

# Hydrodynamics of shock propagation in homogeneous and inhomogeneous gases

*By*

**Amit Kumar**

**PHYS10201705003**

The Institute of Mathematical Sciences, Chennai

*A thesis submitted to the*

*Board of Studies in Physical Sciences*

*In partial fulfillment of requirements*

*for the Degree of*

**DOCTOR OF PHILOSOPHY**

*of*

**HOMI BHABHA NATIONAL INSTITUTE**



July 31, 2025



# Hydrodynamics of shock propagation in homogeneous and inhomogeneous gases

*By*

**Amit Kumar**

**PHYS10201705003**

The Institute of Mathematical Sciences, Chennai

*A thesis submitted to the*

*Board of Studies in Physical Sciences*

*In partial fulfillment of requirements*

*for the Degree of*

**DOCTOR OF PHILOSOPHY**

*of*

**HOMI BHABHA NATIONAL INSTITUTE**



July 31, 2025





# Homi Bhabha National Institute

## Recommendations of the Viva Voce Committee

As members of the Viva Voce Committee, we certify that we have read the dissertation prepared by **Amit Kumar** entitled “**Hydrodynamics of shock propagation in homogeneous and inhomogeneous gases**” and recommend that it may be accepted as fulfilling the thesis requirement for the award of Degree of Doctor of Philosophy.

---

Chairman - **Sibasish Ghosh**

Date: **July 31, 2025**

*Sibasish Ghosh*

---

Guide/Convenor - **R. Rajesh**

Date: **July 31, 2025**

*R. Rajesh*

---

Examiner - **Abhishek Dhar**

Date: **July 31, 2025**

*Abhishek Dhar*

---

Member 1 - **Pinaki Chaudhuri**

Date: **July 31, 2025**

*Pinaki Chaudhuri*

---

Member 2 - **Satyavani Vemparala**

Date: **July 31, 2025**

*Satyavani Vemparala*

---

Member 3 - **Sanatan Digal**

Date: **July 31, 2025**

*Sanatan Digal*

---

Member 4 - **Dibyendu Das**

Date: **July 31, 2025**

*Dibyendu Das*

---

Final approval and acceptance of this thesis is contingent upon the candidate's submission of the final copies of the thesis to HBNI.

I hereby certify that I have read this thesis prepared under my direction and recommend that it may be accepted as fulfilling the thesis requirement.

Date: **July 31, 2025**

Place: IMSc, Chennai

*R. Rajesh*

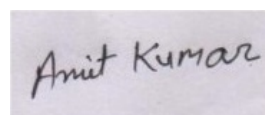
Guide : **R. Rajesh**



## STATEMENT BY AUTHOR

This dissertation has been submitted in partial fulfillment of requirements for an advanced degree at Homi Bhabha National Institute (HBNI) and is deposited in the Library to be made available to borrowers under rules of the HBNI.

Brief quotations from this dissertation are allowable without special permission, provided that accurate acknowledgement of source is made. Requests for permission for extended quotation from or reproduction of this manuscript in whole or in part may be granted by the Competent Authority of HBNI when in his or her judgement the proposed use of the material is in the interests of scholarship. In all other instances, however, permission must be obtained from the author.

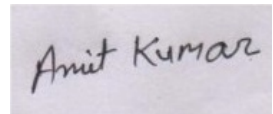
A photograph of a handwritten signature in black ink on a light-colored background. The signature reads "Amit Kumar".

**Amit Kumar**



## DECLARATION

I hereby declare that the investigation presented in the thesis has been carried out by me. The work is original and has not been submitted earlier as a whole or in part for a degree / diploma at this or any other Institution / University.

A photograph of a handwritten signature in black ink on a light-colored background. The signature reads "Amit Kumar" in a cursive script.

**Amit Kumar**



# LIST OF PUBLICATIONS ARISING FROM THE THESIS

## Publications:

- Published

1. Blast Waves in Two and Three Dimensions: Euler Versus Navier–Stokes Equations

Amit Kumar and R. Rajesh, Journal of Statistical Physics **188**(2):1–14, 2022.

2. Shock propagation following an intense explosion in an inhomogeneous gas: core scaling and hydrodynamics

Amit Kumar and R. Rajesh, Journal of Statistical Physics **192**(2):17, 2025.

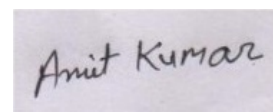
- Submitted

1. Shock propagation in a driven hard sphere gas: molecular dynamics simulations and hydrodynamics

Amit Kumar and R. Rajesh, **DOI** : arXiv:2409.12086

2. Splash in an inhomogeneous gas in one dimension: Exact analysis and molecular dynamics simulations

Amit Kumar and R. Rajesh, **DOI** : arXiv:2504.03549



**Amit Kumar**

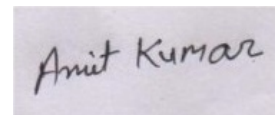




## List of presentations and participations at conferences

1. Presented poster on *Blast Waves in Two and Three Dimensions: Euler Versus Navier–Stokes Equations* at [StatPhys-Kolkata XI \(online\)](#), IISER Kolkata, India (2021)
2. [Statistical Physics of Complex Systems](#) at ICTS, Bengaluru, India (2022)
3. Presented poster on *Driven Shock : Insights from Hydrodynamics and Molecular Dynamics* at [Frontiers in Non-equilibrium Physics](#), IMSc Chennai, India (2023)
4. Gave a talk on *Driven Shock in Three Dimensions: Euler Equation Versus Molecular Dynamics, and Navier-Stokes Equation* at [StatPhys-Kolkata XII](#), SNBNCBS Kolkata, India (2023)
5. Presented poster on *Driven Shock in Three Dimensions: Euler Equation Versus Molecular Dynamics, and Navier-Stokes Equation* at [Chennai Soft Matter Days](#), IMSc Chennai, India (2024)
6. Presented poster on *Driven Shock in Three Dimensions: Euler Equation Versus Molecular Dynamics, and Navier-Stokes Equation* at [APS March Meeting \(Virtual\)](#), 2024
7. Presented poster on *Driven Shock in Three Dimensions: Euler Equation Versus Molecular Dynamics, and Navier-Stokes Equation* at [Fracmeet](#), IMSc Chennai, India (2024)
8. Gave a talk on *Driven Shock in Three Dimensions: Euler Equation Versus Molecular Dynamics, and Navier-Stokes Equation* at [BIFD 2024](#), University of Edinburgh, UK (2024)

9. Presented poster on *Driven Shock in Three Dimensions: Euler Equation Versus Molecular Dynamics, and Navier-Stokes Equation* at **Dynamics Day Europe 2024**, Constructor University, Bremen, Germany (2024)

A photograph of a handwritten signature in black ink on a light-colored surface. The signature reads "Amit Kumar" in a cursive, slightly slanted script.

**Amit Kumar**

Dedicated,  
*To My Family*





## ACKNOWLEDGEMENTS

This thesis is the result of a transformative journey, reflecting my academic growth and many memorable experiences. It would not have been possible without the support of numerous individuals. I am grateful for the opportunity to conduct my doctoral research in the outstanding environment at Matscience and wish to express my sincere appreciation to everyone who contributed to this achievement.

First and foremost, I extend my deepest gratitude to my supervisor, **Prof. R. Rajesh**, for his unwavering support, expert guidance, and invaluable feedback. Your insightful comments, patience, and encouragement were instrumental in shaping my work and personal development. I am deeply grateful for your support, which extended beyond academic matters and contributed to my personal growth.

I would also like to express my gratitude to the members of my doctoral committee: Prof. Dibyendu Das, Prof. Pinaki Chaudhuri, Prof. Sanatan Digal, and Prof. Satyavani Vemparala, for their constructive suggestions, critical questions, and their time in reviewing my work.

Also, I thank Prof. Satyavani Vemparala for her moral support, and help and guidance in the introductory works on charged or uncharged ring and linear polymers, and Prof. Abhishek Dhar for the insightful conversations on the shock waves during FNEP and StatPhys Kolkata conferences. I am also grateful to the professors who taught my master's courses, shared their knowledge, and provided critical evaluations.

I am thankful to Dr. Jilmy P. Joy and Dr. Vinay Vaibhav for helping me learn computational tools and techniques throughout this journey. I appreciate your willingness to assist and clarify even my smallest doubts. I also thank Dr. V. V. Prasad, Dr. Dipanjan Mondal, and Dr. Arghya Das for their valuable feedback during academic discussions. I am grateful to my friends and colleagues Amir, Apurba Biswas,

Goutham, Hitesh, and Subashri for their discussions, which helped me broaden my understanding of various topics. The engaging conversations made this experience more enjoyable.

I am thankful to Matscience for providing the extensive computational resources, facilities, and a supportive research environment. The chance to work here has been a privilege. I thank Vassan for his assistance in resolving computational issues and availing the essential software, making this process smoother. I extend my gratitude to the administrative staff, including Vishnu Prasad, R. Indra, Prema, Usha, K. P. Shankaran, and others, for their help and support during academic and non-academic events and trips. Special thanks to R. Sadhana for being a wonderful friend, a great badminton partner and for her guidance in administrative matters and needs.

I am also deeply grateful to my friends at Matscience, whose presence made this journey more enjoyable and memorable: Pavitra, Gopal, Pavan, Mahaveer, Akhil, Saroj, Raghvendra, Shivam, Amir, Sahil, Pritam, Dheeraj, Ramit, Anupam, Prabhat, Apurba, Jyotijwal, Prateek, Sushovan, Tanmay, Manas, Hitesh, Vaibhav Pathak, Prem, Ravi, Samim, Jatin, Amit Suthar, Vishwajeet, Arup, Harshit, Sashikanta, Saurav, Roni, Sayak, Jitin, Aparna, Vidya, Piyasa, Farhina, Surabhi, Chandrani, Subashri, and many others whom I might have missed mentioning here. You people made this journey more joyful and memorable.

I also want to thank the sports facilities at Matscience, especially the badminton court, where I enjoyed playing with friends like Anupam, Mrigendra, Balesh, Sreeraj, Vasan, Pritam, Abinash, Abhishek, Dheeraj, Ramit, Apurba, Jyotijwal, Sushovan, Manas, Prem, Ravi, Amit Suthar, Vishwajeet, Harshit, Sashikanta, Roni, Sayak, Jitin, Sadhana, Piyasa, Pavitra, Vanisha, and Nandini. The fun moments and friendly atmosphere at the court were truly memorable. I am grateful for my badminton partners: Sadhana, Aparna, Renju, Gayathri, Amir, Chandrashekhar, Mani,

Jyotijwal, and Jitin, who made the badminton tournaments at Matscience special. I am deeply grateful to my family for their unwavering support. I owe everything to you!! To my parents, thank you for your unconditional love, sacrifices, and belief in me. Your simple line, “Beta, abhi ham hain na!!”, gave me immense strength to face any challenges in life. To my sisters, thank you for your sacrifices, love, and for taking care of the home in the absence of us two brothers. To my brother, thank you Bhaiya, for always being there for me, and looking after me on each and every challenge in my life. Your love, care, and encouragement have been a constant anchor throughout my academic journey. To my sister-in-law, thank you Bhabhi, for always cheering me on and taking care of the home in the absence of us siblings. Finally, I would like to express my gratitude to everyone who, directly or indirectly, contributed to this thesis through their ideas, feedback, or moral support. This work would not have been possible without you all.





# Table of Contents

List of Figures	vii
List of Tables	xiii
Synopsis	xv

1

Chapter 1

Introduction

1.1 Shock waves and TvNS theory : A historical note . . . . .	2
1.2 Shock Propagation in Different Cases . . . . .	5
1.2.1 Shock propagation in an in-homogeneous medium . . . . .	6
1.2.2 Shock propagation due to splash . . . . .	7
1.2.3 Shock Propagation in Driven Systems . . . . .	7
1.3 Corrections in TvNS theory : The Role of Dissipation Terms . . . . .	8
1.4 Overview of the Thesis . . . . .	9
1.5 Organisation of Chapters . . . . .	11

---

**15** | **Chapter 2**  
**Hydrodynamics**

2.1	Gas dynamics . . . . .	16
2.1.1	Continuity Equations . . . . .	17
2.2	Navier-Stokes equations . . . . .	19
2.3	Euler equation . . . . .	20
2.4	Surface of shock and boundary condition . . . . .	20

**23** | **Chapter 3**  
**Computational Methods**

3.1	Event-Driven Molecular Dynamics . . . . .	23
3.2	Numerical methods to solve ordinary differential equations : . . . . .	27
3.3	Numerical methods to solve partial differential equations : . . . . .	29

**33** | **Chapter 4**  
**Blast Waves in Two and Three Dimensions: Euler Ver-**  
**sus Navier–Stokes Equations**

4.1	Introduction . . . . .	33
4.2	Hydrodynamics and Numerical details . . . . .	35
4.2.1	Hydrodynamics . . . . .	35
4.2.2	Numerical method . . . . .	37
4.2.3	Solution of Navier-Stokes equations in cartesian coordinates . . . . .	38

---

4.3	Results . . . . .	40
4.3.1	Results in two dimensions . . . . .	41
4.3.2	Results in three dimensions . . . . .	44
4.4	Summary and discussion . . . . .	46

## 51 **Chapter 5** **Shock propagation following an intense explosion in an inhomogeneous gas: core scaling and hydrodynamics**

5.1	Introduction . . . . .	51
5.2	Problem definition . . . . .	53
5.3	Exact solution of the Euler equation in $d$ -dimensions . . . . .	54
5.3.1	Euler equation . . . . .	54
5.3.2	The exact solution . . . . .	57
5.3.3	Asymptotic behaviour for $\xi \rightarrow 0$ . . . . .	58
5.3.4	Critical $\beta$ . . . . .	60
5.4	Molecular Dynamics Simulations . . . . .	60
5.4.1	Model . . . . .	61
5.4.2	Behaviour of thermodynamic quantities . . . . .	62
5.4.3	Comparison between the exact solution of the Euler equation and simulations . . . . .	65
5.5	Navier-Stokes Equations . . . . .	65
5.5.1	Numerical details . . . . .	65

---

5.5.2	Comparison between Euler equation, Simulation, and Navier-Stokes equations . . . . .	67
5.6	Scaling near the shock center in one dimension . . . . .	71
5.7	Behaviour for critical $\beta_c$ . . . . .	74
5.8	Summary and Discussion . . . . .	74

## 79 Chapter 6

### Splash in an inhomogeneous gas in one dimension: Exact analysis and molecular dynamics simulations

6.1	Introduction . . . . .	79
6.2	Model and continuity equations . . . . .	81
6.3	Exact solution of the exponent $\alpha$ . . . . .	84
6.4	Event driven molecular dynamics simulations . . . . .	86
6.5	Results . . . . .	89
6.5.1	The exponents $\delta_s$ and $\alpha$ . . . . .	89
6.5.2	Behaviour of Thermodynamic Quantities . . . . .	90
6.6	Summary and Discussion . . . . .	91

## 95 Chapter 7

### Shock propagation in a driven hard sphere gas : molecular dynamics simulations and hydrodynamics

7.1	Introduction . . . . .	95
7.2	Review of Euler Equation for Driven Shock . . . . .	98

---

7.2.1	Continuity equation of energy for uniform driving . . . . .	100
7.2.2	Continuity equation of entropy for central driving . . . . .	101
7.2.3	Non-dimensional continuity equations for ideal gas . . . . .	102
7.2.4	Euler equation for hard sphere gas . . . . .	110
7.3	EDMD Simulations . . . . .	113
7.4	Navier-Stokes equations . . . . .	117
7.5	Results : comparison between the Euler equation, EDMD, and DNS .	126
7.6	Summary and discussion . . . . .	128

## 131 | Chapter 8

### Summary and outlook

8.1	Conclusions and Outlook . . . . .	132
-----	-----------------------------------	-----

<b>Bibliography</b>	<b>135</b>
---------------------	------------



# List of Figures

3.1	<i>Computational methods : schematic of the numerical algorithm used to solve the system of ordinary differential equations with specified boundary conditions. . . . .</i>	29
3.2	<i>Computational methods : comparison of exact and numerical solutions of the Euler equation for different values of a control parameter using Rankine-Hugoniot boundary conditions. . . . .</i>	30
3.3	<i>Computational methods : schematic illustration of the MacCormack method for solving a PDE using predictor-corrector steps. . . . .</i>	31
3.4	<i>Computational methods : comparison of numerical and exact solutions of the heat equation at different times using the MacCormack method. . . . .</i>	32
4.1	<i>Blast in homogeneous medium : two-dimensional spatial variation of density, temperature, and velocity at single time, along with the radial distance variation at three different times, demonstrating the boundary conditions at shock center. . . . .</i>	39
4.2	<i>Blast in homogeneous medium : comparison of EDMD data and DNS results for non-dimensionalised density, radial velocity, temperature, and pressure, for different times, and the TvNS solution with virial EOS. . . . .</i>	42
4.3	<i>Blast in homogeneous medium : variation of density, velocity, temperature, and pressure obtained from DNS of NSE in two dimensions, with different truncations of the virial expansion at a single time. . .</i>	43

4.4	<i>Blast in homogeneous medium : variation of non-dimensionalised density, radial velocity, temperature, and pressure for different values of coefficient of heat conduction keeping coefficient of viscosity fixed. . . . .</i>	44
4.5	<i>Blast in homogeneous medium : variation of non-dimensionalised density, radial velocity, temperature, and pressure for different values of coefficient of viscosity keeping coefficient of heat conduction fixed. . . . .</i>	45
4.6	<i>Blast in homogeneous medium : comparison of EDMD and DNS results in three dimensions showing non-dimensionalised profiles of density, radial velocity, temperature, and pressure at four different times. . . . .</i>	47
4.7	<i>Blast in homogeneous medium : radial variation of non-dimensionalised density, velocity, temperature, and pressure from DNS of NSE for two different equations of state at a fixed time. . . . .</i>	49
5.1	<i>Blast in inhomogeneous medium : density, velocity, and temperature profiles from exact Euler solutions for various inhomogeneity values in one dimension. . . . .</i>	59
5.2	<i>Blast in inhomogeneous medium : power law growth of shock front radius over time for different inhomogeneity parameters. . . . .</i>	63
5.3	<i>Blast in inhomogeneous medium : spatial variation of density, velocity, and temperature at different times for two inhomogeneity values, above and below the critical value of inhomogeneity. . . . .</i>	64
5.4	<i>Blast in inhomogeneous medium : comparison of EDMD simulation results for thermodynamic quantities with exact solution of Euler equation for different inhomogeneity values. . . . .</i>	66
5.5	<i>Blast in inhomogeneous medium : effect of heat conduction and bulk viscosity on density, velocity, and temperature profiles from DNS of NSE for a fixed value of inhomogeneity. . . . .</i>	69

---



5.6	<i>Blast in inhomogeneous medium : comparison of EDMD, Euler, and DNS results for density, velocity, and temperature profiles at two inhomogeneity values—one below and one above the critical value. . . .</i>	70
5.7	<i>Blast in inhomogeneous medium : scalings of thermodynamic quantities obtained from EDMD results for front and core scaling at different times for a single value of inhomogeneity. . . . .</i>	73
5.8	<i>Blast in inhomogeneous medium : comparison of the exact solution of Euler equation and DNS results of NSE with EDMD data for density, velocity, and temperature at different times for a critical value of inhomogeneity. . . . .</i>	75
5.9	<i>Blast in inhomogeneous medium : variation of the shock front radius with time for two different initial density profiles, showing similar power-law growth at late times as for a uniform density profile. . . .</i>	77
6.1	<i>1D-Splash : variation of point of singularity, density, velocity, and temperature with inhomogeneity parameter at the singular point from Euler equation analysis. . . . .</i>	87
6.2	<i>1D-Splash : power-law behaviours of energy and shock front radius with time from EDMD simulations for different inhomogeneity parameter. . . . .</i>	89
6.3	<i>1D-Splash : comparison of the power-law exponents of the energy and the shock radius from Euler analysis and EDMD simulations. . . . .</i>	90
6.4	<i>1D-Splash : spatial variation of density, velocity, and temperature for fixed inhomogeneity parameter at different times, and for fixed time at different inhomogeneity parameter. . . . .</i>	92
6.5	<i>1D-Splash : variation of scaling functions with rescaled distance for different inhomogeneity parameter, EDMD data compared with self-similar solutions of Euler equation. . . . .</i>	93

---

7.1	<i>Driven shock : comparison of exact and asymptotic power law solutions of Euler equation for density, velocity, temperature, and pressure under uniform driving in two dimensions for different values of driving exponents. . . . .</i>	108
7.2	<i>Driven shock : the behavior of Euler equation under central driving for different values of driving exponents. . . . .</i>	109
7.3	<i>Driven shock : non-dimensionalised thermodynamic profiles from numerical solution of Euler equation with a truncated virial equation of state under uniform driving, showing negligible truncation error after <math>10^{th}</math> term. . . . .</i>	112
7.4	<i>Driven shock : power-law behaviour of scaling functions from numerical solution of Euler equation for hard sphere gas under uniform driving in two dimensions, showing independence from driving exponent.</i>	113
7.5	<i>Driven shock : snapshots of a shock cross-section in the <math>x</math>-<math>y</math> plane showing particle positions within a narrow <math>z</math>-slice, with stationary and moving particles distinguished by colour under central driving. . .</i>	116
7.6	<i>Driven shock : power-law growth of energy, shock front radius, and total radial momentum under central driving in two dimensions, with EDMD simulation results compared to theoretical scaling laws. . . . .</i>	118
7.7	<i>Driven shock : power-law growth of energy, shock front radius, and total radial momentum under central driving in two dimensions, with DNS results of NSE compared to theoretical scaling laws. . . . .</i>	122
7.8	<i>Driven shock : effect of the truncation of virial EOS on DNS data of NSE for density, velocity, temperature, and pressure, comparing central and uniform driving in two dimensions with virial EOS truncated at different terms. . . . .</i>	123

---

7.9	<i>Driven shock : non-dimensionalised profiles of density, velocity, temperature, and pressure from DNS of NSE for varying viscosity coefficients under central driving in two dimensions, with fixed heat conduction and a truncated virial EOS. . . . .</i>	124
7.10	<i>Driven shock : non-dimensionalised profiles of density, velocity, temperature, and pressure from DNS of NSE for varying heat conduction coefficients under central driving in two dimensions, with fixed viscosity and a truncated virial EOS. . . . .</i>	125
7.11	<i>Driven shock : comparison of non-dimensionalised density, velocity, temperature, and pressure profiles obtained from Euler equation, EDMD, and DNS of NSE in two dimensions for central and uniform driving, showing results at different times and parameters for each method. . . . .</i>	127
7.12	<i>Driven shock : comparison of non-dimensionalised density, velocity, temperature, and pressure profiles from EDMD and DNS of NSE in three dimensions, showing results at single and multiple time points for each method under the same initial conditions. . . . .</i>	129



# List of Tables

4.1	<i>Blast in homogeneous medium : numerical values of the virial coefficients for hard sphere gas in two and three dimensions. . . . .</i>	37
4.2	<i>Blast in homogeneous medium : numerical values of parameters used in solving the NSE in two and three dimensions, with all quantities measured in terms of chosen length, mass, and time scales. . . . .</i>	38
5.1	<i>Blast in inhomogeneous medium : values of the inhomogeneity parameter where the analytical solution becomes singular in different dimensions. . . . .</i>	58
5.2	<i>Blast in inhomogeneous medium : parameters used in the numerical solution of the NSE. . . . .</i>	68
6.1	<i>1D-Splash : different values of the energy decay exponents in an inhomogeneous medium corresponding to various inhomogeneity parameter, obtained from second-kind self-similar solutions of the Euler equation. . . . .</i>	86
7.1	<i>Driven shock : numerical values of the rescaled positions of the shock fronts in Euler equation for the hard sphere gas at different virial terms under uniform driving in three dimensions. . . . .</i>	111
7.2	<i>Driven shock : numerical values of the parameters used in solving the Navier-Stokes equations. . . . .</i>	121



# Synopsis

A thermodynamic system, depending on the absence or presence of currents can exist in thermal equilibrium or out of equilibrium. When a system in equilibrium is perturbed slightly, the relaxation back to equilibrium can be understood in terms of linear response theory. However, large perturbations drive the system far from equilibrium, making it difficult to analyze its relaxation behavior. A simple example of such an intense perturbation is the sudden input of a large amount of energy in a localized region in space. Examples of such perturbations include atomic blasts, supernova explosions, gamma-ray bursts, plasma breakdown due to laser pulses, or granular fingering. In such cases, the flow velocity of the system exceeds the velocity of sound in the system resulting in a shock. On the other hand, continuous localized driving maintain the system out of equilibrium while also creating a shock wave. In this thesis, we investigate shock propagation caused both an instantaneous input of energy followed by relaxation as well as a continuous time dependent input of energy, in both homogeneous and inhomogeneous media.

The instantaneous release of a large amount of energy in a localized space in an ambient gas causes a spherically symmetric disturbance. This disturbance expands radially outward, creating a shock front that separates the disturbed medium from the ambient medium. Across this shock front, the different thermodynamic quantities are discontinuous, while, they are continuous within the shock. The magnitudes of these discontinuities are determined by the continuity of currents across the shock

front, also known as the Rankine-Hugoniot boundary conditions [1–3]. The study of shock waves, particularly those originating from a point explosion, is a classic problem in gas dynamics [1–3]. Key questions that have been studied include: How does the radius of the shock front evolve with time? What is the spatio-temporal behavior of various thermodynamic quantities? What is the correct hydrodynamic description of the problem?

For a shock wave following a blast in a homogeneous medium, using dimensional analysis, the time evolution of the shock front radius,  $R(t)$ , is found to follow a power law:  $R(t) \sim (E_0 t^2 / \rho_0)^{1/(2+d)}$  in  $d$ -dimensions, where  $E_0$  is the energy of the explosion, and  $\rho_0$  is the mass density of the ambient system [4–7]. This power-law behavior has been verified in the Trinity explosion [4], and high-energy laser pulses in gas jets [8], in plasma media [9], and in clusters of different gases [10]. The response of the gas to the blast can be described in terms of local density,  $\rho(r, t)$ , velocity,  $u(r, t)$ , temperature,  $T(r, t)$ , and pressure,  $p(r, t)$ , at radial distance  $r$  and time  $t$ . The long time behavior of these thermodynamic quantities are described by the continuity equations of the conserved quantities: mass, momentum, and energy. In addition, assuming local thermal equilibrium implies a relationship between local pressure, temperature, and density through an equation of state. In the scaling regime,  $r, t \rightarrow \infty$  keeping  $rt^{-2/(2+d)}$  fixed, dissipation due to heat conduction and viscosity become negligible, reducing the continuity equations to the Euler equation. The exact solution to the Euler equation in three dimensions for an ideal gas, consistent with the Rankine-Hugoniot boundary conditions, was obtained by Taylor, von-Neumann, and Sedov [4–7], which we will refer as the TvNS solution.

There are other problems closely related to the shock propagation in a homogeneous medium described above. First is the shock propagation due to a blast in an inhomogeneous medium where the initial density varies as  $\rho(r) = \rho_0 r^{-\beta}$ . The TvNS solution corresponding to  $\beta = 0$ , can be extended to the case  $0 \leq \beta < d$  [11].



Second is the blast problem in a system composed of a gas in the region  $x \geq 0$  and vacuum in the region  $x < 0$ . At long times, the entire energy is reflected back into the vacuum, and the energy of the gas decreases as a power law  $E(t) \sim t^{-\delta_s}$ . This problem is referred to the splash problem. The exponent  $\delta_s$  was determined recently in one dimension for a homogeneous medium [12]. A third related problem is the study of shock waves due to the continuous input of energy into the medium in a localized region, where the total energy increases as  $E(t) = E_0 t^\delta$ . In this case the system is driven away from the equilibrium. For an ideal gas, the TvNS solution can be generalized to the driven case and the exact solution for the thermodynamic quantities can be found [13]. We will refer to this problem as the driven shock.

Only recently has the shock problem has been studied using hard sphere simulations. While the radius of shock front aligns with TvNS theory in two and three dimensions [14, 15], there were significant discrepancies in density, velocity, temperature, and pressure profiles near the shock center between simulations and TvNS theory in all the dimensions [16–18]. The cause of these mismatches was hypothesized to be the omission of heat conduction. At the shock center, TvNS predicts a diverging temperature. However, the presence of a conduction term implies that the derivative of temperature being zero. The scaling limits are not commutative: scaling thermodynamic quantities followed by solving continuity equations, as done in TvNS theory, differs from solving continuity equations first and then scaling thermodynamic quantities. The correct approach involves solving the continuity equations with dissipation terms, specifically the Navier-Stokes equation. This was demonstrated for point-sized particles in one dimension where the simulations were shown to be described by Navier-Stokes equation [18]. A length scale was identified below which heat conduction is relevant and above which it can be ignored. The exponents describing this crossover were determined.

In this thesis, we follow this line of investigation to understand the hydrodynamics of

---

the shock propagation. Analysis up to now was mostly on the blast in a homogeneous medium. For this problem also, it is not clear whether the Navier-Stokes equation will capture the molecular dynamics simulations in two and higher dimensions where excluded volume effects become important. When the system is inhomogeneous with an initial density  $\rho(r) = \rho_0 r^{-\beta}$ , the role of inhomogeneity is not clear. Likewise the role of inhomogeneity in determining the exponents for splash problem remain unexplored. Finally, for the driven shock, it is not clear at all whether Navier-Stokes equation is the correct description. To address these open issues, we address the following question in this thesis.

## Questions:

1. For shocks following a blast in a homogeneous medium in two and three dimensions, is Navier-Stokes equation the correct hydrodynamics description?
2. For a blast in an inhomogeneous medium with  $\rho(r) = \rho_0 r^{-\beta}$ ,  $0 < \beta < d$ , does the Navier-Stokes describe the numerical data? Is there a critical  $\beta$  for which the Euler equation is the correct description? What are the crossover exponents describing the crossover from core scaling near the shock center to the scaling near the shock front?
3. For splash in an inhomogeneous medium with  $\rho(r) = \rho_0 r^{-\beta}$ ,  $0 < \beta < 1$ , in one dimension, can the exponent characterizing energy decay in the medium be calculated exactly? Is the Euler equation sufficient to describe the problem?
4. For driven shocks that are far from equilibrium, does the Euler equation describe the behavior away from shock front? Does the Navier-Stokes equation describe the behavior near shock center? What is the role of hard core exclusion?

We address these questions by studying shock propagation using three methods: event driven molecular dynamics simulations, scaling solution of the Euler equation, and the numerical integration of the Navier-Stokes equation .

The event driven simulations are done for a mono-disperse hard sphere system in two and three dimensions and bi-disperse point particles in one dimension. All collisions are energy and momentum conserving. Initially all particles are at rest. For the splash problem only the region  $x \geq 0$  is occupied. For other problems, the number density is spherically symmetric  $\rho(r) = \rho_0 r^{-\beta}$ ,  $0 \leq \beta < d$ . For the blast problem, energy is given to a few particles around the origin. For the driven shock, particles within a fixed radius are driven stochastically throughout the simulations.

For the Euler equation, we non-dimensionalize the thermodynamic quantities, and either solve exactly or solve numerically, depending on the equation of state, the resultant ordinary differential equations consistent with Rankine-Hugoniot boundary conditions.

The Navier-Stokes equation cannot be solved analytically. We use MacCormack method to numerically integrate the Navier-Stokes equation. This method is accurate up to second order both in time and space discretization. The initial condition for the simulations is chosen appropriately depending on the system being studied.

## Findings of the thesis

We enumerate the results found in these studies:

### 1. Blast in two and three dimensions in a homogeneous medium

- To model the hard sphere gas, we use both the virial equation of state as well as the Henderson equation of state in the Navier-Stokes equation.

- We resolve the earlier observed mismatch between the theoretical predictions, based on the Euler equations, for the time evolution of a blast wave and results from hard sphere simulations in two and three dimensions.
- We compare the results of direct numerical simulations of the Navier-Stokes equation in two and three dimensions with the molecular dynamics data, and show they match quantitatively.
- We conclude that the order in which the scaling limit is taken is important in the blast problem. In the TvNS solution, the scaling limit is taken first – heat conduction and viscosity terms being irrelevant – before the exact solution is found. However, the correct limit to take is to find the solution with non-zero heat conduction and viscosity terms and then take the scaling limit.
- The direct numerical solution data shows no dependence on the viscosity constant when constant of heat conduction was held fixed; however, changes in direct numerical solution data were observed when varying the heat conduction constant with fixed viscosity. Notably, the power-law exponents of thermodynamic quantities remained unaffected by these variations.

## 2. Blast in an inhomogeneous medium

- We generalize the exact solution of the Euler equation for a blast, consistent with the Rankine-Hugoniot boundary conditions, to arbitrary  $d$ -dimensions.
  - From the asymptotic behavior of the solution near the shock center, we argue that only for  $\beta_c = d^2/(d+2)$ , should the Euler equation provide a full description of the blast response.
  - Using event driven molecular dynamics simulations in one dimension, we show that the Euler equation does not describe the data near the shock
-

center. On the other hand the Navier-Stokes equation is able to overcome this issue.

- The crossover length scale below which the dissipation terms are relevant are derived for arbitrary  $\beta$ . The core scaling for the data near the shock center are also derived for arbitrary  $\beta$  and confirmed in event driven molecular dynamics simulations in one dimension.
- In one dimension, the direct numerical solution data showed quantitative dependency on both heat conduction when bulk viscosity held fixed as well as bulk viscosity when heat conduction held fixed.

### 3. Splash in an inhomogeneous medium in one dimension

- In this case, the similarity exponent  $\alpha$  in the growth of the radius of the shock front,  $R(t) \sim t^\alpha$ , cannot be derived from dimensional analysis, as with other problems addressed in this thesis. We determined different values of  $\alpha$  in one dimension by locating the singular points of different thermodynamic quantities in the Euler equation. For the solution curve to yield a single-valued solution for the thermodynamic quantities, it must pass through these singular points, consistent with the Rankine-Hugoniot boundary conditions.
- The energy in the medium decays as  $t^{-\delta_s}$ , where  $\delta_s$  is shown to be  $\delta_s = 2 - \alpha(3 - \beta)$  in one dimension.
- The numerically exact values of  $\alpha$  for different  $\beta$ , found using the Euler equation, are validated by event driven molecular dynamics simulations in one dimension..
- The event driven molecular dynamics simulations data for the different thermodynamic quantities are shown to be well described by the Euler equation for all  $\beta$ .

#### 4. Driven shock in a homogeneous medium

- We studied the hydrodynamics of shocks in a gas in which energy is continuously input at one localized region in space. Different schemes were used to study this problem: event driven molecular dynamics simulations, direct numerical solution of Navier-Stokes equation, and numerical solution of the Euler equation.
- We show that the solution of Euler equation does not match with the event driven molecular dynamics data anywhere, but the numerical solution of Navier-Stokes equation shows a reasonable agreement with the event driven molecular dynamics results, provided the heat conduction and viscosity are chosen parametrically.
- We show that the different scaling functions within the Euler equation, follow power law behavior close to the shock center with respective exponents are independent of the driving exponent  $\delta$ .
- We conclude that even though the continuous drive takes the system far from equilibrium, Navier-Stokes equation continues to give a good description of the system.
- We also show that the direct numerical solution data changes with heat conduction when viscosity was fixed, while it does not change when viscosity varied keeping heat conduction fixed.

# 1

## Introduction

Thermodynamically, systems can exist in equilibrium, non-equilibrium, or far-from-equilibrium states. In equilibrium systems, properties like energy, temperature, and pressure remain constant, with no net flow of energy or matter. Equilibrium thermodynamics has been key to industrial advancements such as gasoline engines, refrigeration systems, and the Haber-Bosch process for ammonia production.

However, most systems in nature and industry operate far from equilibrium. Non-equilibrium processes govern complex systems like catalytic reactors in chemical industries, cellular metabolism in biology, and large-scale weather patterns. Astrophysical phenomena like supernovae, star formation, and galaxy dynamics are also driven by non-equilibrium conditions. These systems often exhibit behaviours such as turbulence, clustering, and shock wave propagation, as seen in earthquakes, volcanic eruptions, and cosmic events.

While small perturbations in equilibrium systems can be modelled using methods like linear response theory, large perturbations push systems far from equilibrium,

making traditional analysis challenging. Examples include high-speed jets and bullets, which generate strong shock waves as they exceed the speed of sound. In astrophysics, extreme events like supernova explosions or gamma-ray bursts create powerful shock waves that propagate through interstellar space, affecting the formation of stars and galaxies.

A special class of large-scale disturbances arises from point perturbations, such as atomic explosions or supernovae. These events inject massive amounts of energy into the surrounding medium, resulting in shock waves that travel at supersonic speeds. This thesis focuses on studying shock wave propagation in homogeneous and inhomogeneous media, caused by single impacts or continuous energy sources. Understanding shock waves is crucial for both practical applications—such as aerospace, energy systems, and medicine—and for interpreting astrophysical phenomena like stellar explosions and galaxy evolution.

## **1.1 Shock waves and TvNS theory : A historical note**

High-speed objects like aircraft, missiles, supersonic jets, and modern fighter planes compress the air in front of them, generating shock waves due to the sudden disturbances they create. Similar effects are seen in astrophysics, where meteoroids and spacecraft generate shock waves as they travel through planetary atmospheres. Shock waves also occur in interstellar space as stars, planets, or even galaxies move through gaseous environments, creating compression waves.

The study of shock propagation resulting from intense explosions is a classic problem in gas dynamics, with a wide range of applications, from astrophysical blast waves like supernova explosions to controlled fusion in plasma physics [1–3, 11]. The immediate release of a large amount of energy in a localised space within a stationary



system creates a spherically symmetric disturbance that expands radially over time, with a front that separates the affected material from the ambient medium, known as the shock front. In the affected region, various thermodynamic quantities, such as density, velocity, temperature, and pressure, vary continuously with radial distance  $r$  at any time  $t$ , while they change abruptly across the shock front. The extent of these changes in thermodynamic quantities is described by the Rankine-Hugoniot boundary conditions [1–3].

Initially, the system loses energy solely through radiation for a brief moment. As the system cools, it enters the hydrodynamic regime where the primary mode of energy transport is through particle motion. In this regime, shock propagation is described by continuity equations for three globally conserved quantities: mass, momentum, and energy. These continuity equations are non-linear partial differential equations that involve local fields of density, velocity, temperature, and pressure. The assumption of local thermal equilibrium relates local pressure to local density and temperature through the equation of state of the gas, effectively reducing the number of dependent variables by one.

In the 1940s, Geoffrey Taylor, John von Neumann, and Leonid Sedov (TvNS) tackled the complex problem of shock propagation to understand the mechanical effects resulting from the release of substantial energy in atomic explosions. Each of these scientists applied their unique expertise to develop a theoretical framework, scaling laws, and analytical solutions to model shock wave behaviour, focusing on how energy propagates through the medium from the detonation point. Taylor investigated the effects of large explosions potentially caused by high-energy nuclear fission. His analysis of the Trinity test, a controlled blast in the Jornada del Muerto desert in New Mexico in June 1945, successfully predicted the growth of the shock front radius over time using only three control parameters: the energy  $E_0$  of the explosion, the mass density of air  $\rho_0$ , and time  $t$ . He applied dimensional analysis to derive

the growth of the shock front radius as  $R(t) \sim (E_0 t^2 / \rho_0)^{1/5}$ . Simultaneously, Sedov, working independently in the Soviet Union, approached the problem theoretically, similar to Taylor, and derived an expression for the growth of the shock front radius in general  $d$ -dimensions. Remarkably, this power-law behaviour closely matched the radius data extracted from images of the Trinity explosion taken at various times [5].

In recent decades, the power-law growth of the shock front radius has been confirmed in numerous experimental studies, including blast waves resulting from high-energy laser pulses in gas jets in 2D [8], in plasma media in 3D [9], and in clusters of different gases in both 2D and 3D [10].

In the scaling regime where  $r \rightarrow \infty$  and  $t \rightarrow \infty$ , keeping  $rt^{-2/5}$  finite, TvNS made the following assumptions:

- Heat conduction and viscosity terms are negligible compared to other terms.
- The gas is in local thermal equilibrium, and an equation of state linking the thermodynamic variables exists.
- The gas follows the ideal equation of state.

Under the TvNS assumptions, the continuity equations reduce to the Euler equation with the ideal equation of state. TvNS provided an exact solution to the Euler equation that describes the spatio-temporal evolution of thermodynamic quantities caused by a point explosion [4–7]. This solution is self-similar in time and will be referred to as the TvNS solution for the remainder of this thesis.

The TvNS theory has various applications, including modeling supernova explosions and the early evolution stages of young supernova remnants [19–25], and in studying astrophysical blast waves caused by hidden powerful neutrino sources [26]. The TvNS theory has been generalised to examine shocks in granular gases, where energy is no longer conserved [27, 28]. It has also been utilised to describe driven shocks in

---

homogeneous media, where energy is continuously injected into the system, such as in nebula formation and its motion due to stellar winds interacting with interstellar gas [29, 30], as well as bubble formation around stars from strong stellar winds interacting with the interstellar medium [31, 32]. The TvNS theory has been extended to include various effects such as heat conduction [33–36], viscosity [37–40], and thermal radiation [41, 42]. It has also been applied to study implosion problems, where shock waves converge from infinity and then diverge from the center of symmetry after reflecting from the symmetry point [3, 43–46].

Granular materials are prevalent in nature and are significant in industry and daily life [47]. These materials exhibit key properties of inelastic collisions, leading to energy loss over time. Shock propagation has also been studied in granular systems, with examples including crater formation due to the impact of high-energy particles on a granular heap [48], vertical impacts of steel balls into containers of small glass beads [49], vertical impingement of gas jets on granular beds [50], and shock propagation from impacts on fast-flowing granular layers [51] or due to sudden localised energy releases [14, 52]. Additionally, shock wave propagation in vibrofluidised granular materials has been studied [53–56], and stationary shocks have been observed in nonlinear granular chains due to nonlinear pulses from one end [57–60]. Understanding shock propagation in granular materials is crucial for modelling impacts on geological surfaces, such as meteorite impacts on planets or asteroids.

## **1.2 Shock Propagation in Different Cases**

The radius of the shock front depends solely on initial conditions such as total energy, ambient mass density, and time. Therefore, understanding the response of shock propagation to alterations in initial conditions – like initial mass density distribution, energy injection or the surface effects – is crucial.

### 1.2.1 Shock propagation in an in-homogeneous medium

The shock propagation has been studied in various environments with different density distributions and under various effects. For example, strong spherical blast waves in heat-conducting gases and their interactions with electromagnetic fields have been examined [61], as well as strong underwater explosions [62], and shocks in various atmospheric conditions [63, 64]. Additionally, shock propagation in variable density media has been explored, including linear and nonlinear density distributions [62, 65], uniform and non-uniform media [66], exponential density distributions [67], and power-law decaying densities [11, 68, 69].

The study of shock propagation in a medium with a power-law decaying density, expressed as  $\rho = \rho_0 r^{-\beta}$ , is particularly significant in astrophysical blast wave research [24, 64, 70–72]. Expanding the analysis of shock waves from homogeneous to inhomogeneous gases, where the initial density distribution decreases as a power law with radial distance, introduces new challenges and necessitates generalising the TvNS solution. In such systems, the growth of the shock front radius following an explosion with energy  $E_0$  can be expressed as:

$$R(t) \sim \left( \frac{E_0 t^2}{\rho_0} \right)^{\frac{1}{2+d-\beta}},$$

in  $d$ -dimensions, where  $\beta$  is the inhomogeneity parameter [11]. This result stems from dimensional analysis, treating  $E_0$ ,  $\rho_0$ , and  $t$  as fundamental quantities and initial control parameters. The shocks are decelerating if  $\beta < d$ , and accelerating if  $d < \beta < d + 2$ . Thus, the results of shock propagation in these media generalise the shock propagation in homogeneous media when  $\beta = 0$ .

These problems have been formulated and studied by extending the TvNS theory, and presented an exact solution in three dimensions [11, 68].

### 1.2.2 Shock propagation due to splash

An interesting scenario to pinpoint the initial conditions could be the case where there is vacuum in half the space and a gas in the other half. Energy is input at a point in the interface. This problem is referred as the splash problem. This problem is less studied in comparison to the blast problem. In a recent paper, the splash problem was studied in one dimension when the gas is homogeneous [12]. The energy is reflected back into the vacuum, and in the scaling regime the total energy of medium (gas) decays as  $E(t) \sim t^{-\delta_s}$ . The value of  $\delta_s = 0.11614383675\dots$  has been obtained for the homogeneous medium in one dimension by analysing the Euler equation, using self-similarity of the second kind. The value of  $\delta_s$  was obtained by arguing that the singular points in the Euler equation should be canceled by zeros elsewhere. The results were validated using molecular dynamics simulations of hard point particles of different masses with alternate particles having same mass [12].

### 1.2.3 Shock Propagation in Driven Systems

A closely related problem involves shocks generated by a continuous input of energy at a specific point in space. Unlike the single impact scenario, now the system is driven away from equilibrium due to a constant energy current. The driven shock problem is relevant for studying the motion of interstellar gas influenced by continuous energy injection from stellar winds [29, 30]. In this case, a homogeneous system is driven from the center by an external point or extended source that injects energy continuously, resulting in an increase in the total energy of the system as  $E(t) = E_0 t^\delta$ . Dimensional analysis indicates that the radius of the shock front of a driven shock increases over time as:

$$R(t) \sim \left( \frac{E_0 t^{2+\delta}}{\rho_0} \right)^{\frac{1}{d+2}},$$

in  $d$ -dimensions [1, 11, 13, 73].

These kind of shocks have been studied extensively, focusing on either the radius of the shock front or the spatio-temporal behaviour of thermodynamic quantities. Examples include shock propagation resulting from continuous energy injection via particle insertion [74], granular fingering and pattern formation due to the injection of viscous liquids into dry dense granular materials [75–79], and an exact solution of the Euler equation for shock propagation due to continuous energy injection by an external point source, derived by Dokuchaev [13], notably the results with  $\delta = 0$  reproduces the results of single impact.

### 1.3 Corrections in TvNS theory : The Role of Dissipation Terms

Unlike the scaling law for  $R(t)$ , the direct experimental determination of scaling functions for density, temperature, velocity, and pressure is limited to the measurement of the density profile at a single time (see Fig. 1 of [8] and the inset of Fig. 5 of [10]). However, these data are insufficient for making a meaningful comparison with the theoretical predictions for the scaling functions derived from the TvNS theory. In the absence of experimental data, molecular dynamics (MD) simulations of hard spheres can serve as a model platform for verifying the TvNS solution.

Recently, the TvNS theory has been tested against MD simulations of hard spheres in both two and three dimensions. Initial MD studies confirmed the power-law growth of the shock front radius in two dimensions [14, 15] and three dimensions [14], consistent with the TvNS theory. Subsequent work focused on validating the theoretical predictions of the scaling functions for density, radial velocity, temperature, and pressure. One study of scaling functions in two dimensions concluded that the TvNS theory accurately describes the simulation data for low to medium number

densities, except for small discrepancies near the shock front and slight deviations near the shock center [28]. However, more extensive large-scale simulations revealed that the numerically obtained radial distributions of density, radial velocity, and temperature did not align with the TvNS theory (modified to account for steric effects), neither in two dimensions [17] nor in three dimensions [16]. The discrepancies manifested as differing power-law behaviours at the shock center for density, radial velocity, and temperature, even though pressure distributions from both theory and simulations matched.

It was postulated that the mismatch between MD simulations and TvNS solutions arises from the non-commutativity of the order of taking limits: the solution of the Euler equation after applying the scaling limit (as in the TvNS solution) does not equal applying the scaling limit to the solution of the Navier-Stokes equations that include heat conduction and viscosity.

In particular, the heat conduction term imposes the boundary condition  $\nabla T = 0$  at  $r = 0$ , where  $T$  is the temperature, which the TvNS solution does not satisfy [16]. Recently, it was shown [18, 80] that the results from direct numerical simulations (DNS) of the Navier-Stokes equations, which include heat conduction and viscosity terms, align very well with results from MD simulations of shock propagation in a one-dimensional gas consisting of two types of point particles. These studies argue that the heat conduction term becomes significant at distances very close to the shock center.

## 1.4 Overview of the Thesis

In this thesis, we follow this line of investigation to understand the hydrodynamics of the shock propagation. Analysis up to now was mostly on the blast in a homogeneous medium. For this problem also, it is not clear whether the Navier-Stokes equations

will capture the molecular dynamics simulations in two and higher dimensions where excluded volume effects become important. When the system is inhomogeneous with an initial density  $\rho(r) = \rho_0 r^{-\beta}$ , the role of inhomogeneity is not clear. Likewise the role of inhomogeneity in determining the exponents for splash problem remain unexplored. Finally, for the driven shock, it is not clear at all whether Navier-Stokes equations are the correct description. To address these open issues, we address the following question in this thesis.

### Questions:

1. For shocks following a blast in a homogeneous medium in two and three dimensions, are Navier-Stokes equations the correct hydrodynamics description?
2. For a blast in an inhomogeneous medium with  $\rho(r) = \rho_0 r^{-\beta}$ ,  $0 < \beta < d$ , does the Navier-Stokes describe the numerical data? Is there a critical  $\beta$  for which the Euler equation is the correct description? What are the crossover exponents describing the crossover from core scaling near the shock center to the scaling near the shock front?
3. For splash in an inhomogeneous medium with  $\rho(r) = \rho_0 r^{-\beta}$ ,  $0 < \beta < 1$ , in one dimension, can the exponent characterising energy decay in the medium be calculated exactly? Is the Euler equation sufficient to describe the problem?
4. For driven shocks that are far from equilibrium, does the Euler equation describe the behaviour away from shock front? Do the Navier-Stokes equations describe the behaviour near shock center? What is the role of hard core exclusion?

We address these questions by studying shock propagation using three methods: event driven molecular dynamics simulations, scaling solution of the Euler equation, and the numerical integration of the Navier-Stokes equations.

---



The event driven simulations are done for a mono-disperse hard sphere system in two and three dimensions and bi-disperse point particles in one dimension. All collisions are energy and momentum conserving. Initially all particles are at rest. For the splash problem only the region  $x \geq 0$  is occupied. For other problems, the number density is spherically symmetric  $\rho(r) = \rho_0 r^{-\beta}$ ,  $0 \leq \beta < d$ . For the blast problem, energy is given to a few particles around the origin. For the driven shock, particles within a fixed radius are driven stochastically throughout the simulations.

For the Euler equation, we non-dimensionalise the thermodynamic quantities, and either solve exactly or solve numerically, depending on the equation of state, the resultant ordinary differential equations consistent with Rankine-Hugoniot boundary conditions.

The Navier-Stokes equations cannot be solved analytically. We use MacCormack method to numerically integrate the Navier-Stokes equations. This method is accurate up to second order both in time and space discretisation. The initial condition for the simulations is chosen appropriately depending on the system being studied.

## 1.5 Organisation of Chapters

In Chapter 2, we review the continuity equations of mass, momentum, and energy. From these equations, we derive the Navier-Stokes and Euler equation. We also provide a brief introduction to the Rankine-Hugoniot boundary conditions and derive the jump conditions at the shock front.

In Chapter 3, we describe the computational algorithms used to solve the Navier-Stokes equations (set of partial differential equations) numerically, the rescaled Euler equation (set of ordinary differential equations) numerically, and the algorithm for event-driven molecular dynamics simulations. We validate our numerical methods by benchmarking them against problems with known exact solutions.

The remaining chapters present the original contributions of this thesis.

In Chapter 4, we address the discrepancy between the hydrodynamic description of the blast problem and the results from event-driven molecular dynamics simulations. We compare the direct numerical solutions of the Navier-Stokes equations with simulation data in both two and three dimensions. The excellent agreement between the Navier-Stokes equations and simulation results demonstrates that the Navier-Stokes equations accurately describes the shock problem. We show that truncating the virial equation of state at the 10th virial term introduces negligible error, and the thermodynamic profiles for a hard-sphere gas remain consistent as long as the equation of state represents the hard-sphere gas. We also identify the parametric dependence of thermodynamic quantities: changing the coefficient of viscosity while keeping the coefficient of heat conduction fixed does not affect the numerical results, whereas altering the heat conduction while keeping viscosity fixed does affect the results. However, these changes do not influence the power-law behaviour of the thermodynamic quantities near the shock center.

In Chapter 5, we generalise the blast problem from a homogeneous medium to an inhomogeneous medium. We compare the exact solution of the Euler equation with molecular dynamics simulation results in one dimension and find that the exact solutions do not match the simulation results, except for a critical value of the inhomogeneity parameter. In contrast, the numerical solution of the Navier-Stokes equations shows excellent agreement with the simulation data. For the critical inhomogeneity parameter, all thermodynamic quantities from the Euler equation, Navier-Stokes equations, and molecular simulations converge to identical profiles. Our parametric study for this case shows that the thermodynamic profiles change quantitatively when varying the coefficient of heat conduction while keeping the coefficient of bulk viscosity fixed, and vice versa. Additionally, we identify a new length scale and scaling law for thermodynamic quantities near the shock center,

where heat conduction dominates the Euler terms.

In Chapter 6, we investigated the splash problem where energy is initially input into a system consisting of a vacuum region and an inhomogeneous medium where the initial density distribution varies as a power law with radial distance. At long times, the energy of the inhomogeneous medium decays as power law in time, which does not allow for determination of all the exponents using scaling analysis. Instead, we derived the values of the exponents and other thermodynamic quantities for different values of inhomogeneity parameter by solving the Euler equation using self-similarity of the second kind, and we validated the results through event-driven molecular simulations in one dimension.

In Chapter 7, we study the driven shock problem in two as well as in three dimensional homogeneous medium, where the system is continuously driven by energy injection from a localised region near the center. In this scenario, the system is taken far from equilibrium by this external energy source, making the applicability and solubility of the Navier-Stokes equations questionable. We compare the solution of the Euler equation with molecular dynamics simulation results and find a significant mismatch. However, the direct numerical solution of the Navier-Stokes equations shows good agreement with the simulation data. Our parametric study for this system exhibits behaviour similar to the blast problem: truncating the virial equation of state at the 10th term introduces negligible error, and varying the coefficient of viscosity while keeping the coefficient of heat conduction fixed does not affect the results, whereas altering the heat conduction while holding viscosity constant does change the results. Nonetheless, the power-law behaviour of different thermodynamic quantities near the shock center remains unaffected by these changes.



# 2

## Hydrodynamics

In this chapter, we will review the continuity equations for mass, momentum, and energy. We will derive the Navier-Stokes equations, which incorporate the continuity equations up to second-order derivatives of thermodynamic quantities. In special cases, the Navier-Stokes equations reduce to the Euler equation. Furthermore, we describe the shock wave jump conditions caused due to the perturbations by the external source, the Rankine-Hugoniot boundary conditions, and these conditions are useful to solve the Euler equation.

The perturbation caused by the source can be either small or large. A perturbation that results in flow velocity exceeding the speed of sound is classified as a high perturbation in gas dynamics. A key quantity that determines the scale of the perturbation is the Mach number, defined as the ratio of flow velocity to the speed of sound. Flows with a Mach number less than 1 are considered subsonic, while flows with a Mach number greater than 1 are classified as supersonic in gas dynamics.

## 2.1 Gas dynamics

The flow of a fluid is described by local thermodynamic fields such as density, velocity, temperature, and pressure. A fluid can be classified as compressible or incompressible, depending on how its density varies in response to changes in flow velocity, pressure, or temperature. A fluid is considered incompressible if changes in density remain nearly constant in response to variations in temperature or pressure. In contrast, it is treated as compressible if the changes in density relative to its initial value cannot be neglected.

Shock propagation occurs in supersonic flow with high Mach numbers, resulting in significant density compression. Therefore, the evolution of thermodynamic quantities is described by compressible fluid dynamics. The theories of gas dynamics have evolved continuously over the years, with foundational contributions beginning in the seventeenth century. Early developments in gas dynamics were made by Isaac Newton, Daniel Bernoulli, Leonhard Euler, Robert Boyle, and Jacques Charles, who enhanced the understanding of gas behaviour under force, flow through nozzles and channels, and compressible flows. Further advancements occurred in the nineteenth and twentieth centuries through the work of William Rankine, Pierre-Simon Laplace, Ernst Mach, Henri St. Venant, Adhémar Barré de Saint-Venant, Theodore von Kármán, Ludwig Prandtl, Hugoniot, Geoffrey Ingram Taylor, and John von Neumann, who contributed to the understanding of supersonic and hypersonic flows. Gas dynamics has numerous applications in modern technologies and industries, including aerospace engineering (aircraft design, spacecraft, rocket propulsion, jet engines, and ballistics), nuclear explosions and shock waves, automotive aerodynamics, meteorology and climate science, industrial processes (gas turbines, compressors, and chemical reactors), environmental and energy applications (air pollution, wind energy, and dispersal of airborne particles), and astrophysics (the evolution of stars and galaxies).

---

### 2.1.1 Continuity Equations

The continuity equations for mass, momentum, and energy form the foundation of gas dynamics. These equations describe the evolution of various thermodynamic quantities. The continuity equation for a given quantity is derived by considering the algebraic sum of the rate of change of that quantity within a control volume and its total flux across the surface, equating this to the external influences acting on the quantity.

#### Continuity of Mass

The total mass of the system must be conserved, which can be expressed as:

*“The rate of change of total mass in the control volume  $V$  plus the total mass crossing the surface per time due to material transfer through the surface  $S$  equals zero.”*

This can be written in integral form as:

$$\frac{d}{dt} \int_V \rho dv + \int_S \rho \vec{u} \cdot d\vec{S} = 0, \quad (2.1)$$

or in differential form as:

$$\partial_t \rho + \vec{\nabla} \cdot (\rho \vec{u}) = 0, \quad (2.2)$$

where  $\rho$  and  $\vec{u}$  are the local density and velocity, respectively, and  $S$  denotes the surface area bounding the control volume.

#### Continuity of Momentum

According to the conservation of momentum, the rate of change of momentum within the control volume must equal the external forces acting on it. This can be formu-

---

lated as:

*“The rate of change of total momentum in the control volume  $V$  plus the total momentum transferred through  $S$  plus the resultant force due to stress on  $S$  equals the external force.”*

This can be expressed in integral form as:

$$\frac{d}{dt} \int_V \rho \vec{u} dv + \int_S \rho \vec{u} \vec{u} \cdot d\vec{S} - \int_S P d\vec{S} = \int_V \vec{f} dv, \quad (2.3)$$

where  $P$  represents the stress tensor due to the surrounding gas and  $\vec{f}$  is the external force acting on the control volume. The term  $\int_S P_{ij} d\vec{S}_j$  denotes the  $i^{th}$  component of the resultant force due to stress on the control volume:

$$F_i = \int_S P_{ij} dS_j. \quad (2.4)$$

Here, repeated indices are summed over, and  $P_{ij}$  is the  $ij^{th}$  element of the stress tensor, which is a symmetric matrix. The differential form of Eq. 2.3 is given by:

$$\rho \partial_t u_i + \rho u_j \partial_j u_i - \partial_j P_{ij} = \vec{f}. \quad (2.5)$$

## Continuity of Energy

According to the conservation of energy:

*“The rate of change of total energy in the control volume  $V$  plus the total energy transported per time due to transfer of particles through the surface  $S$  plus the work done per time due to stress acting on the surface  $S$  plus heat loss or gain per time due to conduction through the surface equals zero.”*

---



This can be written in integral form as:

$$\frac{d}{dt} \int_V \left( \frac{1}{2} \rho u^2 + \frac{\rho T}{\gamma - 1} \right) dv + \int_S \left( \frac{1}{2} \rho u^2 + \frac{\rho T}{\gamma - 1} \right) \vec{u} \cdot d\vec{S} - \int_S \vec{u} \cdot P d\vec{S} + \int_S \vec{q} \cdot d\vec{S} = 0, \quad (2.6)$$

or in differential form as:

$$\partial_t \left( \frac{1}{2} \rho u^2 + \frac{\rho T}{\gamma - 1} \right) + \vec{\nabla} \cdot \left( \left( \frac{1}{2} \rho u^2 + \frac{\rho T}{\gamma - 1} \right) \vec{u} \right) - \vec{\nabla} \cdot (\vec{u} P) + \vec{\nabla} \cdot \vec{q} = 0, \quad (2.7)$$

where  $\frac{\rho T}{\gamma - 1}$  and  $\frac{\rho u^2}{2}$  represent the total energy density and total kinetic energy density of the control volume, respectively. Here,  $\vec{q}$  denotes heat conduction,  $\gamma$  is the adiabatic constant, and  $\vec{\nabla} \cdot (\vec{u} P) = \partial_i u_j P_{ij}$ .

## 2.2 Navier-Stokes equations

The Navier-Stokes equations incorporate contributions from various thermodynamic quantities up to their second-order partial derivatives in the continuity equations.

In the Navier-Stokes framework, the pressure tensor is expressed as follows:

$$P_{ij} = -p \delta_{ij} - \frac{2}{d} \mu \frac{\partial u_k}{\partial x_k} \delta_{ij} + \mu \left[ \frac{\partial u_j}{\partial x_i} + \frac{\partial u_i}{\partial x_j} \right] + \zeta \frac{\partial u_k}{\partial x_k} \delta_{ij}, \quad (2.8)$$

$$q_j = -\lambda \frac{\partial T}{\partial x_j}, \quad (2.9)$$

where  $p$  is the pressure,  $d$  is the dimension of the system, and  $\delta_{ij}$  is the Kronecker delta function. The parameters  $\mu$ ,  $\zeta$ , and  $\lambda$  represent the coefficients of viscosity, bulk viscosity, and heat conduction, respectively.

Under this stress tensor, the continuity equations can be written as:

$$\partial_t \rho + \vec{\nabla} \cdot (\rho \vec{u}) = 0, \quad (2.10)$$

$$\begin{aligned} \partial_t (\rho \vec{u}) + \vec{u} \cdot \vec{\nabla} (\rho \vec{u}) + \rho (\vec{u} \cdot \vec{\nabla}) \vec{u} + \vec{\nabla} p &= [\vec{\nabla} (\vec{u} \cdot \vec{\nabla} \mu) - (\vec{u} \cdot \vec{\nabla}) \vec{\nabla} \mu + (\vec{\nabla} \mu \cdot \vec{\nabla}) \vec{u}] \\ &+ \mu [\vec{\nabla} (\vec{\nabla} \cdot \vec{u}) + \vec{\nabla}^2 \vec{u}] - \frac{2}{d} \vec{\nabla} (\mu \vec{\nabla} \cdot \vec{u}) + \vec{\nabla} (\zeta \vec{\nabla} \cdot \vec{u}), \end{aligned} \quad (2.11)$$

$$\begin{aligned} \partial_t \left( \frac{1}{2} \rho u^2 + \frac{\rho T}{\gamma - 1} \right) + \vec{\nabla} \cdot \left[ \left( \frac{1}{2} \rho u^2 + \frac{\rho T}{\gamma - 1} + p \right) \vec{u} \right] &= \vec{\nabla} \cdot [\mu (\vec{u} \cdot \vec{\nabla}) \vec{u}] \\ &+ \vec{\nabla} \cdot \left[ \mu \vec{\nabla} \left( \frac{u^2}{2} \right) \right] - \frac{2}{d} \vec{\nabla} \cdot (\mu \vec{u} \vec{\nabla} \cdot \vec{u}) + \vec{\nabla} \cdot (\zeta \vec{u} \vec{\nabla} \cdot \vec{u}) + \vec{\nabla} \cdot (\lambda \vec{\nabla} T). \end{aligned} \quad (2.12)$$

Eqs. (2.10)–(2.12) represent the continuity equations for mass, momentum, and energy, respectively.

## 2.3 Euler equation

The Euler equation describes the motion of a fluid by considering only the contribution of the surrounding pressure, neglecting the effects of viscosity. In this case, the pressure tensor is given by  $P_{ij} = -p\delta_{ij}$ . The Euler equation can be expressed as:

$$\rho (\partial_t + \vec{u} \cdot \vec{\nabla}) \vec{u} + \vec{\nabla} p = \vec{f}, \quad (2.13)$$

where  $\rho$  is the fluid density,  $\vec{u}$  is the velocity field,  $p$  is the pressure, and  $\vec{f}$  represents any external body forces acting on the fluid.

## 2.4 Surface of shock and boundary condition

In gas dynamics, continuous flows are characterised by thermodynamic quantities that vary smoothly. However, when the flow encounters surfaces, such as normal shocks, these quantities can become discontinuous and change abruptly. Normal shocks occur when the fluid flow interacts with the shock front head-on. The values of the quantities on both sides of the shock must satisfy specific boundary conditions.

Consider a quantity  $Q$  that becomes discontinuous across the shock surface  $R(t)$ . Its flux can be expressed as:

$$\frac{d}{dt} \int_V Q dv + \int_S \vec{J} \cdot d\vec{S} = 0. \quad (2.14)$$


---

Close to the shock, we can assume the flux is one-dimensional. In the rest frame of the shock surface, which moves with speed  $U = \dot{R}(t)$ , the flux on the  $i^{th}$  side of the surface is given by  $J_i - Q_i U$ . Assuming there are no sinks or sources at the surface, the integral form of the flux becomes:

$$[J - QU]_1^2 = 0, \quad (2.15)$$

where 1 and 2 represent the regions on either side of the shock front. Equation (2.15) is known as the general form of the Rankine-Hugoniot boundary condition [3].

Without considering heat conduction and viscosity, the flux forms of the continuity equations are:

$$\partial_t \rho + \vec{\nabla} \cdot (\rho \vec{u}) = 0, \quad (2.16)$$

$$\partial_t (\rho \vec{u}) + \vec{\nabla} \cdot (\rho u^2 + p) = 0, \quad (2.17)$$

$$\partial_t \left( \frac{1}{2} \rho u^2 + \frac{\rho T}{\gamma - 1} \right) + \vec{\nabla} \cdot \left( \left( \frac{1}{2} \rho u^2 + \frac{\rho T}{\gamma - 1} + p \right) \vec{u} \right) = 0. \quad (2.18)$$

The Rankine-Hugoniot boundary conditions for the thermodynamic quantities are:

$$[\rho(u - U)]_1^2 = 0, \quad (2.19)$$

$$[\rho u(u - U) + p]_1^2 = 0, \quad (2.20)$$

$$\left[ \left( \frac{1}{2} \rho u^2 + \frac{\rho T}{\gamma - 1} \right) (u - U) + up \right]_1^2 = 0. \quad (2.21)$$

These equations are essential for solving the Euler equation.



# 3

## Computational Methods

In this chapter, we provide a brief overview of the computational methods essential for studying shock propagation through various approaches. The methods discussed include:

- **Event-Driven Molecular Dynamics Simulations:** Used to investigate shock phenomena in microscopic particle-based models.
- **Numerical Schemes for Euler Equations:** Approaches to solve the ordinary differential equations (ODEs) relevant to elastic hard sphere gases.
- **Numerical Schemes for Navier-Stokes Equations:** Techniques for solving the partial differential equations (PDEs) governing fluid dynamics.

### 3.1 Event-Driven Molecular Dynamics

Event-driven molecular dynamics (EDMD) is a microscopic particle-based simulation technique. Unlike traditional molecular dynamics (MD), which updates the

---

velocities and positions of particles by integrating the equations of motion at fixed time intervals, EDMD advances in time based on the occurrence of events that cause significant changes in particle dynamics, such as collisions and interactions. For a given interaction potential  $w(r_{ij})$  between particles  $i$  and  $j$ , Newton's equation of motion gives the resultant force on particle  $i$  as:

$$m_i \ddot{\vec{r}}_i = - \sum_{j=1, j \neq i}^N \vec{\nabla} w(r_{ij}), \quad (3.1)$$

where  $m_i$ ,  $\vec{r}_i$ , and  $\ddot{\vec{r}}_i$  represent the mass, position, and acceleration of particle  $i$ , respectively. The distance between particles  $i$  and  $j$  is given by  $r_{ij} = |\vec{r}_i - \vec{r}_j|$ . Solving the force equation analytically becomes challenging, especially with a large number of particles  $N$ , making molecular dynamics a useful tool for obtaining approximate numerical results. For large  $N$ , force calculations are time-consuming, rendering traditional MD simulations inefficient; however, EDMD simulations are significantly faster in such scenarios.

EDMD simulations are particularly efficient for dilute hard sphere systems where particles interact solely through collisions. The algorithm skips the integration of the equations of motion and directly jumps to the next event, typically a collision, enhancing simulation efficiency [81]. The interaction potential for hard spheres is given by:

$$w(r_{ij}) = \begin{cases} \infty & \text{if } 0 \leq r_{ij} \leq a_i + a_j, \\ 0 & \text{if } r_{ij} > a_i + a_j, \end{cases} \quad (3.2)$$

where  $a_i$  is the radius of particle  $i$ . This potential implies that the duration of contact during collisions is instantaneous, and particles move ballistically until their next collision, allowing for the prediction of all possible future collision events given the initial conditions of particle velocities and positions.

The core of the EDMD algorithm lies in predicting and executing events. To determine the earliest collision, one must calculate the time taken for all possible collisions. The total number of possible pair collisions for a particle with others can scale as  $O(N^2)$ , which can be computationally expensive. Since a particle can only collide with its neighbouring particles, the calculation can be limited to pair collisions with neighbours. To facilitate this, the system is divided into cells of finite size, introducing an additional event type called cell-crossing. In a cell-crossing event, a particle crosses one of the boundaries of a cell and enters a new cell. The cells contain information about particles based on their coordinates, aiding in the identification of neighbouring particles.

The steps of the algorithm for a simple EDMD simulation of hard sphere gas in the absence of external forces are as follows:

**1. Setup the Initial Conditions:**

- Define parameters, boundary conditions, cell size, etc.
- Assign velocities and positions to the particles.

**2. Predict the Events:**

- Determine all future collision times for all particles with their neighbours.
- Determine all cell-crossing times for particles crossing the boundaries of their respective cells.

**3. Identify the Next Event and Execute:**

- Determine the event type and time.
- Update the system time to the event time.
  - Since particles move ballistically until their collision, their position

at the current event time  $t_e$  can be determined as:

$$\vec{r}_i(t_e) = \vec{r}_i(t_{e-1}) + \vec{u}_i(t_{e-1})(t_e - t_{e-1}), \quad (3.3)$$

where  $t_{e-1}$  is the time of the last event occurrence with  $t_{e-1} < t_e$ . The values  $\vec{u}_i(t_{e-1})$  and  $\vec{r}_i(t_{e-1})$  are the velocity and position of particle  $i$  just after the last event at time  $t_{e-1}$ .

- For collision-type events:
  - Calculate the new velocities of the particles due to the elastic collision at event time  $t_e$ :

$$\vec{u}'_i = \vec{u}_i - \frac{2m_j}{m_i + m_j} \left( (\vec{u}_i - \vec{u}_j) \cdot \left( \frac{\vec{r}_i - \vec{r}_j}{|\vec{r}_i - \vec{r}_j|^2} \right) \right) (\vec{r}_i - \vec{r}_j), \quad (3.4)$$

$$\vec{u}'_j = \vec{u}_j - \frac{2m_i}{m_i + m_j} \left( (\vec{u}_j - \vec{u}_i) \cdot \left( \frac{\vec{r}_i - \vec{r}_j}{|\vec{r}_i - \vec{r}_j|^2} \right) \right) (\vec{r}_i - \vec{r}_j), \quad (3.5)$$

where  $m_i$  is the mass of particle  $i$ . Since the particles are smooth and elastic, the tangential relative velocity remains unchanged, while only the normal relative velocity changes.

- Predict future events for these particles  $i$  and  $j$ , and update the upcoming events.
- For cell-crossing type events:
  - Remove the particle from the current cell and assign it to a new cell based on its coordinates after the crossing.
  - Predict future events for this particle and update the upcoming events.

4. Repeat step : 3 until the desired simulation time.

Although the introduction of cells increases the number of events, it reduces the computation of collisions after each event, thereby minimising unnecessary time

---



consumption in the simulation.

## 3.2 Numerical methods to solve ordinary differential equations :

Although exact solutions for shock propagation, such as the TvNS solution and Dokuchaev's solution, are available, obtaining an exact solution to the Euler equations is not always feasible. This is particularly true when the initial conditions are altered or when shock propagation occurs in gases characterised by complicated equations of state. In such cases, a numerical approach is necessary to solve the rescaled form of the Euler equations, which are coupled ordinary differential equations (ODEs). In this section, we describe the numerical method for solving these ODEs under specified boundary conditions and benchmark the algorithm by comparing the numerical results of driven shocks with Dokuchaev's solution.

To maintain consistency in this chapter, we reproduce the Euler equations. For a driven shock in three dimensions, where the total energy of the system increases over time  $t$  as  $E(t) = E_0 t^\delta$ , the equations in terms of non-dimensionalised functions  $\tilde{R}(\xi)$ ,  $\tilde{u}(\xi)$ ,  $\tilde{T}(\xi)$ , and  $\tilde{P}(\xi)$  for an ideal gas are given by:

$$(\alpha - \tilde{u}) \frac{d \log \tilde{R}}{d \log \xi} - \frac{d \tilde{u}}{d \log \xi} = 3 \tilde{u}, \quad (3.6)$$

$$(\tilde{u} - \alpha) \frac{d \tilde{u}}{d \log \xi} + \tilde{T} \frac{d \log \tilde{R}}{d \log \xi} + \frac{d \tilde{T}}{d \log \xi} + \tilde{u}[\tilde{u} - 1] + 2 \tilde{T} = 0, \quad (3.7)$$

$$\tilde{T} = \frac{\tilde{u}^2 (\alpha - \tilde{u}) (\gamma - 1)}{2(\gamma \tilde{u} - \alpha)}, \quad (3.8)$$

where  $\alpha = \frac{2+\delta}{5}$ ,  $\gamma = \frac{5}{3}$ , and  $\xi = \frac{r}{R(t)}$ . At the shock front, the Rankine-Hugoniot boundary conditions for these rescaled functions are given by:

$$\tilde{R}(\xi = \xi_f) = 4, \quad (3.9)$$

$$\tilde{u}(\xi = \xi_f) = \frac{3\alpha}{4}, \quad (3.10)$$

$$\tilde{T}(\xi = \xi_f) = \frac{3\alpha^2}{16}, \quad (3.11)$$

where  $\xi_f$  is the position of the shock front. Assuming

$$I_e = 4\pi \int_0^{\xi_f} \left( \frac{\tilde{R}\tilde{u}^2}{2} + \frac{\tilde{R}\tilde{T}}{\gamma-1} \right) \xi^4 d\xi, \quad (3.12)$$

the value of  $\xi_f$  is bounded by the energy constraint  $E(t) = E_0 t^\delta$  as

$$I_e = 1.0. \quad (3.13)$$

The exact solution of the Euler equations (3.6)–(3.8) with boundary conditions (3.9)–(3.11) is possible. More details about the problem can be found in Sec. 7.2, with the exact solution provided in the Chapter 7.

The numerical procedure to solve these ODEs using the Rankine-Hugoniot boundary conditions is as follows. Begin with an initial value for  $\xi_f$  and solve the Euler equations (3.6)–(3.8) for the scaling functions. Using this solution, calculate the value of  $I_e$ . If  $I_e < 1$ , increase the value of  $\xi_f$  and resolve the Euler equations; if  $I_e > 1$ , decrease the value of  $\xi_f$  and resolve again. This iterative process continues until  $I_e$  satisfies Equation (3.13). A schematic diagram of this numerical process is shown in Fig. 3.1. All numerical integrations to solve the Euler equations are performed using *MATHEMATICA*.

To benchmark this algorithm, we compare the numerical solutions of the Euler equations (3.6)–(3.8) with Dokuchaev's solution (see the Chapter 7) in Fig. 3.2 for four different values of  $\delta = 0.0, 0.5, 1.0, 1.5$ . In Fig. 3.2, the numerical and exact solutions align well, indicating that the numerical procedure is correct.

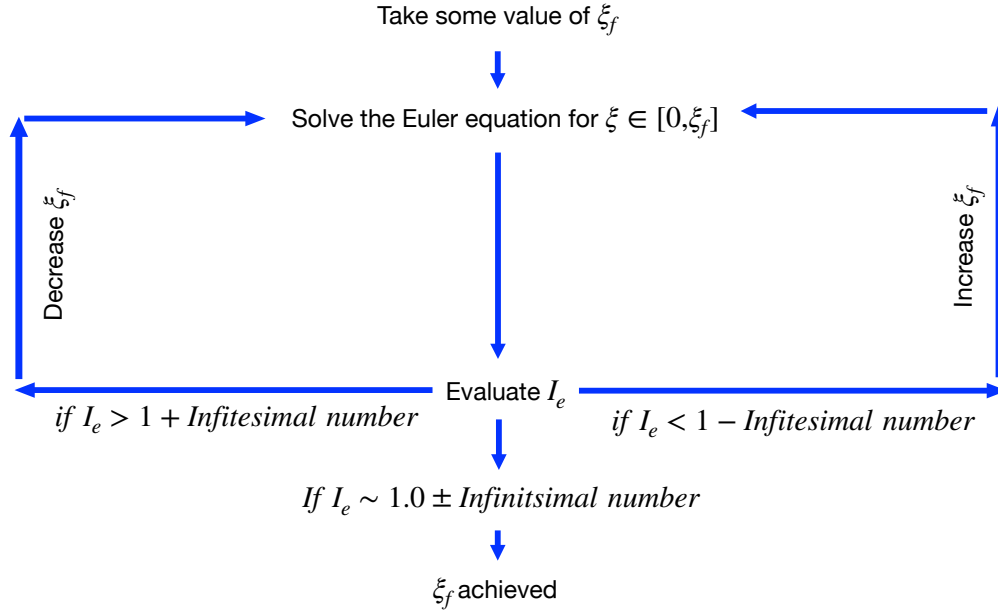


Figure 3.1: Schematic diagram of the numerical algorithm to solve ordinary differential equations (3.6)–(3.8) under boundary conditions (3.9)–(3.11).

### 3.3 Numerical methods to solve partial differential equations :

The Navier-Stokes equations are a second-order partial differential equation that cannot be solved analytically for studying shock propagation. To tackle this numerically, we employ the MacCormack method [82]. In this method, the spatial domain is discretised into bins of size  $\Delta x$ , and the system is integrated from time  $t$  to  $t + \Delta t$  using the values of the quantities at time  $t$  from all the bins. Each time interval  $\Delta t$  involves two steps: the predictor step and the corrector step. The predictor step uses forward differentiation, while the corrector step uses backward differentiation, or vice versa. This method provides up to second-order accuracy in both time discretisation  $\Delta t$  and space discretisation  $\Delta x$ .

The numerical algorithm for the MacCormack method is as follows. Consider a partial differential equation (PDE) to be solved under the initial condition  $u(x, t =$

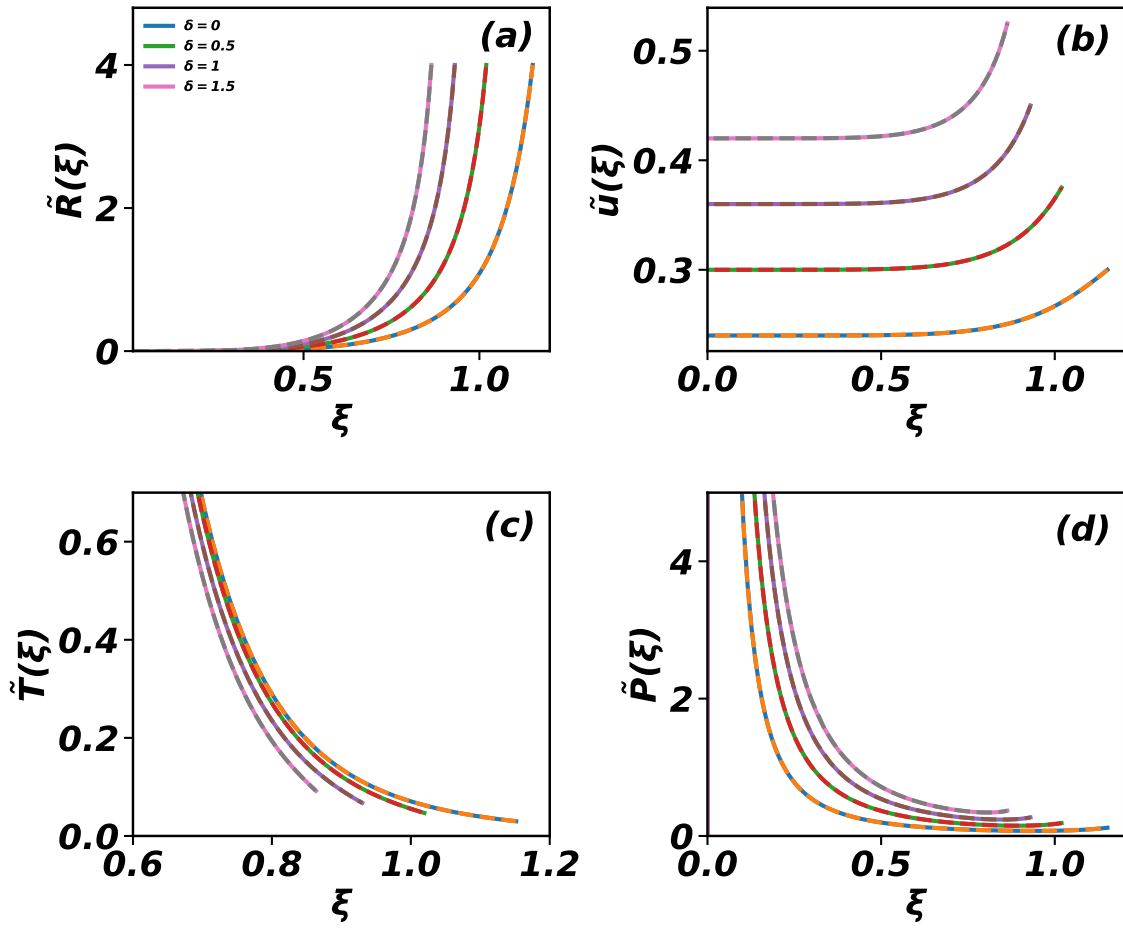


Figure 3.2: Comparison of the solutions of the Euler equations (3.6)–(3.8) using Rankine-Hugoniot boundary conditions (Eqs. (3.9)–(3.11)) for four different values of  $\delta = 0, 0.5, 1, 1.5$ . The solid lines represent the exact solution of the Euler equations (see the Chapter 7), while the dashed lines represent the numerical solution obtained using the algorithm in Fig. 3.1.

$0) = u_0$  and the boundary condition  $u(x = \pm L, t) = u_0$ , which has the form:

$$\partial_t u = f(x, \partial_x u), \quad (3.14)$$

First, define all parameter values and bins. Solve the PDE from time 0 to  $\Delta t$  as follows: take the initial values and compute the predictor values  $u_p$  in each bin using forward differentiation:

$$u_p(x, t) = u(x, t) + f(u, \partial_x u) \Delta t. \quad (3.15)$$

Next, use these predictor values to compute the corrector values  $u_c$  using backward

---

differentiation:

$$\left(\frac{\partial u}{\partial t}(x, t)\right)_c = f(u_p, \partial_x u_p). \quad (3.16)$$

The final value at time  $\Delta t$  is given by:

$$u(x, t + \Delta t) = \frac{u(x, t) + u_p(x, t)}{2} + \frac{1}{2} \left(\frac{\partial u}{\partial t}(x, t)\right)_c \Delta t. \quad (3.17)$$

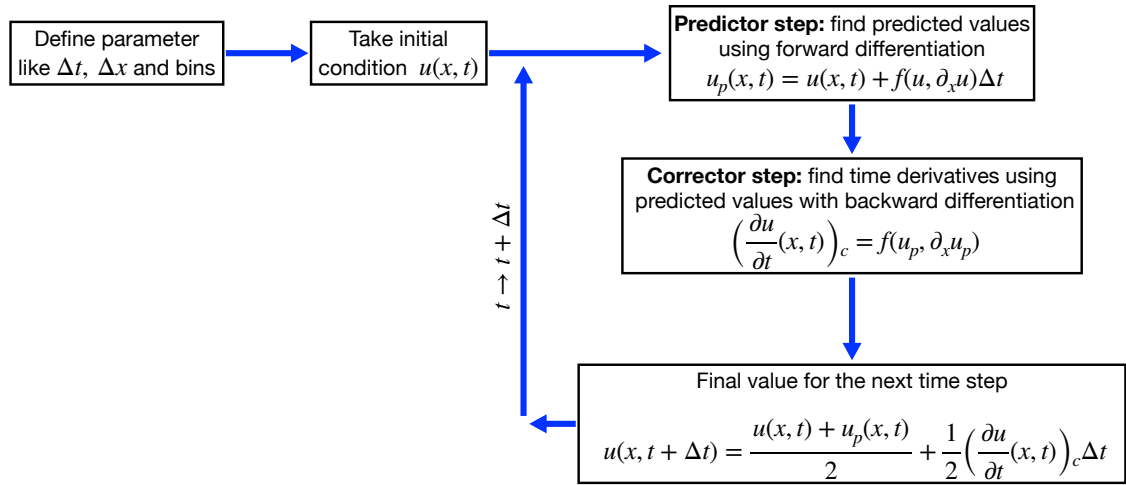


Figure 3.3: Schematic diagram of the MacCormack method for solving the partial differential equation (3.14).

The forward differentiation in the predictor step and the backward differentiation in the corrector step are defined as follows:

$$\partial_x u|_{forward} = \frac{u(x + \Delta x, t) - u(x, t)}{\Delta x}, \quad (3.18)$$

$$\partial_x u_p|_{backward} = \frac{u_p(x, t) - u_p(x - \Delta x, t)}{\Delta x}. \quad (3.19)$$

To benchmark this numerical algorithm, we solve the heat equation in one dimension:

$$\frac{\partial u(x, t)}{\partial t} = \alpha \frac{\partial^2 u(x, t)}{\partial x^2}, \quad (3.20)$$

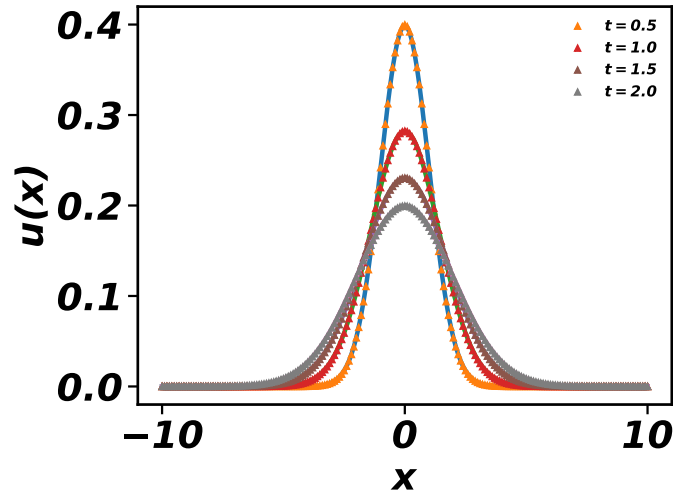


Figure 3.4: Solution of the heat equation (3.20) with initial condition (3.21) at four different times  $t = 0.5, 1.0, 1.5, 2.0$ . The symbols represent the numerical solution using the MacCormack method, while the solid lines represent the exact solution (see (3.22)). The parameter values are set as:  $\Delta t = 0.001$ ,  $\Delta x = 0.1$ ,  $\alpha = 1.0$ .

where  $\alpha$  is a constant. The initial condition is given by:

$$u(x, 0) = \begin{cases} 0 & \text{if } x \neq 0, \\ 1 & \text{if } x = 0, \end{cases} \quad (3.21)$$

with boundary conditions  $u(\pm L, t) = 0$ . The exact solution under this initial condition is:

$$u(x, t) = \frac{1}{\sqrt{4\pi\alpha t}} \exp\left(-\frac{x^2}{4\alpha t}\right). \quad (3.22)$$

We compare the numerical solution of the heat equation obtained using the MacCormack method with the exact solution in Fig. 3.4. In Fig. 3.4, the numerical solution aligns well with the exact solution, demonstrating the high accuracy of the algorithm.

# 4

## Blast Waves in Two and Three Dimensions: Euler Versus Navier–Stokes Equations

### Related Publication :

This chapter is based on the following publication [83]:

Blast waves in two and three dimensions: Euler versus Navier–Stokes equations

**Amit Kumar** and R. Rajesh, *Journal of Statistical Physics*, 188(2):1–14, 2022.



### 4.1 Introduction

The time evolution of a blast wave resulting from an intense explosion is a classic problem in gas dynamics [1–3]. From dimensional analysis, the radius of the shock front  $R(t)$  is known to increase with time  $t$  as a power law  $R(t) \sim (E_0 t^2 / \rho_0)^{1/(d+2)}$  in  $d$  dimensions, where  $E_0$  is the energy of the blast and  $\rho_0$  is the ambient density of the system [4–7, 11].

Analysis up to now was mostly on the blast in a homogeneous medium. For this problem also, it is not clear whether the Navier-Stokes equations will capture the molecular dynamics simulations in two and higher dimensions where excluded volume effects become important.

In this chapter, we ask if Navier-Stokes equations will provide the correct description of the data from MD simulations in two and three dimensions. To do so, we do DNS of the continuity equations for mass, momentum and energy using the same numerical methods followed in Ref. [80]. In continuation of our earlier work [16, 17], steric effects, which are absent in one-dimensional systems, were included by modifying the equation of state that relates pressure to temperature and density from the ideal gas equation of state to the virial equation of state.

The boundary conditions for the equations in radial coordinates are obtained from DNS of the equations in cartesian coordinates. The constants related to heat conduction and viscosity are determined from kinetic theory. We then show that the results from DNS match the data from MD simulations without any fitting parameter in two dimensions. In three dimensions, there is a small mismatch which is resolved by treating the constants appearing in heat conduction and viscosity terms as free parameters. We conclude that to obtain the correct description of a blast wave in the hydrodynamic regime, the solution has to be first found for the Navier-Stokes equations, which includes heat conduction and viscosity terms, followed by taking the appropriate scaling limit.

The remainder of this chapter is organised as follows. In Sec. 4.2, we review the continuity equations to describe hydrodynamics of shock in the spherical polar coordinate in  $d$ -dimensions. The numerical algorithm and the values of the parameters used for DNS are also given. In Sec. 4.3, we show that the results from DNS match with the results from MD of hard spheres in both two and three dimensions. Section 4.4 contains a summary and discussion. The content of this chapter is published



in Ref. [83].

## 4.2 Hydrodynamics and Numerical details

### 4.2.1 Hydrodynamics

We briefly review the hydrodynamics of explosion induced shock propagation in  $d$ -dimensions. Consider a gas of constant density  $\rho_0$  and temperature zero. At time  $t = 0$ , energy  $E_0$  is input isotropically in a localised region around  $r = 0$ . The state of the gas is described by its density field  $\rho(\vec{r}, t)$ , velocity field  $\vec{u}(\vec{r}, t)$ , temperature field  $T(\vec{r}, t)$ , and pressure field  $p(\vec{r}, t)$ . Since mass, momentum and energy are locally conserved, their continuity equations describe the time evolution of the local fields. Since shock propagation is spherically symmetric, the above thermodynamic quantities will depend only on  $r$ .

In spherical polar coordinates, the continuity equations for density, momentum, and energy for a mono-atomic gas are respectively [1, 84],

$$\partial_t \rho + \frac{1}{r^{d-1}} \partial_r (r^{d-1} \rho u) = 0, \quad (4.1)$$

$$\begin{aligned} \partial_t (\rho u) + \frac{1}{r^{d-1}} \partial_r [r^{d-1} \rho u^2] + \partial_r p \\ = \frac{1}{r^{d-1}} \partial_r (2\mu r^{d-1} \partial_r u) - \frac{2\mu(d-1)u}{r^2} + \partial_r \left[ \left( \zeta - \frac{2}{d}\mu \right) \frac{1}{r^{d-1}} \partial_r (r^{d-1} u) \right], \end{aligned} \quad (4.2)$$

$$\begin{aligned} \partial_t \left( \frac{1}{2} \rho u^2 + \frac{\rho T}{\gamma - 1} \right) + \frac{1}{r^{d-1}} \partial_r \left( r^{d-1} \left[ \frac{1}{2} \rho u^2 + \frac{\rho T}{\gamma - 1} + p \right] u \right) = \frac{1}{r^{d-1}} \partial_r (2r^{d-1} \mu u \partial_r u) \\ + \frac{1}{r^{d-1}} \partial_r \left( r^{d-1} u \left[ \zeta - \frac{2}{d}\mu \right] \frac{1}{r^{d-1}} \partial_r (r^{d-1} u) \right) + \frac{1}{r^{d-1}} \partial_r (r^{d-1} \lambda \partial_r T), \end{aligned} \quad (4.3)$$

where  $\gamma = 1 + \frac{2}{d}$ ,  $\mu$  is the coefficient of viscosity,  $\lambda$  is the coefficient of heat conduction, and  $\zeta$  is the bulk viscosity.

The coefficients  $\mu$  and  $\lambda$  increase with temperature as [85, 86]

$$\mu = C_1 \sqrt{T}, \quad (4.4)$$

$$\lambda = C_2 \sqrt{T}, \quad (4.5)$$

where  $C_1$  and  $C_2$  are constants which depend on the size of the particles. From kinetic theory of gases, approximate values of  $C_1$  and  $C_2$  can be obtained for hard spheres. The approximate values of  $C_1$  and  $C_2$  for hard sphere particles of diameter  $D$  are given by [86],

$$C_1^* = \frac{1}{dD^{d-1}} \sqrt{\frac{mk_B}{\pi^{d-1}}} \frac{\left[\Gamma\left(\frac{d+1}{2}\right)\right]^2}{\Gamma\left(\frac{d}{2}\right)}, \quad (4.6)$$

$$C_2^* = \frac{1}{2D^{d-1}} \sqrt{\frac{k_B^3}{m\pi^{d-1}}} \frac{\left[\Gamma\left(\frac{d+1}{2}\right)\right]^2}{\Gamma\left(\frac{d}{2}\right)}, \quad (4.7)$$

where  $m$  is the mass of a particle and  $\Gamma$  is the gamma function. The star in the superscript denotes that the results for  $C_1$  and  $C_2$  are from kinetic theory. The bulk viscosity for mono-atomic gas is usually taken to be zero [87]. In three dimensions, we consider both  $\zeta = 0$  as well as the expression for bulk viscosity given by [88]

$$\zeta = \frac{4}{9} (\rho D^2)^2 \sqrt{\frac{\pi k_B T}{m^3}}. \quad (4.8)$$

Equations (4.1)-(4.3) have four independent fields. If local thermal equilibrium is assumed, as is usually done, then the local pressure  $p$  is expressed in terms of local density  $\rho$  and local temperature  $T$  through an equation of state (EOS). While the ideal gas EOS was used in the original TvNS solution, for a hard sphere gas, steric effects become important and a more realistic EOS would be required in order to compare with results from hard sphere simulations [16, 17, 28]. We choose the EOS to be the virial EOS, which takes the form

$$p = k_B \rho T \left[ 1 + \sum_{i=2}^{\infty} B_i \rho^{i-1} \right], \quad (4.9)$$

where  $B_i$  is  $i^{th}$  virial coefficient. In Table 4.1, we tabulate the values for the first 10

Table 4.1: The numerical values of the virial coefficients  $B_i$  for the hard sphere gas in two and three dimensions. The data are from Ref. [89], and for spheres of diameter one.

$i$	$B_i(d=2)$	$B_i(d=3)$
2	$\frac{\pi}{2}$	$\frac{2\pi}{3}$
3	$(\frac{4}{3} - \frac{\sqrt{3}}{\pi})B_2^2$	$\frac{5}{8}B_2^2$
4	$\left[2 - \frac{9\sqrt{3}}{2\pi} + \frac{10}{\pi^2}\right]B_2^3$	$\left[\frac{2707}{4480} + \frac{219\sqrt{2}}{2240\pi} - \frac{4131}{4480} \frac{\arccos[1/3]}{\pi}\right]B_2^3$
5	$0.33355604B_2^4$	$0.110252B_2^4$
6	$0.1988425B_2^5$	$0.03888198B_2^5$
7	$0.11486728B_2^6$	$0.01302354B_2^6$
8	$0.0649930B_2^7$	$0.0041832B_2^7$
9	$0.0362193B_2^8$	$0.0013094B_2^8$
10	$0.0199537B_2^9$	$0.0004035B_2^9$

virial coefficients.

## 4.2.2 Numerical method

We solve Eqs. (4.1)-(4.3) numerically using the MacCormack numerical integration method [82]. In this scheme, a partial differential equation is solved by using predictor-corrector steps. It has accuracy upto second order both in spatial discretisation  $\Delta r$  and temporal discretisation  $\Delta t$ .

We now describe the parameters that we have used for numerically solving Eqs. (4.1)-(4.3). We choose system size  $L$  and total integration time  $\tau$  such that the shock does not reach the boundary at time  $\tau$ . The initial condition at time  $t = 0$  is: density  $\rho = \rho_0$  everywhere, velocity  $u = 0$  everywhere and temperature  $T = 0$  everywhere except in small region  $0 \leq r \leq \sigma$ . In this small region, we take gaussian temperature profile

$$T(r, 0) = bT_0 \exp\left(-\frac{r^2}{2\sigma^2}\right), \quad (4.10)$$

where we set the temperature scale  $T_0$  to one and choose the dimensionless constant  $b$  to be  $b = 8.35$  in  $d = 2$  and  $b = 6.17$  for  $d = 3$  to match with the values chosen

Table 4.2: The numerical values of different parameters used in solving Eqs. (4.1)-(4.3) in two and three dimensions. All quantities are measured in terms of the length scale  $\ell_0 = D$ , mass scale  $m_0 = m$  and time scale  $\tau_0 = D \sqrt{m/T_0}$ . These scales are set to one by choosing  $D = 1$ ,  $m = 1$  and  $T_0 = 1$  and  $k_B = 1$ .

Parameters	$d = 2$	$d = 3$
$\rho_0$	0.382	0.4
$L$	300	136
$\tau$	8000	10000
$\Delta r$	0.05	0.05
$\Delta t$	$10^{-5}$	$10^{-5}$
$\sigma$	0.5	0.65
$\gamma$	2.0	5/3
$C_1^*$	$\sqrt{\pi}/8$	$2/(3\sqrt{\pi^3})$
$C_2^*$	$\sqrt{\pi}/8$	$1/\sqrt{\pi^3}$

in the event driven simulations. In addition to the initial conditions, we also need the boundary conditions at  $r = 0$  and  $r = L$ . At  $r = 0$ , we impose the boundary conditions  $\partial_r \rho = 0$ ,  $u = 0$ , and  $\partial_r T = 0$ . These boundary conditions are justified by numerically solving the continuity equations in cartesian coordinates, wherein the boundary conditions at the origin need not be specified (see Sec. 4.2.3).

All quantities are measured in terms of the length scale  $\ell_0 = D$ , mass scale  $m_0 = m$  and time scale  $\tau_0 = D \sqrt{m/T_0}$ . These scales are set to one by choosing  $D = 1$ ,  $m = 1$  and  $T_0 = 1$  and  $k_B = 1$ . The numerical values of the different parameters are given in Table 4.2.

### 4.2.3 Solution of Navier-Stokes equations in cartesian coordinates

In this section, we solve the Navier-Stokes equations in two dimensional cartesian coordinates to find the boundary conditions obeyed by the thermodynamic quantities at the shock center. Unlike spherical coordinates, where both the initial conditions as well as boundary conditions at  $r = 0$  have to be provided, in cartesian coordi-

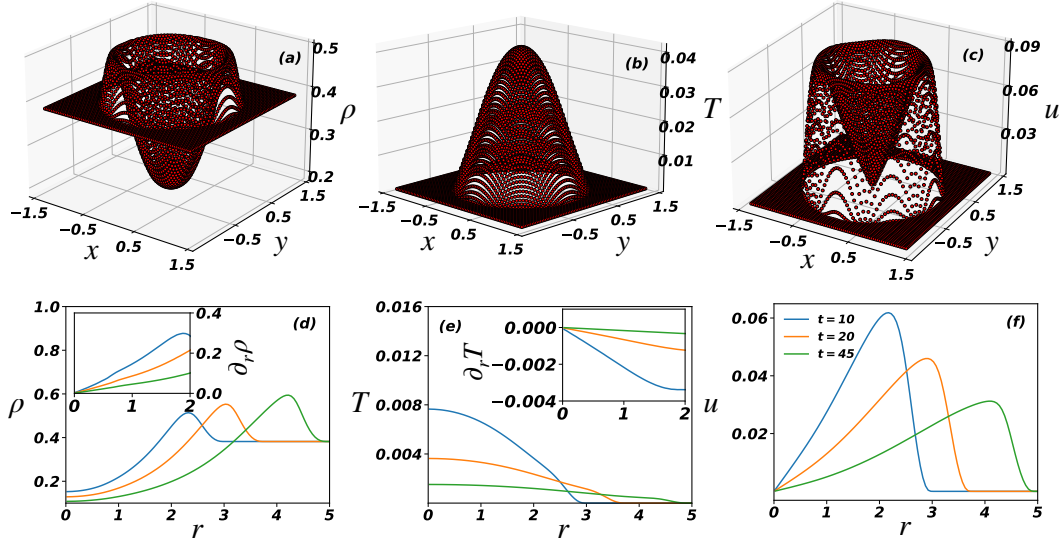


Figure 4.1: The two-dimensional spatial variation of (a) density  $\rho$ , (b) temperature  $T$ , and (c) speed  $u$ , at time  $t = 2.5$ . The corresponding variations with radial distance  $r$  are shown in (d)-(f) for three different times. The insets in (d) and (e) show the variation of  $\partial_r \rho$  and  $\partial_r T$  with  $r$ . The data justifies the boundary conditions at  $r = 0$ :  $\partial_r \rho = 0$ ,  $\partial_r T = 0$ , and  $u = 0$ .

nates only the initial conditions are required for determining the solution at any time. Thus, numerically solving the equations in cartesian coordinates allows us to determine the boundary conditions at  $r = 0$  for the solution in spherical coordinates. The continuity equations for mass, momentum and energy for a mono-atomic gas are given by [1, 3, 84, 85]

$$\partial_t \rho + \vec{\nabla} \cdot (\rho \vec{u}) = 0, \quad (4.11)$$

$$\begin{aligned} \partial_t (\rho \vec{u}) + \vec{u} (\vec{\nabla} \cdot (\rho \vec{u})) + \rho (\vec{u} \cdot \vec{\nabla}) \vec{u} + \vec{\nabla} p = & [\vec{\nabla} (\vec{u} \cdot \vec{\nabla} \mu) - (\vec{u} \cdot \vec{\nabla}) \vec{\nabla} \mu + (\vec{\nabla} \mu \cdot \vec{\nabla}) \vec{u}] \\ & + \mu [\vec{\nabla} (\vec{\nabla} \cdot \vec{u}) + \vec{\nabla}^2 \vec{u}] - \vec{\nabla} (\mu \vec{\nabla} \cdot \vec{u}), \end{aligned} \quad (4.12)$$

$$\begin{aligned} \partial_t \left( \frac{1}{2} \rho u^2 + \rho T \right) + \vec{\nabla} \cdot \left( \left[ \frac{1}{2} \rho u^2 + \rho T + p \right] \vec{u} \right) = & \vec{\nabla} \cdot \left[ \mu (\vec{u} \cdot \vec{\nabla}) \vec{u} \right] + \vec{\nabla} \cdot \left[ \mu \vec{\nabla} \left( \frac{u^2}{2} \right) \right] \\ & - \vec{\nabla} \cdot (\mu \vec{u} \vec{\nabla} \cdot \vec{u}) + \vec{\nabla} \cdot (\lambda \vec{\nabla} T). \end{aligned} \quad (4.13)$$

We solve Eqs. (4.11)-(4.13) in two dimensions using MacCormack method (see Sec. 4.2.2). The pressure is related to temperature and density through the virial

EOS given in Eq. (4.9). We choose the same values of the parameters as in spherical coordinate (see Table 4.2). For spatial discretisation, we use  $dx = dy = dr / \sqrt{2}$ . The initial temperature profile is chosen to be a gaussian. The system size is chosen such that the shock does not reach the boundaries during the times that we have considered.

The spatial variation of density, temperature and speed for a single time  $t$  is shown in Fig. 4.1(a)-(c) respectively. The corresponding variation with radial distance  $r$  are shown in Fig. 4.1(d)-(f). From these data, we can determine the boundary conditions at  $r = 0$ . For all the times shown,  $\partial_r \rho = 0$  at  $r = 0$  [see inset of Fig. 4.1(d)]. Also,  $\partial_r T = 0$  at  $r = 0$  [see inset of Fig. 4.1(e)]. Finally,  $u = 0$  at  $r = 0$  [see Fig. 4.1(f)]. These boundary conditions at  $r = 0$ ,  $\partial_r \rho = 0$ ,  $\partial_r T = 0$ , and  $u = 0$ , are used for the numerical integration of the continuity equations in radial coordinates.

## 4.3 Results

We define non-dimensionalised density  $\tilde{\rho}$ , radial velocity  $\tilde{u}$ , temperature  $\tilde{T}$ , and pressure  $\tilde{P}$  fields. From dimensional analysis [2],

$$\rho(\vec{r}, t) = \rho_0 \tilde{R}(\xi), \quad (4.14)$$

$$u(\vec{r}, t) = \frac{r}{t} \tilde{u}(\xi), \quad (4.15)$$

$$T(\vec{r}, t) = \frac{r^2}{t^2} \tilde{T}(\xi), \quad (4.16)$$

$$p(\vec{r}, t) = \frac{\rho_0 r^2}{t^2} \tilde{P}(\xi), \quad (4.17)$$

where

$$\xi = r \left( \frac{E_0 t^2}{\rho_0} \right)^{-1/(d+2)}, \quad (4.18)$$

is the scaled distance, and  $E_0$  is the initial energy injected into the system. We describe the results for two dimensions in Sec. 4.3.1 and three dimensions in Sec. 4.3.2.

### 4.3.1 Results in two dimensions

For the simulations in two dimensions, we set the bulk viscosity  $\zeta = 0$  [87]. We first describe our main result. Figure 4.2 shows the variation of the different non-dimensionalised observables with  $\xi$  for four different times. The data for different times collapse onto one curve confirming the scaling in Eqs. (4.14)-(4.17). The results from DNS are an excellent match with the results from MD simulations (the MD data are from Ref. [17]) for all the four thermodynamic quantities. In comparison, the TvNS solution, shown by solid black lines, does not describe the data well. We note that there are no fitting parameters used in the simulations, with the values  $C_1^*$  and  $C_2^*$  being calculated from kinetic theory. We conclude that heat conduction and viscosity terms are essential to reproduce the results from MD, though these terms are irrelevant in the scaling limit.

We have used the virial EOS [see Eq. (4.9)] for relating local pressure to density and temperature. However, only ten terms of the expansion are known. To check whether our numerical results are affected by this truncation, we solve the continuity equations by using the virial EOS only upto the  $i^{th}$  term where  $i = 0, 2, 4, \dots, 10$ .  $i = 0$  corresponds to the ideal gas. Figure 4.3 shows the dependence of our results on the number of terms kept in the virial expansion. The results for  $i = 8$  and  $i = 10$  are nearly identical, showing that truncating the virial EOS at the  $10^{th}$  term causes negligible error in the results.

We now probe the sensitivity of the results to the parameters  $C_1$  and  $C_2$  where  $\mu = C_1 \sqrt{T}$  and  $\lambda = C_2 \sqrt{T}$  [see Eqs. (4.4)-(4.5)]. In Fig. 4.4, we show the results for the different thermodynamic quantities for different values of  $C_2$  keeping all other parameters fixed. We choose  $C_2 = C_2^*, 2C_2^*, 4C_2^*$ . For  $C_2 < C_1^*$ , we find that the numerical integration is not stable. Near the shock front, these parameters have negligible effect. On the other hand, near the shock center, the results depend on

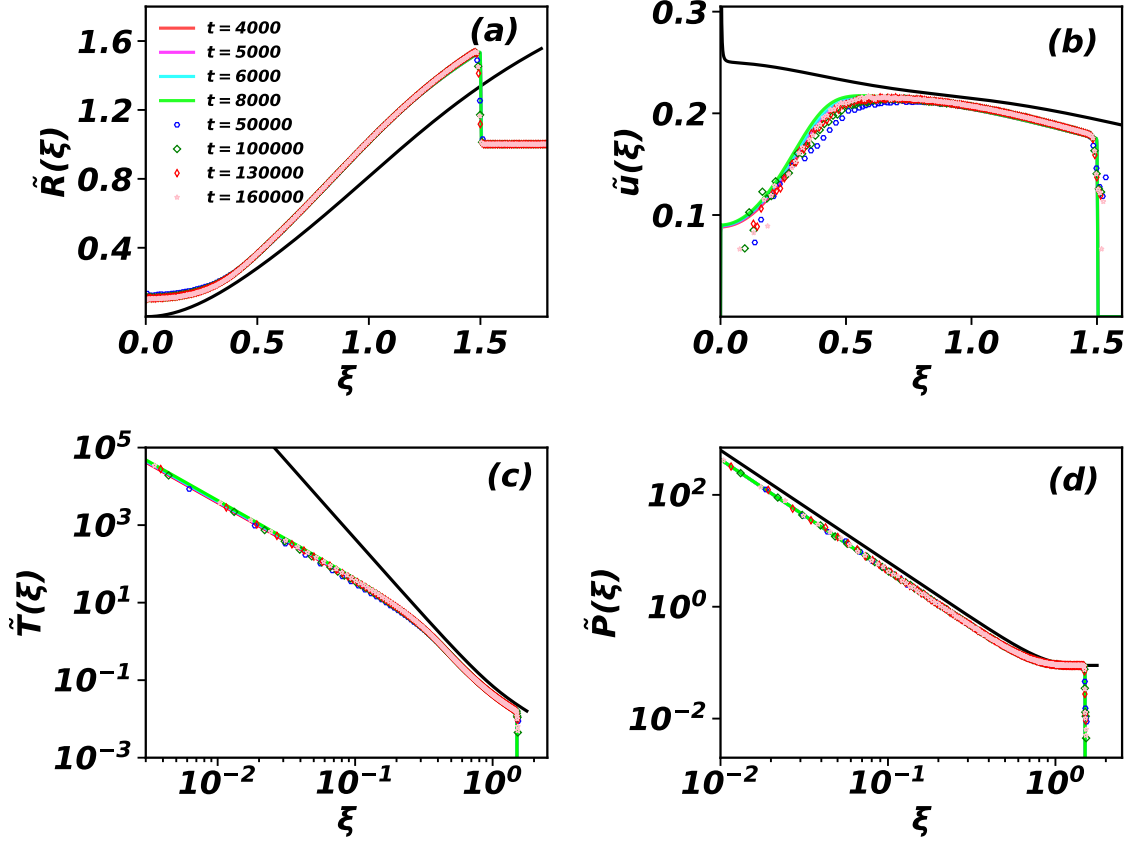


Figure 4.2: The data from MD simulations (taken from Ref. [17]) are compared with the data from DNS of the continuity Eqs. (4.1)-(4.3) in two dimensions. The variation of the non-dimensionalised (a) density (b) radial velocity (c) temperature and (d) pressure with  $\xi$  is shown for four different times (different times for MD and DNS). The symbols represent the MD data and coloured lines represent the results from DNS. The solid black lines represent the TvNS solution with virial EOS. The data are for ambient gas density  $\rho_0 = 0.382$ .



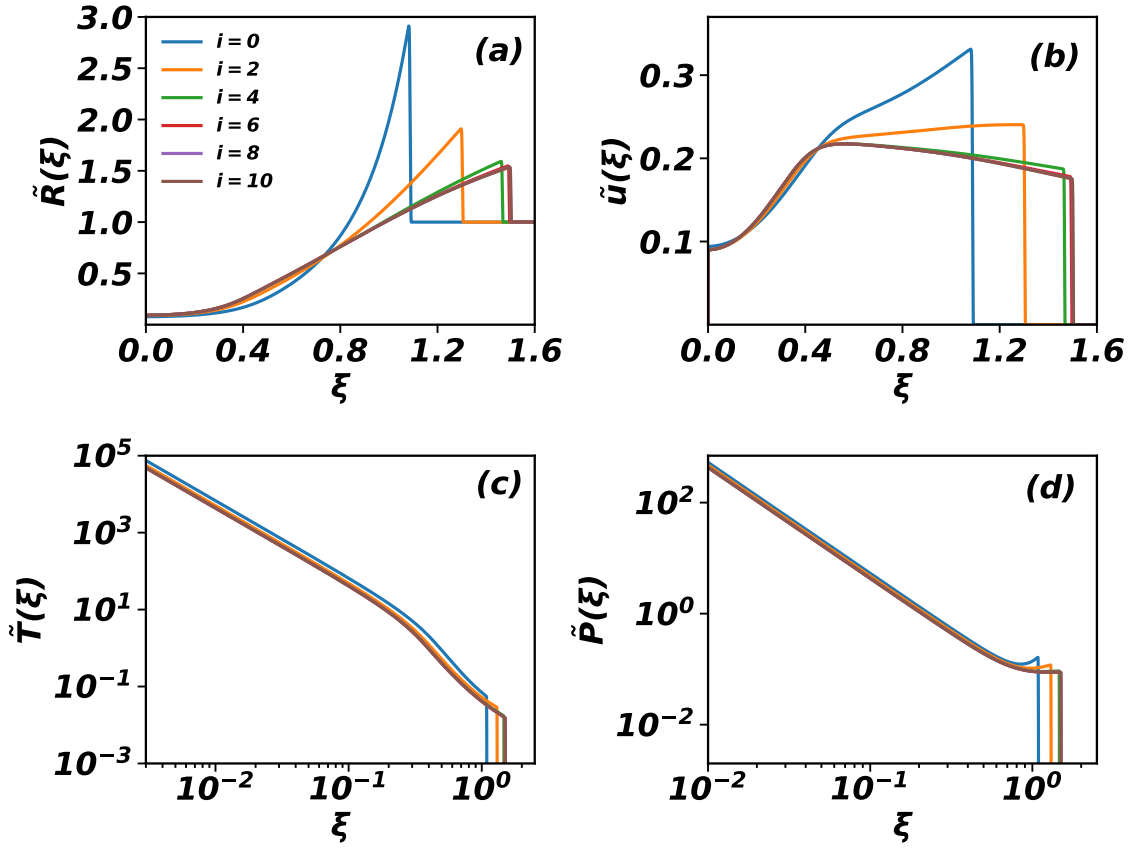


Figure 4.3: The variation of the non-dimensionalised (a) density  $\rho(r)$ , (b) velocity  $u(r)$ , (c) temperature  $T(r)$ , (d) pressure  $p(r)$  obtained from the DNS of the continuity Eqs. (4.1)-(4.3) in two dimensions, when the virial expansion in Eq. (4.9) is truncated at  $i = 2, 4, 6, 8, 10$ . The data for different  $i$  are shown for a single time  $t = 8000$  and ambient density  $\rho_0 = 0.382$ .  $i = 0$  corresponds to ideal EOS  $p = \rho T$ .

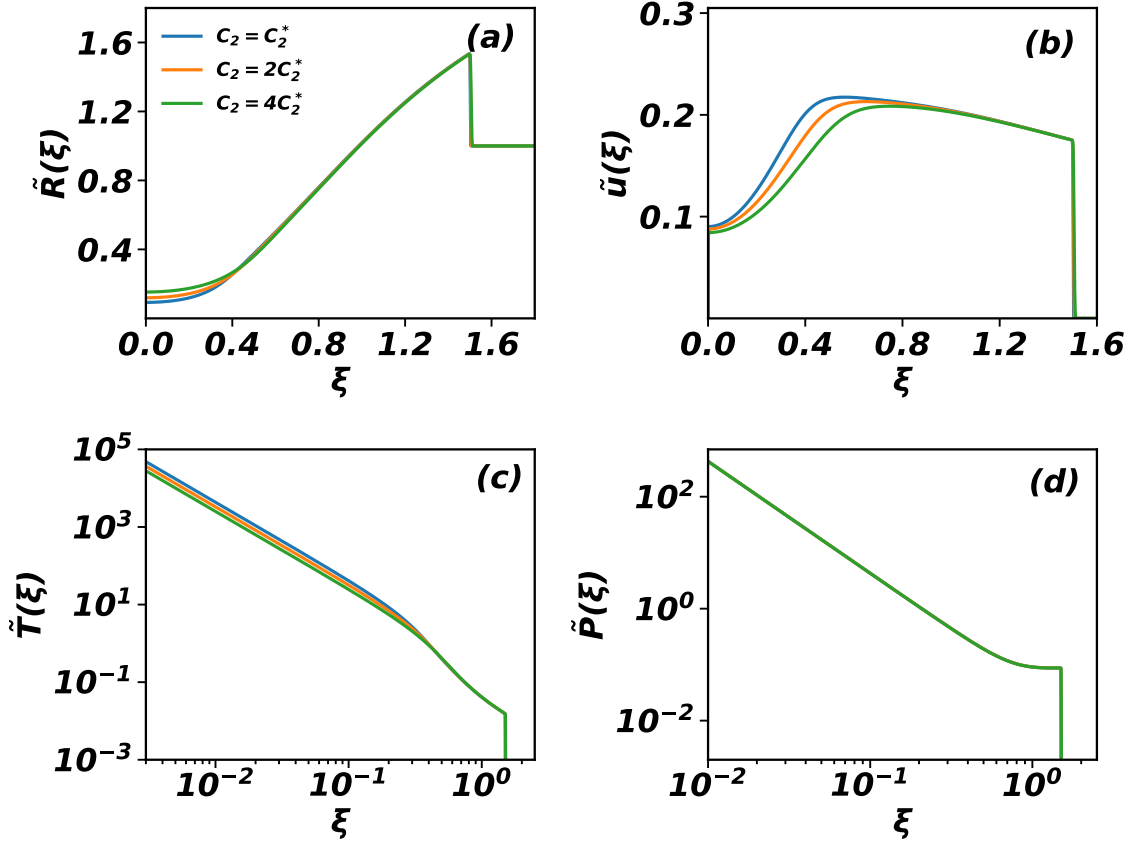


Figure 4.4: Non-dimensionalised (a) density, (b) radial velocity, (c) temperature, and (d) pressure for three different values of the parameter  $C_2$  [see Eq. (4.5)] keeping all other parameters fixed. The data are for  $t = 8000$  and ambient density  $\rho_0 = 0.382$ .

$C_2$ . However, features such as the power-law exponents, density having a finite value at  $r = 0$  remain unchanged with changing  $C_2$ . We also note that pressure does not have any appreciable dependence on  $C_2$  for all  $\xi$ .

Figure 4.5 shows the dependence on the parameter  $C_1$ , related to viscosity, where the results are shown for  $C_1 = C_1^*/4, C_1^*/2, C_1^*$ , keeping all other parameters fixed. We find that changing  $C_1$  does not affect any of the thermodynamic quantities. Thus, features such as the power-law exponents, density having a finite value at  $r = 0$  remain unchanged with changing  $C_1$ .

### 4.3.2 Results in three dimensions

We now show that the Navier-Stokes equations in three dimensions are able to reproduce the simulation results from MD. We solve the continuity Eqs. (4.1)-(4.3)

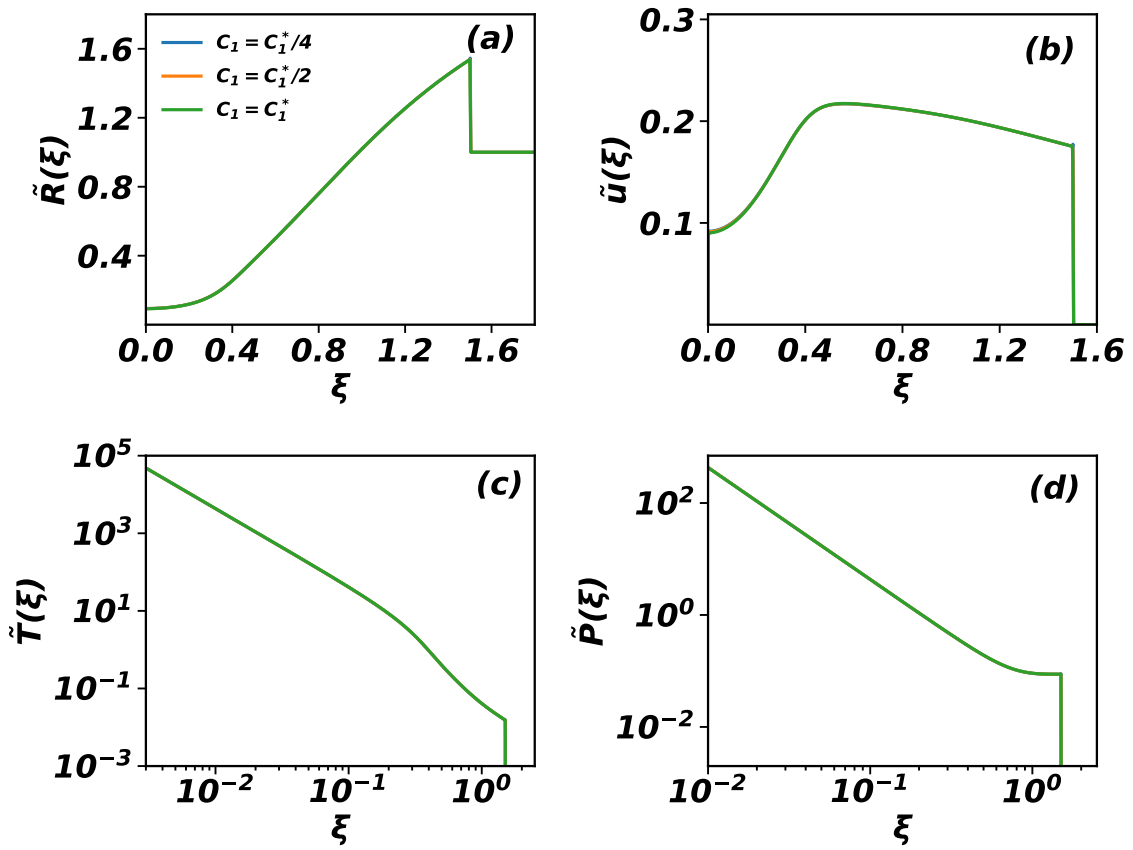


Figure 4.5: Non-dimensionalised (a) density, (b) radial velocity, (c) temperature, and (d) pressure for three different values of the parameter  $C_1$  [see Eq. (4.4)] keeping all other parameters fixed. The data are for  $t = 8000$  and ambient density  $\rho_0 = 0.382$ .

in three dimensions numerically using the values of parameter given in Table 4.2 and virial EOS [see Eq. (4.9)]. We set the coefficient  $C_1$  and  $C_2$  to their kinetic theory values as given in Eqs. (4.6) and (4.7). We solve for both  $\zeta = 0$  and non-zero  $\zeta$  with value as in Eq. (4.8).

In Fig. 4.6, we show the results from DNS for both  $\zeta = 0$  and  $\zeta \neq 0$ . The data for the latter corresponds to the curve whose shock front is to the right. For each of the thermodynamic quantities, the data for four different times collapse onto one curve when they are scaled according to Eqs. (4.14)-(4.17). The power law exponents for temperature and pressure as well as the feature of the scaled density having a finite value for small  $\xi$  are reproduced by the DNS of the Navier-Stokes equations. On the other hand, the TvNS solution, denoted by solid black lines, fail to capture the qualitative features for all the thermodynamic quantities except pressure.

However, unlike in two dimensions, we find that the quantitative results obtained from DNS show a slight discrepancy with the MD simulations results (data are taken from Ref. [16]). When  $\zeta$  is non-zero, we find that the DNS data move closer to the MD results. We have not treated  $\zeta$ ,  $C_1$  and  $C_2$  as free parameters to obtain better fit to the simulation data, as that is not the main focus of the chapter.

## 4.4 Summary and discussion

As summary, in this chapter, we resolved the earlier observed mismatch between the theoretical predictions, based on the Euler equation, for the time evolution of a blast wave and results from hard sphere simulations in two and three dimensions. We compare the results of direct numerical simulations of the Navier-Stokes equations in two and three dimensions with the MD data, and show they match quantitatively. These results are consistent with those found recently for blast waves in one dimension [18, 80]. We conclude that the order in which the scaling limit is taken is

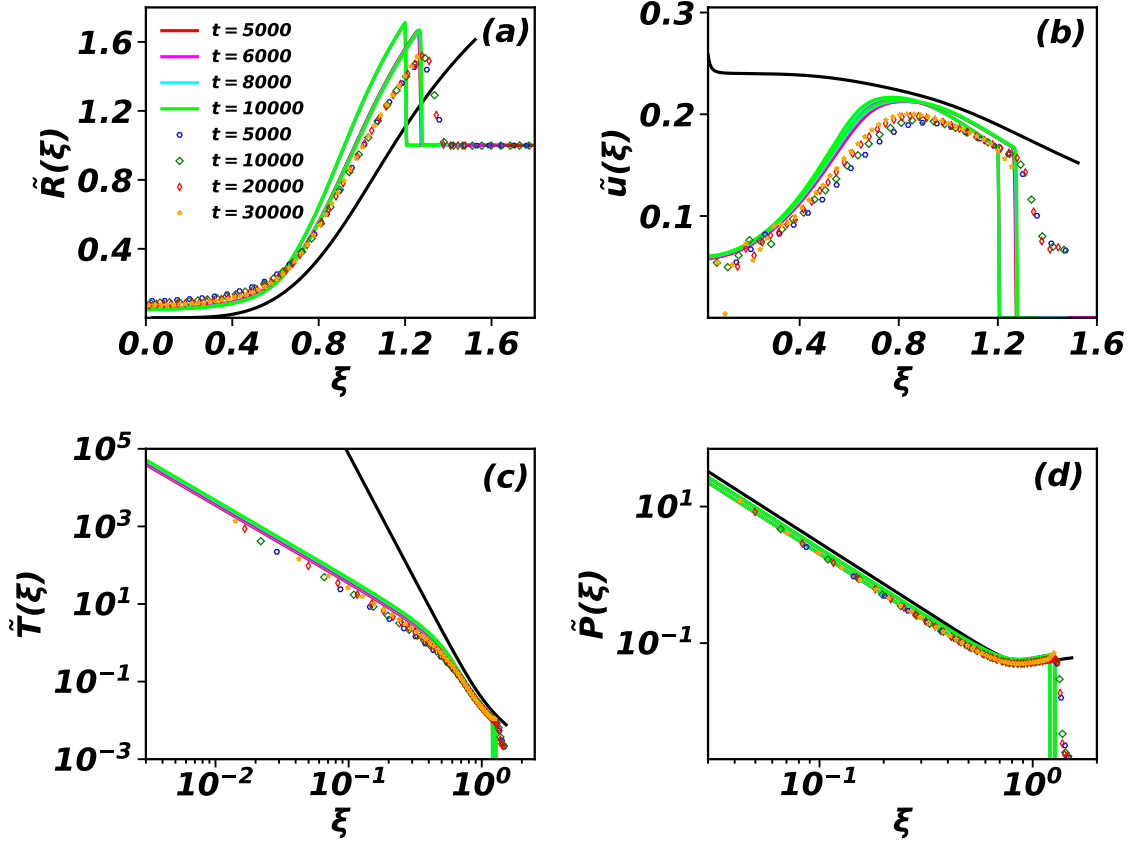


Figure 4.6: The data from MD simulations (taken from Ref. [16]) are compared with the data from DNS of the continuity Eqs. (4.1)-(4.3) in three dimensions. The variation of the non-dimensionalised (a) density (b) radial velocity (c) temperature and (d) pressure with  $\xi$  is shown for four different times. The symbols represent the MD data and solid coloured lines represent the DNS results of the continuity Eqs. (4.1)-(4.3). For the DNS data, the curve where the shock front is to the left corresponds to  $\zeta = 0$  and the curve for which the shock front is to the right corresponds to  $\zeta \neq 0$  and as given in Eq. (4.8). The coefficients  $C_1$  and  $C_2$  are set to their kinetic theory values. The solid black lines represent the TvNS solution with virial EOS. The data are for ambient gas density  $\rho_0 = 0.4$ .

important in the blast problem. In the TvNS solution, the scaling limit is taken first – heat conduction and viscosity terms being irrelevant – before the exact solution is found. However, the correct limit to take is to find the solution with non-zero heat conduction and viscosity terms and then take the scaling limit.

One possible question that immediately arises is whether the TvNS solution will fail to be the correct description in all dimensions or only upto a critical dimension. One way to answer this question would be to solve the TvNS equations numerically in  $d$  dimensions, and check if gradient of temperature is zero at the shock center. If the gradient is zero, one would expect the heat conduction term to be irrelevant and the TvNS solution to be the correct description. This question is a promising area for future research.

To account for steric effects in hard sphere systems, we used the virial EOS to relate pressure to temperature and density. To show that our results are not sensitive to the EOS used, we compare our results with another well-known EOS. A generic EOS has the form [90, 91],

$$p = \rho T Z(\rho), \quad (4.19)$$

where  $Z(\rho)$  is known as compressibility factor of the EOS. There are many proposals for the compressibility factor  $Z(\rho)$  [90–93]. Since the general form of  $Z(\rho)$  is not known, we take the commonly used Henderson relation to solve the continuity Eqs. (4.1)–(4.3). The classic Henderson relation [92] for  $Z(\rho)$  for mono-disperse elastic hard sphere gas in two dimensions is given by

$$Z(\rho) = \frac{128 + \pi^2 \rho^2 D^4}{8(4 - \pi \rho D^2)^2}, \quad (4.20)$$

where  $D$  is the diameter of the hard sphere.

Figure 4.7 compares the results for density, radial velocity, temperature and pressure

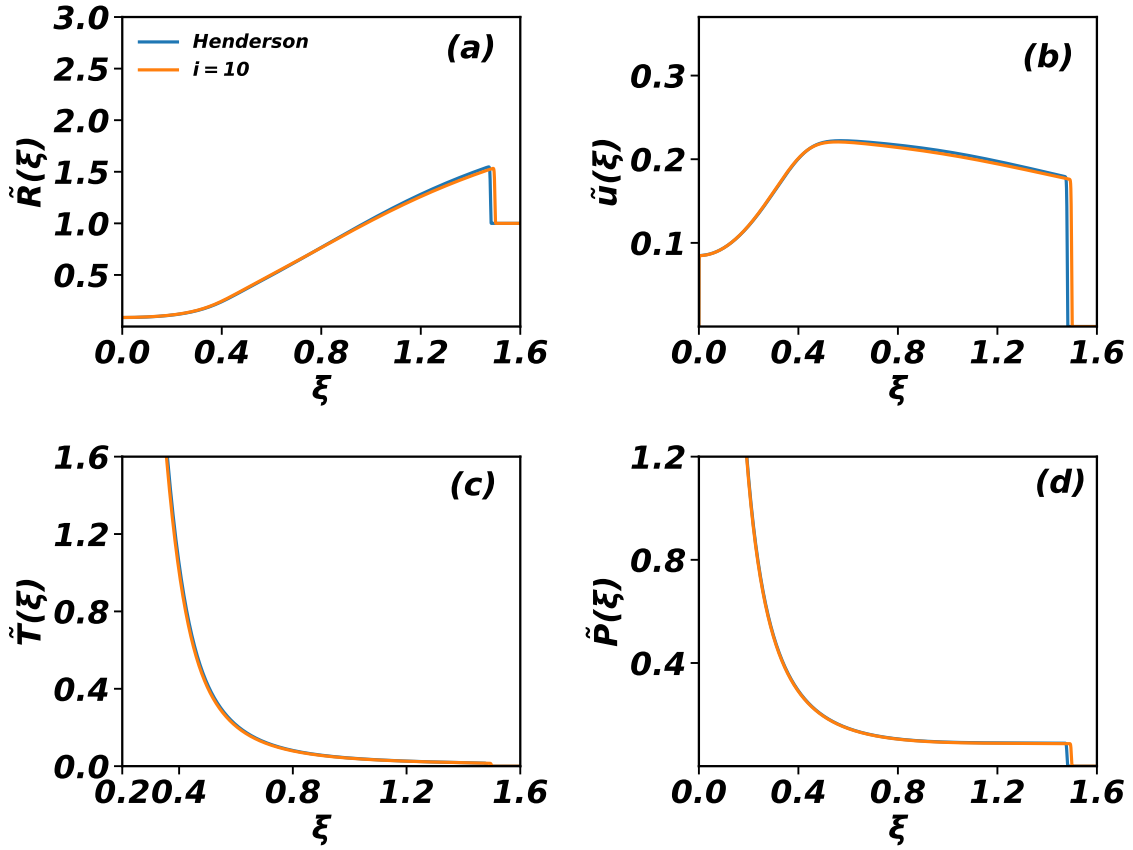


Figure 4.7: The radial variation of non-dimensionalised (a) density, (b) radial velocity, (c) temperature, and (d) pressure for two different EOS: the virial EOS truncated at the 10<sup>th</sup> term [see Eq. (4.9)] and the Henderson EOS [see Eqs. (4.19) and (4.20)]. The data are for time  $t = 8000$ .

for the two EOS. The data for the different EOS cannot be distinguished from each other except for a slight mismatch near the shock front. We conclude that the results presented in this chapter are not dependent on the choice of the EOS as long as the EOS describes the equilibrium hard sphere gas well.

In the TVNS solution, when the scaling limit is taken, heat conduction and viscosity terms are irrelevant. The role of heat conduction is to alter the boundary conditions at the shock center. The solution in the bulk should still be given by the Euler equation. Thus, there should be a small region close to the shock center when a different scaling should be observed as has been seen for one dimension [18, 80]. Likewise, there should be a region near the shock front where the scaling should be different [28]. Identifying these different scaling would be a promising area for

future study.

The TvNS theory has been extended to study problems where there is a continuous input of energy at the shock center [13]. It would be interesting to compare the theoretical predictions for this problem with MD simulations and check whether it is important to keep heat conduction and viscosity terms.



# 5

## Shock propagation following an intense explosion in an inhomogeneous gas: core scaling and hydrodynamics

### Related Publication :

This chapter is based on the following publication [94]:

Shock propagation following an intense explosion in an inhomogeneous gas: core scaling and hydrodynamics,

**Amit Kumar** and R. Rajesh, *Journal of Statistical Physics*, 192(2):17, 2025.



### 5.1 Introduction

The behaviour of shock propagation has primarily been studied in systems with a homogeneous ambient mass density distribution. In general, the ambient medium

could have any initial density distributions. The scaling solutions of Euler equation for shock propagation are possible for homogeneous as well as for inhomogeneous mediums. The evolution of thermodynamic quantities has been studied both for a homogeneous gas in which initial density of the gas is uniform, as well as an inhomogeneous gas where the initial density,  $\rho(r)$ , at distance  $r$  from the explosion varies as  $\rho(r) = \rho_0 r^{-\beta}$ .

In the scaling regime, from dimensional analysis, it is straightforward to obtain that the radius of the shock front,  $R(t)$ , grows as  $R(t) \sim (E_0/\rho_0)^{\alpha/2} t^\alpha$  with  $\alpha = 2/(2+d-\beta)$  in  $d$ -dimensions, where  $E_0$  is the energy input [4–7, 11].

The spatio-temporal evolution of the thermodynamic quantities are studied using the continuity equations of mass, momentum, and the energy, corresponding to the Navier-Stokes equations. However, in the scaling limit  $r \rightarrow \infty$ ,  $t \rightarrow \infty$  keeping  $rt^{-\alpha}$  finite, the heat conduction and viscosity terms are negligible, leading to the Euler equation. If the gas is assumed to an ideal gas, then an exact solution for density, velocity and temperature, can be found both for the homogeneous case [4–7, 11] as well as the inhomogeneous case [11].

In this chapter, we generalise these results to the case of an explosion in an inhomogeneous gas, where the initial density varies as a power law  $\rho(r) = \rho_0 r^{-\beta}$ . We generalise the exact solution of the Euler equation to  $d$ -dimensions. By examining the asymptotic behaviour near the shock center, we identify a critical  $\beta$  for which we conjecture that Euler equation should give a complete description of the problem both at the shock center as well as the shock front. For other  $\beta$ , we show that there is a crossover behaviour near the shock center. We generalise the results of Ref. [18, 80, 95] for  $\beta = 0$  to arbitrary  $\beta$  to derive a crossover length scale as well as a core scaling which describes the data near the shock center. These results are verified using event driven molecular dynamics simulations in one dimension and numerical integration of the Navier-Stokes equations in one dimension.

---

The remainder of the chapter is organised as follows. In Sec. 5.3, we generalise the exact solution of Euler equation to  $d$ -dimensions, and find the asymptotic behaviour of the thermodynamic quantities near the shock center. Based on these results, we derive a critical  $\beta_c$  for which the solution satisfies  $\nabla T = 0$  at the center. In Sec. 5.4 we define the model for the EDMD simulations, and show that the simulation data differs from the exact solution near the shock center for the different thermodynamic quantities. In Sec. 5.5, after describing the details of the numerical solution of the Navier-Stokes equations, we show that including dissipation terms are able to reproduce the EDMD data for different  $\beta$ . The crossover near the shock center is studied in Sec. 5.6 by identifying a crossover length scale and the resultant scaling of the different thermodynamic functions. These are verified in EDMD simulations. In Sec. 5.7, we show numerically that the data for critical  $\beta$  are completely described by the Euler equation without any dissipation terms. We conclude with a summary and discussion in Sec. 5.8. The content of this chapter is published in Ref. [94].

## 5.2 Problem definition

At initial time  $t = 0$ , we consider a gas whose density is inhomogeneous and varies from the center as

$$\rho(\vec{r}, t = 0) = \frac{\rho_0}{r^\beta}, \quad (5.1)$$

where  $\beta$  is the exponent characterising the power law variation. To ensure that the total mass in a bounded region is finite, we require  $\beta < d$ , where  $d$  is the dimension [11].

Energy  $E_0$  is isotropically input at the center at time  $t = 0$ . The “explosion” results in the formation of a spherically symmetric shock that propagates outwards in time with a shock front at  $R(t)$  separating the disturbed gas from the ambient gas. The parameters in the problem are  $E_0$ ,  $\rho_0$ , and  $t$  with dimensions  $[E] = ML^2T^{-2}$ ,  $[\rho_0] =$

$ML^{-d+\beta}$  and  $[t] = T$ .  $R(t)$  can be uniquely written in terms of these quantities by dimensional analysis, and we obtain [1, 11, 73]:

$$R(t) \propto \left( \frac{E_0}{\rho_0} \right)^{\alpha/2} t^\alpha, \quad (5.2)$$

where

$$\alpha = \frac{2}{2+d-\beta}. \quad (5.3)$$

We study the self-similar evolution of the shock using different methods: within Euler equation in  $d$ -dimensions, EDMD simulations of point sized binary gas in one dimension and Navier-Stokes equations in one dimension. We will be primarily interested in the following thermodynamic quantities: temperature  $T(r, t)$ , radial velocity  $u(r, t)$ , and density  $\rho(r, t)$ . In particular, we will analyse the scaling of these quantities near the shock front as well as the core region near the center of the shock.

## 5.3 Exact solution of the Euler equation in $d$ -dimensions

### 5.3.1 Euler equation

In this section, we generalise the known exact solution of the Euler equation for an explosion in an ideal gas with a density gradient. This will also allow us to derive the behaviour of the thermodynamic quantities near the shock center, which in turn will allow us to determine the crossover exponents for  $r \rightarrow 0$  in the presence of dissipative terms.

The microscopic description of the gas, at position  $\vec{r}$ , and at time  $t$ , is given by the local fields of the density  $\rho(\vec{r}, t)$ , velocity  $\vec{u}(\vec{r}, t)$ , temperature  $T(\vec{r}, t)$ , and the pressure  $p(\vec{r}, t)$ . These thermodynamic quantities evolve in time based on the continuity

equations of the mass, momentum, and the energy. In the scaling limit  $r, t \rightarrow \infty$ , keeping  $rt^{-\alpha}$  constant [see Eq. (5.2)], the contributions of heat conduction and viscosity terms become negligible. The continuity equations, after ignoring these terms, result in the Euler equation. Using spherical symmetry, the Euler equation in radial coordinates in  $d$ -dimensions is given by [1–3, 11, 13],

$$\partial_t \rho + \partial_r(\rho u) + \frac{(d-1)\rho u}{r} = 0, \quad (5.4)$$

$$\partial_t u + u \partial_r u + \frac{1}{\rho} \partial_r p = 0, \quad (5.5)$$

$$\partial_t \left( \frac{p}{\rho^\gamma} \right) + u \partial_r \left( \frac{p}{\rho^\gamma} \right) = 0, \quad (5.6)$$

where  $\gamma = 1 + 2/d$  is the adiabatic index of a mono-atomic gas. If local thermal equilibrium of the gas is considered, then the local pressure of the gas can be obtained from the equation of the state of the gas,

$$p = k_B \rho T, \quad (5.7)$$

where  $k_B$ , the Boltzmann constant, is set equal to one in the remainder of the chapter.

We introduce non-dimensional distance  $\xi$ , density  $\tilde{R}$ , velocity  $\tilde{u}$ , and temperature  $\tilde{T}$  [11, 13]:

$$\rho(r, t) = \rho_0 r^{-\beta} \tilde{R}(\xi), \quad (5.8)$$

$$u(r, t) = \frac{r}{t} \tilde{u}(\xi), \quad (5.9)$$

$$T(r, t) = \frac{r^2}{t^2} \tilde{T}(\xi), \quad (5.10)$$

$$\xi = r \left( \frac{E_0}{\rho_0} \right)^{-\alpha/2} t^{-\alpha}. \quad (5.11)$$

The position of the shock front will be denoted by  $\xi_f$ . The Euler equation (5.4)–(5.6), on non-dimensionalising reduce to ordinary differential equations:

$$(\tilde{u} - \alpha) \frac{d \log \tilde{R}}{d \log \xi} + \frac{d \tilde{u}}{d \log \xi} + (d - \beta) \tilde{u} = 0, \quad (5.12)$$


---

$$(\tilde{u} - \alpha) \frac{d\tilde{u}}{d \log \xi} + \frac{d\tilde{T}}{d \log \xi} + \tilde{T} \frac{d \log \tilde{R}}{d \log \xi} + (2 - \beta) \tilde{T} + \tilde{u}^2 - \tilde{u} = 0, \quad (5.13)$$

$$(\tilde{u} - \alpha) \frac{d}{d \log \xi} \log \left( \frac{\tilde{T}}{\tilde{R}^{\gamma-1}} \right) + [2 + \beta(\gamma - 1)] \tilde{u} - 2 = 0. \quad (5.14)$$

Across the shock front, the thermodynamic quantities are discontinuous and obey the Rankine-Hugoniot boundary conditions, which are [1, 3, 11],

$$\rho_1 = \left( \frac{\gamma + 1}{\gamma - 1} \right) \rho_0, \quad (5.15)$$

$$u_1 = \frac{2}{\gamma + 1} U, \quad (5.16)$$

$$p_1 = \rho_0 U u_1, \quad (5.17)$$

where the subscript 1 signifies values just behind the shock front, and  $U = \dot{R}$  is the speed of the shock front. In terms of the dimensionless quantities, the Rankine-Hugoniot boundary conditions (5.15)–(5.17) reduce to

$$\tilde{R}(\xi_f) = \frac{\gamma + 1}{\gamma - 1}, \quad (5.18)$$

$$\tilde{u}(\xi_f) = \frac{2\alpha}{\gamma + 1}, \quad (5.19)$$

$$\tilde{T}(\xi_f) = \frac{2\alpha^2(\gamma - 1)}{(\gamma + 1)^2}. \quad (5.20)$$

We need one more equation for determining  $\xi_f$ . This is provided by the energy conservation, ie, the total energy is  $E_0$ . This constraint reduces to

$$S_d \int_0^{\xi_f} \left( \frac{1}{2} \tilde{R} \tilde{u}^2 + \frac{\tilde{R} \tilde{T}}{\gamma - 1} \right) \xi^{d+1-\beta} d\xi = 1, \quad (5.21)$$

where  $S_d = \frac{2\pi^{d/2}}{\Gamma(d/2)}$  is the surface area of  $d$ -dimensional sphere of unit radius.  $\Gamma$  is the Gamma function.

It has been shown [1, 11] that the solution curve of Euler equation (5.12)–(5.14) in the  $\tilde{T}$ - $\tilde{u}$  plane, that passes through the Rankine-Hugoniot boundary conditions (5.15–

5.17), should satisfy

$$\tilde{T} = \frac{\tilde{u}^2(\alpha - \tilde{u})(\gamma - 1)}{2(\gamma\tilde{u} - \alpha)}, \quad (5.22)$$

### 5.3.2 The exact solution

The analytical solution of Eqs. (5.12)–(5.13) with the help of integral curve (5.22) using Rankine-Hugoniot boundary Eqs. (5.18)–(5.20) is given by

$$\frac{\xi(\tilde{u})}{\xi_f} = \alpha^\alpha 2^{\frac{a_2}{2a_1}} \frac{(g_3(\tilde{u}))^{\frac{\gamma-1}{a_0}}}{((\gamma+1)\tilde{u})^\alpha} \left( \frac{g_1(\tilde{u})}{\alpha b_1} \right)^{\frac{a_4}{2a_1}} e^{\frac{a_3 \left( \tanh^{-1} \left( \frac{g_2(\tilde{u})}{\sqrt{A_1}} \right) - \tanh^{-1} \left( \frac{g_2(\tilde{u}(\xi_f))}{\sqrt{A_1}} \right) \right)}{a_1 \sqrt{A_1}}}}, \quad (5.23)$$

$$\tilde{R}(\tilde{u}) = \alpha \frac{(g_3(\tilde{u}))^{\frac{d-\beta}{a_0}}}{\alpha - \tilde{u}} \left( \frac{g_1(\tilde{u})}{2\alpha b_1} \right)^{\frac{b_2}{2a_1}} e^{\frac{b_3 \left( \tanh^{-1} \left( \frac{g_2(\tilde{u})}{\sqrt{A_1}} \right) - \tanh^{-1} \left( \frac{g_2(\tilde{u}(\xi_f))}{\sqrt{A_1}} \right) \right)}{a_1 \sqrt{A_1}}}}, \quad (5.24)$$

where

$$A_1 = \alpha^2(\beta(\gamma - 1) - 2\gamma + 4)^2 + 4\gamma^2 + 4\alpha((\beta - 2)\gamma^2 - (\beta - 4)\gamma - 2(\gamma - 1)d - 4),$$

$$a_0 = d - (\beta - 2)\gamma - 2,$$

$$a_1 = (d(\gamma - 1) + 2)(d - (\beta - 2)\gamma - 2),$$

$$a_2 = \alpha(\gamma - 1)d^2 - \left( \alpha((\beta - 2)\gamma^2 - (\beta - 4)\gamma - 4) - (\gamma - 1)\gamma - 2 \right) d \\ - (\beta - 2)(\gamma + 1)\gamma - 2\alpha((\beta - 2)\gamma + 2) - 4,$$

$$a_3 = a_1((\beta - 2)\gamma - \beta + 4)\alpha^2 + \left[ 2(\gamma^2 - 5\gamma + 4)d^2 - \beta(\gamma^3 - 8\gamma^2 + 5\gamma + 2)d \right. \\ \left. + 2(\gamma^3 - 9\gamma^2 + 16\gamma - 12)d + \beta^2(\gamma - \gamma^3) + \beta(4\gamma^3 - 6\gamma^2 + 6\gamma + 4) \right. \\ \left. - 4(\gamma^3 - 3\gamma^2 + 6\gamma - 4) \right] \alpha - 2\gamma^2(\gamma\beta + \beta + d(\gamma - 3) - 2\gamma + 2),$$

$$a_4 = \alpha(\gamma - 1)d^2 - \left( \alpha((\beta - 2)\gamma^2 - (\beta - 4)\gamma - 4) + (\gamma - 1)\gamma + 2 \right) d \\ + (\beta - 2)(\gamma + 1)\gamma - 2\alpha((\beta - 2)\gamma + 2) + 4,$$

$$b_1 = -\frac{(\gamma - 1)(\alpha((\beta - 2)\gamma + \beta - 2d) + \gamma + 1)}{(\gamma + 1)^2},$$

$$b_2 = \beta((\beta - 2)\gamma^2 + \beta\gamma + 4) + 2d^2 - d((\beta - 2)\gamma^2 + (\gamma + 2)\beta + 4),$$

Table 5.1: The values of  $\beta$  in different dimensions for which the constants  $a_0$  or  $b_1$  equals zero, making the analytical solution in Eqs. (5.23)–(5.24) singular.

	$\beta(d=1)$	$\beta(d=2)$	$\beta(d=3)$
$a_0$	5/3	2	13/5
$b_1$	1	4/3	2

$$b_3 = (d - \beta)((\beta - 2)\gamma + \beta - 2d) \left( \alpha \left( (\beta - 2)\gamma^2 - (\beta - 4)\gamma - 2(\gamma - 1)d - 4 \right) + 2\gamma^2 \right),$$

$$g_1(\tilde{u}) = \tilde{u}^2((\gamma - 1)d + 2) - \tilde{u}(\alpha((\beta - 2)\gamma - \beta + 4) + 2\gamma) + 2\alpha,$$

$$g_2(\tilde{u}) = 2\tilde{u}((\gamma - 1)d + 2) - \alpha((\beta - 2)\gamma - \beta + 4) - 2\gamma,$$

$$g_3(\tilde{u}) = \frac{(\gamma + 1)(\gamma\tilde{u} - \alpha)}{\alpha(\gamma - 1)}.$$

The above constants depend on  $\beta$ . The constants  $a_0$  and  $b_1$  become zero for certain values of  $\beta$  resulting in the solution becoming singular. These values of  $\beta$  are tabulated in Table 5.1. For these special cases, the exact solution has been described in  $d = 3$  [11]. In this chapter, we will consider only the generic non-singular case.

### 5.3.3 Asymptotic behaviour for $\xi \rightarrow 0$

According to the solution Eq. (5.23), when  $\xi \rightarrow 0$  then  $\tilde{u} \rightarrow \frac{\alpha}{\gamma}$ , and the range being  $\tilde{u} \in [\alpha/\gamma, 2\alpha/(\gamma + 1)]$ . When  $\xi \rightarrow 0$ , the exact solutions of  $\tilde{u}$ ,  $\tilde{R}$ , and  $\tilde{T}$  lead to the following asymptotic behaviour:

$$\tilde{u} - \frac{\alpha}{\gamma} \rightarrow \xi^{\frac{d-2+(2-\beta)\gamma}{\gamma-1}}, \quad (5.25)$$

$$\tilde{R} \rightarrow \xi^{\frac{d-\beta}{\gamma-1}}, \quad \xi \rightarrow 0, \quad (5.26)$$

$$\tilde{T} \rightarrow \xi^{-\frac{d-2+(2-\beta)\gamma}{\gamma-1}}. \quad (5.27)$$

The behavior near the shock center is dependent on the inhomogeneity parameter  $\beta$ , unlike on the driving parameter in driven shock [96]. For  $\beta = 0$  all of these exponents become equal to those for single impact [16, 17, 95].

It is convenient to define a different non-dimensional velocity  $\tilde{V}$  instead of  $\tilde{u}$  to avoid



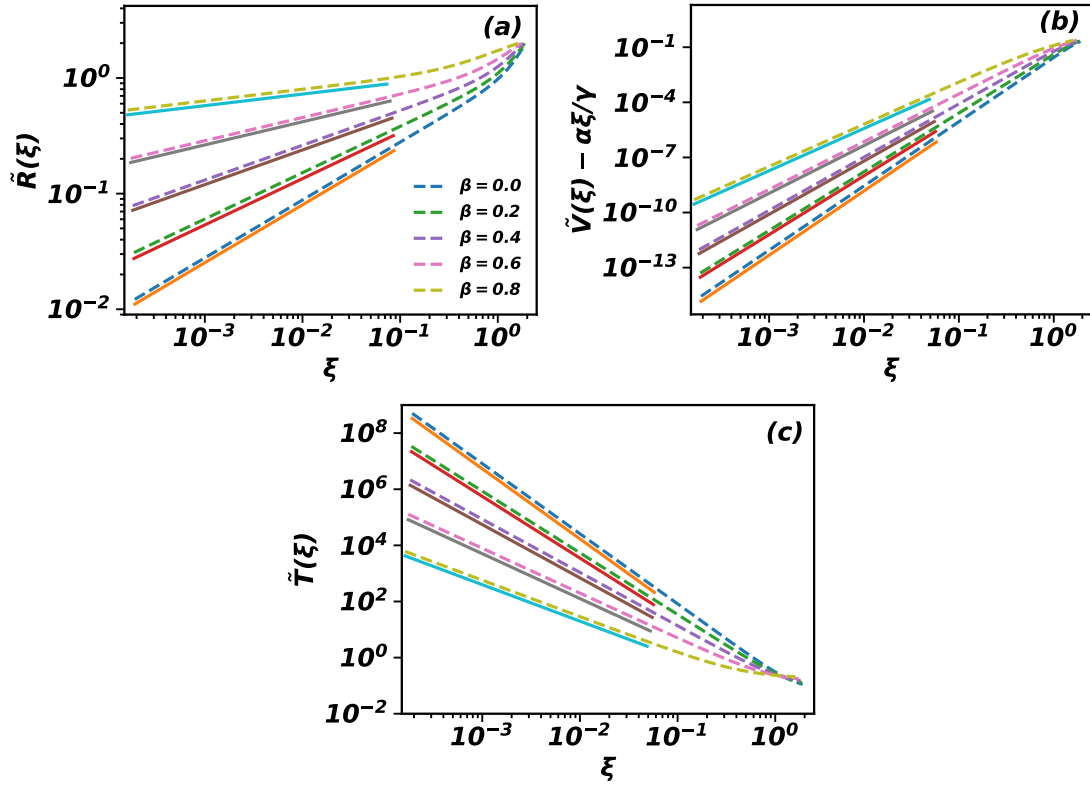


Figure 5.1: (a) density  $\tilde{R}$ , (b) velocity  $\tilde{V}$ , and (c) temperature  $\tilde{T}$  obtained from the exact solution [see Eqs. (5.22)–(5.24)] of the Euler equation for five different values of  $\beta = 0.0, 0.2, 0.4, 0.6, 0.8$ . The coloured solid lines represent the fitting of power law behaviour near the shock center (see Eqs. (5.26–5.27) and Eq. (5.29)) for various  $\beta$ . All the curves are for  $d = 1$ .

numerical difficulties in measuring  $\tilde{u}$  near the center. We define  $\tilde{V}$  as

$$\tilde{V} = \xi \tilde{u}. \quad (5.28)$$

Near the shock center,  $\tilde{V}$  follows the following asymptotic behaviour,

$$\tilde{V} - \frac{\alpha\xi}{\gamma} \rightarrow \xi^{\frac{d-3+(3-\beta)\gamma}{\gamma-1}} \quad (5.29)$$

To confirm the correctness of the asymptotic behaviour near the shock center, we compare the power law behaviour with the exact solution in Fig. 5.1 for five different values of  $\beta$ . The asymptotic behavior compare well with the exact result for  $\tilde{R}$  [Fig. 5.1(a)],  $\tilde{V}$  [Fig. 5.1(b)], and  $\tilde{T}$  [Fig. 5.1(c)].

### 5.3.4 Critical $\beta$

In the exact solution of the Euler equation, the exponent characterising the power-law behaviour of the temperature and density for  $\xi \rightarrow 0$  depends on  $\beta$  [see Eq. (5.26) and Eq. (5.27)] as

$$T \sim r^{\frac{\beta\gamma-d}{\gamma-1}} t^{\frac{-\alpha(\beta-2d+d\gamma)}{\gamma-1}}, \quad r \rightarrow 0 \quad (5.30)$$

$$\rho \sim r^{\frac{-\beta\gamma+d}{\gamma-1}} t^{\frac{-\alpha(d-\beta)}{\gamma-1}}, \quad r \rightarrow 0. \quad (5.31)$$

Temperature diverges for small  $r$  for  $\beta < d/\gamma$  while  $\nabla T$  diverges for  $\beta < (d+\gamma-1)/\gamma$ . The divergence of  $\nabla T$  is not consistent with the boundary condition when heat conduction is present, namely  $\nabla T = 0$ . For  $\beta = \beta_c = d/\gamma$ , and  $\beta > (d+\gamma-1)/\gamma$ , we find that  $\nabla T = 0$ . We identify the critical value of  $\beta$ , denoted as  $\beta_c$ , for which the solution to the Euler equation satisfies  $\nabla T = 0$  with  $T \rightarrow \dot{R}(t)^2$ , and to achieve this the condition  $\tilde{T} \rightarrow \xi^{-2}$ , or equivalently  $T \sim r^0$ , must hold. This condition is seen for the temperature in all the simulations. We also check that for  $\beta = \beta_c$ , the heat conduction term is always sub-dominant (see discussion after Eq. (5.49)). At this critical  $\beta_c$ , the Euler equation is expected to provide a complete description of the problem. From Eq. (5.30), we deduce that the critical value of  $\beta_c$  in  $d$  dimensions is given by:

$$\beta_c = \frac{d}{\gamma}. \quad (5.32)$$

This conjecture will be validated through simulations in subsequent sections.

It is possible that for  $\beta > (d+\gamma-1)/\gamma = 1(1d), 3/2(2d)$ , heat conduction is still important. While this is not possible in one dimension, there is a possibility in two dimensions since  $\beta$  can take values upto 2.

## 5.4 Molecular Dynamics Simulations

In this section, we verify the asymptotic behaviours given by Eqs. (5.26–5.27) and Eq. (5.29) using EDMD simulations of hard point particles in one dimension. In

collisions, particles with the same mass simply exchange their velocities, and in one dimension making the system integrable. In the following, we consider bi-dispersed hard point particles, where adjacent particles have different masses  $m_1$  and  $m_2$ . Alternating particles with different masses breaks the integrability of the system [97–99].

### 5.4.1 Model

Consider a system of  $N$  point particles labeled  $i = 1, 2, 3, \dots, N$  sorted according to their positions  $x_i$ . Let their velocities be denoted by  $u_i$ . All the particles with odd  $i$  have mass  $m_1$  and even  $i$  have mass  $m_2$ . Particles do ballistic motion until they undergo energy and momentum conserving elastic collisions. Since the particles are on a line, the particle  $i$  can only collide with the particles  $i - 1$  or  $i + 1$ , which conserves the ordering of the particles. If  $u_i$ , and  $u_j$  are the pre-collision velocities of the particles  $i$ , and  $j$  then their post-collision velocities  $u'_i$ , and  $u'_j$ , respectively, are given by

$$u'_i = \frac{m_i u_i + m_j u_j + m_j (u_j - u_i)}{m_i + m_j}, \quad (5.33)$$

$$u'_j = \frac{m_j u_j + m_i u_i + m_i (u_i - u_j)}{m_i + m_j}. \quad (5.34)$$

We consider the region  $0 \leq x \leq L$  centered about with  $x = L/2$ . To implement the initial density as given in Eq. (5.1), we divide the region in equally spaced bins with bin-size  $\Delta r$ . The number of particles,  $N_r$ , in a bin at distance  $r$  from  $L/2$  is given by

$$N_r = \left\lceil \frac{N}{2(L/2)^{1-\beta}} \left[ (r + \Delta r)^{1-\beta} - r^{1-\beta} \right] \right\rceil, \quad (5.35)$$

where  $\lceil \dots \rceil$  is the least integer function. This gives  $\rho_0 = \frac{N}{4} \frac{(1-\beta)(m_1+m_2)}{(L/2)^{(1-\beta)}}$ . The  $N_r$  particles are distributed at random in the respective bins in  $[0, L/2]$ . Symmetry about  $L/2$  is ensured by filling the bins in  $[L/2, L]$  based on the positions of particles in bins in  $[0, L/2]$ .

All the particles are initially at rest. An initial energy  $E_0$  is input by giving to  $N_c$  number of particles around the center a non-zero velocity that depends on their position. The first  $N_c/2$  particles are given velocities as

$$u_{N/2+1+i} = u_0 e^{\frac{-(x_{N/2+1+i}-L/2)^2}{2\sigma^2}}, \quad (5.36)$$

and the remaining  $N_c/2$  particles have velocity  $u_{(N-N_c)/2+i} = -u_{(N+N_c)/2+1-i}$ , where  $i \in [0, N_c/2]$ , and  $u_0, \sigma$  are the positive constants. The velocities are rescaled to ensure that the system has total energy  $E_0$ , and zero linear momentum.

In the EDMD simulations for different  $\beta$ , we take  $N = 50000$ ,  $L = 10000$ , and  $E_0 = 24$ ,  $N_c = 32$ ,  $m_1 = 1$ ,  $m_2 = 2$ . The simulation time is chosen such that the shock front does not reach the boundaries.

### 5.4.2 Behaviour of thermodynamic quantities

To benchmark the EDMD simulations, we reproduce the scaling of the shock front,  $R(t)$  with time, as given in Eq. (5.2). Our simulations reproduce the scaling exponent for different  $\beta$  accurately as can be seen from Fig. 5.2.

To measure  $\rho(x, t)$ ,  $u(x, t)$ ,  $T(x, t)$ , we divide the system size into bins with bin size  $\Delta'$ , and measure these quantities in a bin at spatial position  $x \in [0, L]$  as

$$\rho(x, t) = \left\langle \frac{\sum m_i \delta(x_i, x)}{\Delta'} \right\rangle, \quad (5.37)$$

$$u(x, t) = \left\langle \frac{\sum m_i u_i \delta(x_i, x)}{\sum m_i \delta(x_i, x)} \right\rangle, \quad (5.38)$$

$$T(x, t) = \left\langle \frac{\sum m_i u_i^2 \delta(x_i, x)}{\sum m_i \delta(x_i, x)} \right\rangle - \left( \left\langle \frac{\sum m_i u_i \delta(x_i, x)}{\sum m_i \delta(x_i, x)} \right\rangle \right)^2, \quad (5.39)$$

where  $\langle \dots \rangle$  denotes averaging over different initial configuration, and  $\delta$  is a step

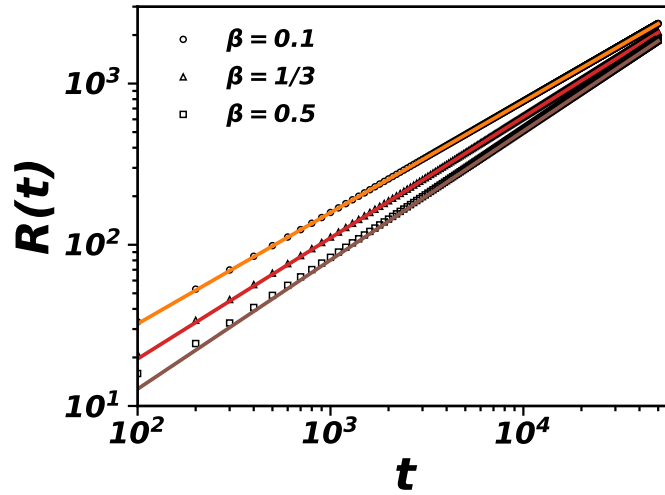


Figure 5.2: The power law variation of the radius of shock front,  $R(t)$ , with time  $t$ . Symbols represent the EDMD data for three different values of  $\beta = 0.1, 1/3, 0.5$ . The solid lines represent the fitting of power law behaviour  $R(t) \sim t^{\frac{2}{3-\beta}}$ .

function defined as

$$\delta(x_i, x) = \begin{cases} 1 & |x - x_i| \leq \Delta'/2 \\ 0 & |x - x_i| > \Delta'/2 \end{cases} \quad (5.40)$$

We average over  $10^3$  different initial configurations for each  $\beta$ . We present data for mostly  $\beta = 0.1, 0.5$ . We note that in one dimension  $\beta_c = 1/3$ , and these two values are chosen as representative values above and below  $\beta_c$ .

The variation of  $\rho$ ,  $u$ ,  $T$  with spatial position  $x$  at four different times is shown in Fig. 5.3 for  $\beta = 0.1, 0.5$ . The density  $\rho(x)$  increases monotonically for  $\beta = 0.1$ , while for  $\beta = 0.5$ , there is a sharp increase in density at the shock center. Temperature also shows different behaviour near the shock center. For  $\beta = 0.1$ , temperature diverges near the shock center before being rounded off, while it is a minimum for  $\beta = 0.5$  at the shock center. The qualitative behaviour of velocity  $u(x)$  remains unchanged for all  $\beta$ .

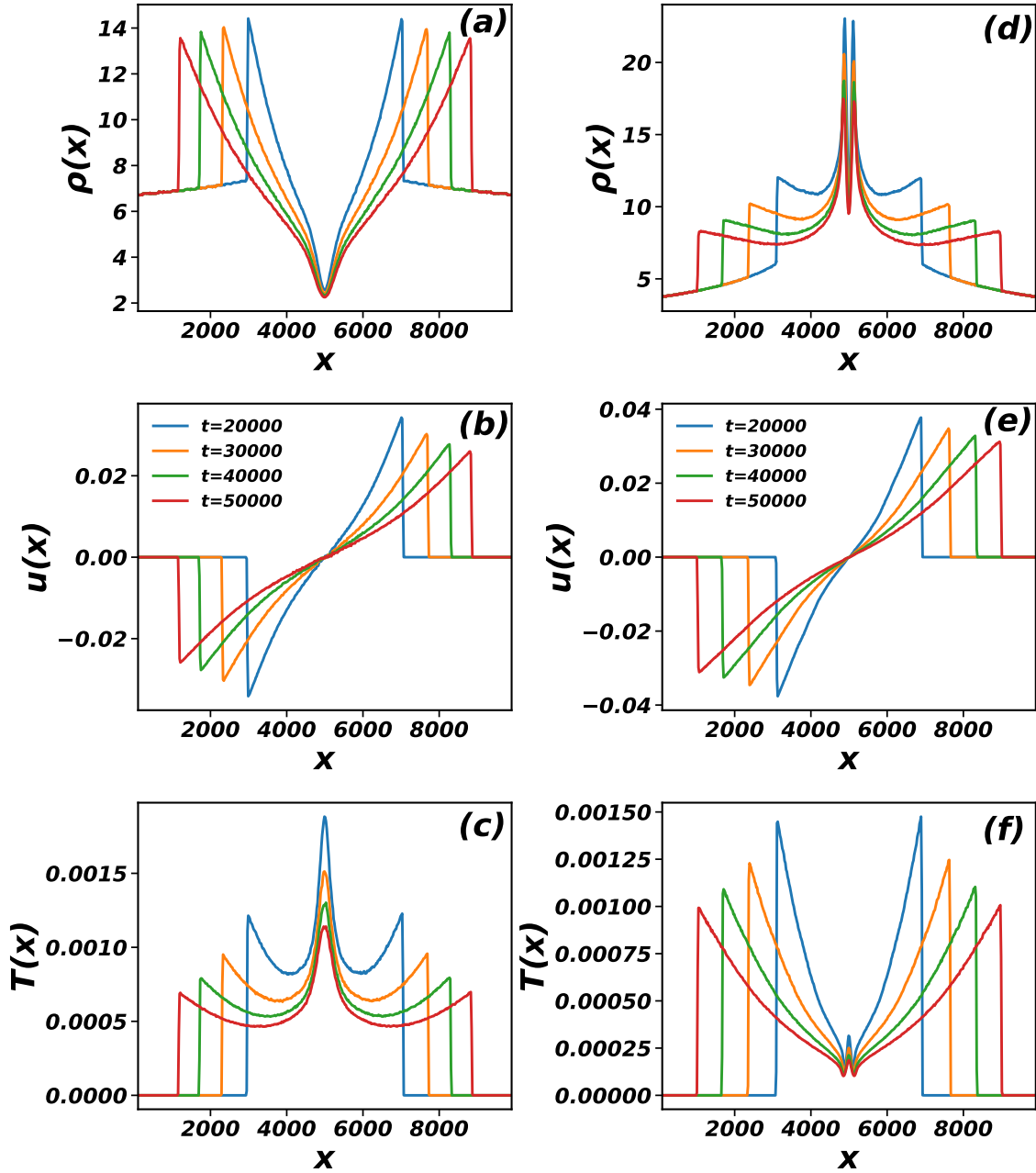


Figure 5.3: The variation of (a) density  $\rho(x,t)$ , (b) velocity  $u(x,t)$ , and (c) temperature  $T(x,t)$  with spatial position  $x$  at four different times  $t = 20000, 30000, 40000, 50000$ . Figs. (a)–(c) are for  $\beta = 0.1$ , and Figs. (d)–(f) are for  $\beta = 0.5$ .

### 5.4.3 Comparison between the exact solution of the Euler equation and simulations

In Fig. 5.4, we compare the non-dimensionalised thermodynamic quantities  $\tilde{R}(\xi)$ ,  $\tilde{V}(\xi)$ , and  $\tilde{T}(\xi)$  obtained from the EDMD simulations and the exact solution of Euler equation for two different values of  $\beta = 0.1, 0.5$ . First, we note that the data for the different times, away from the shock center, collapse onto one curve, validating the correctness of the scaling Eqs.(5.8)–(5.11) for both values of  $\beta$ . The data away from the shock center match perfectly with the exact solution of the Euler equation.

The data near the shock center do not seem to collapse (see the inset plots in Fig. 5.4), which indicates that the system follows a different scaling near center. Near the shock center, the EDMD results show that the density  $\tilde{R}(\xi)$  increases as  $\tilde{R} \sim \xi^\beta$ . Also, independent of  $\beta$ , temperature varies as  $\tilde{T} \sim \xi^{-2}$ , or equivalently  $\nabla T = 0$ . These power law exponents differ from the exponents given by the exact solution,  $\tilde{R} \sim \xi^{(1-\beta)/2}$ ,  $\tilde{T} \sim \xi^{-(5-3\beta)/2}$ , showing the discrepancy between the exact solution and the simulation results.

## 5.5 Navier-Stokes Equations

In this section, we describe the numerical solution of Navier-Stokes equations, and its comparison with the EDMD results and the exact solution.

### 5.5.1 Numerical details

Taking into account the dissipation terms in the Euler equation, we obtain the Navier-Stokes equations. The different continuity equations now reduce to [1, 84],

$$\partial_t \rho + \partial_x(\rho u) = 0, \quad (5.41)$$

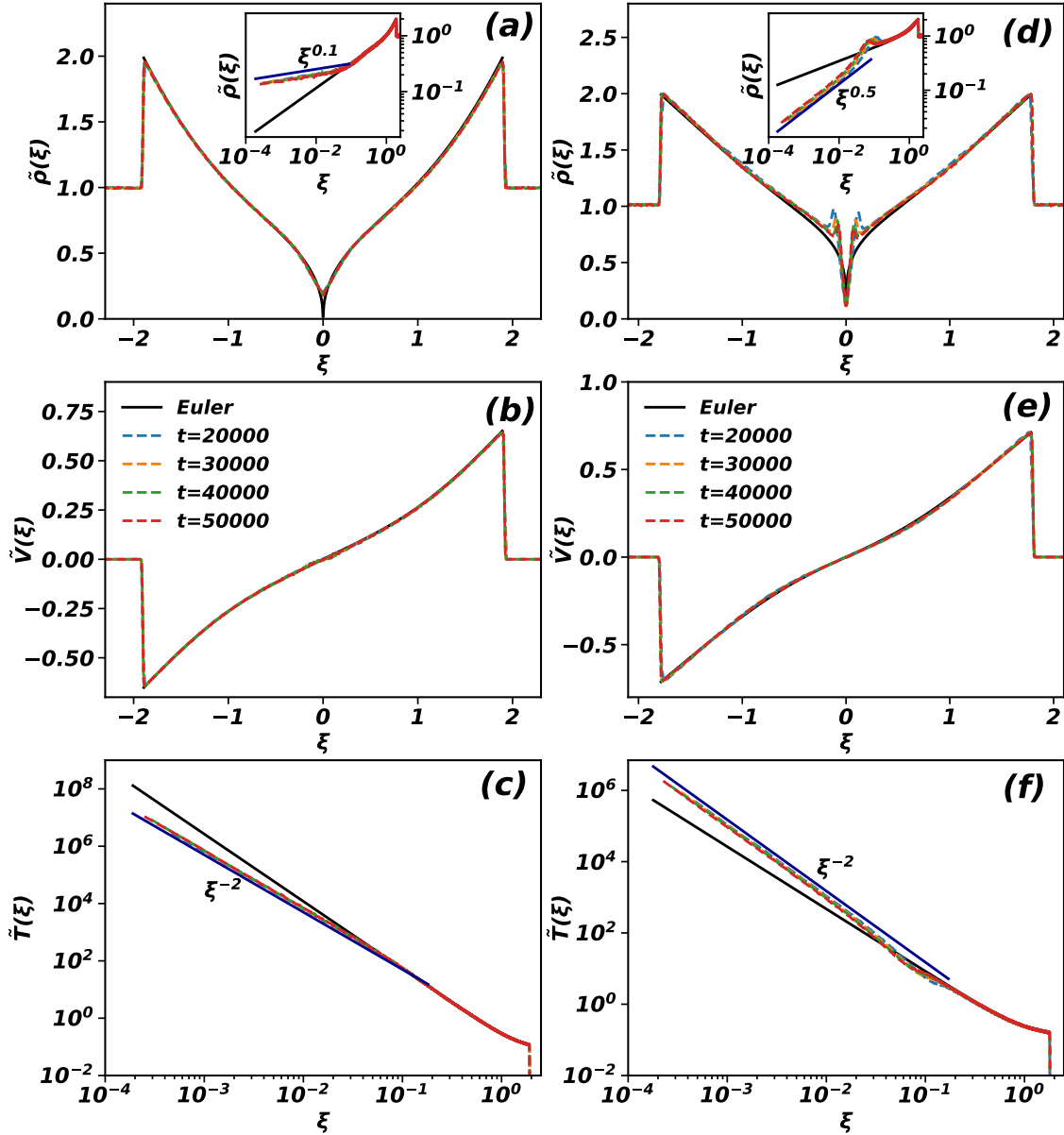


Figure 5.4: The comparison of  $\tilde{R}(\xi)$ ,  $\tilde{V}(\xi)$ , and  $\tilde{T}(\xi)$  obtained from the EDMD simulations with the exact solution for two different values of  $\beta = 0.1, 0.5$ . Figs. (a)-(c) represent the plot for  $\beta = 0.1$ , and the Figs. (d)-(f) represent the plots for  $\beta = 0.5$ . The broken coloured lines represent the EDMD results at four different times, and solid black lines represent the exact solution. Insets show the same data on the logarithmic scale. Solid dark blue lines represent the power law fitting of the data of density and temperature profiles obtained from the EDMD.



$$\partial_t(\rho u) + \partial_x(\rho u^2 + p) = \partial_x(\zeta \partial_x u), \quad (5.42)$$

$$\partial_t\left(\frac{1}{2}\rho u^2 + \frac{1}{2}\rho T\right) + \partial_x\left(\left[\frac{1}{2}\rho u^2 + \frac{1}{2}\rho T + p\right]u\right) = \partial_x(u\zeta \partial_x u + \lambda \partial_x T), \quad (5.43)$$

where  $\zeta$  and  $\lambda$  are the bulk viscosity, and the heat conduction of the system, respectively. According to the Green-Kubo relations, both of these quantities depend on temperature as  $T^{1/2}$  in one dimension, while a recent study shows the heat conduction depend on density also as  $\lambda \sim \rho^{1/3}$  [100]. Accordingly, we take these quantities as

$$\lambda = C_1 \rho^{1/3} T^{1/2}, \quad (5.44)$$

$$\zeta = C_2 T^{1/2}. \quad (5.45)$$

We solve the Navier-Stokes equations (5.41)–(5.43) in the region  $-L/2 \leq x \leq L/2$ , numerically using MacCormack method [82]. MacCormack method provides an accuracy up to second order both in time discretisation  $\Delta t$ , and space discretization  $\Delta x$ . We take the initial condition at time  $t = 0$  as : gradually decreasing density  $\rho(x) = \rho_0 |x|^{-\beta}$  as in Eq. (5.1), zero velocity everywhere, and the initial temperature as

$$T(x, 0) = T_0 e^{\frac{-x^2}{2\sigma^2}}, \quad (5.46)$$

We choose  $L$  such that the shock does not reach to the edge of the system at its maximum integration time  $\tau$ . The values of the parameters used in the numerical integration are tabulated in Table 5.2.

### 5.5.2 Comparison between Euler equation, Simulation, and Navier-Stokes equations

Since  $C_1$  and  $C_2$ , the constants parameterising heat conductivity and bulk viscosity, are not known, we first perform a parametric study to understand their effect on the results. We fix both  $\beta = 0.5$  and time. We show the dependence of  $\tilde{R}$ ,  $\tilde{V}$ , and  $\tilde{T}$  on

Table 5.2: The values of parameters used in the numerical solution of the Navier-Stokes Eqs. (5.41)–(5.43).

Parameters	Values
$L$	10000
$\tau$	80000
$T_0$	0.01
$\sigma$	1
$\Delta r$	0.1
$\Delta t$	0.001
$C_1$	5
$C_2$	20

varying  $C_1$  keeping  $C_2$  fixed in Fig. 5.5(a)–(c) and on varying  $C_2$  keeping  $C_1$  fixed in Fig. 5.5(d)–(f). Introducing non-zero dissipation immediately changes the behaviour near the shock center to the correct power laws as seen in the EDMD simulations. Changing  $C_1$  and  $C_2$  changes the results near the shock center quantitatively, keeping the exponent of the power law unchanged. The velocity is unaffected by dissipation. Changing the values of the coefficients does not affect the results near the shock front. The change near the center indicates the heat conduction becomes important in the tiny region  $0 \leq |x| \leq X(t)$  (see Sec. 5.6) and becomes negligible in the region  $X(t) \leq |x| \leq R(t)$ .

In Fig. 5.6, we compare the  $\tilde{R}$ ,  $\tilde{V}$ , and  $\tilde{T}$  obtained from the exact solution of the Euler equation, EDMD, and the numerical solution of the Navier-Stokes equations for  $\beta = 0.1, 0.5$ , each for four different times. The Navier-Stokes data are for the choice  $C_1 = 5$ ,  $C_2 = 20$ , which we found to be a good approximation to the solution. Near the shock center, the EDMD results and the Navier-Stokes results show the same power law behaviour of density as  $\tilde{R} \sim \xi^\beta$  (inset plots), and the temperature as  $\tilde{T} \sim \xi^{-2}$  (Figs.(c), (f)), unlike the exact solution of the Euler equation. We find excellent agreement between the Navier-Stokes data and the EDMD data everywhere, which indicates that the Navier-Stokes equations are the correct description of the theory for the inhomogeneous gas also.

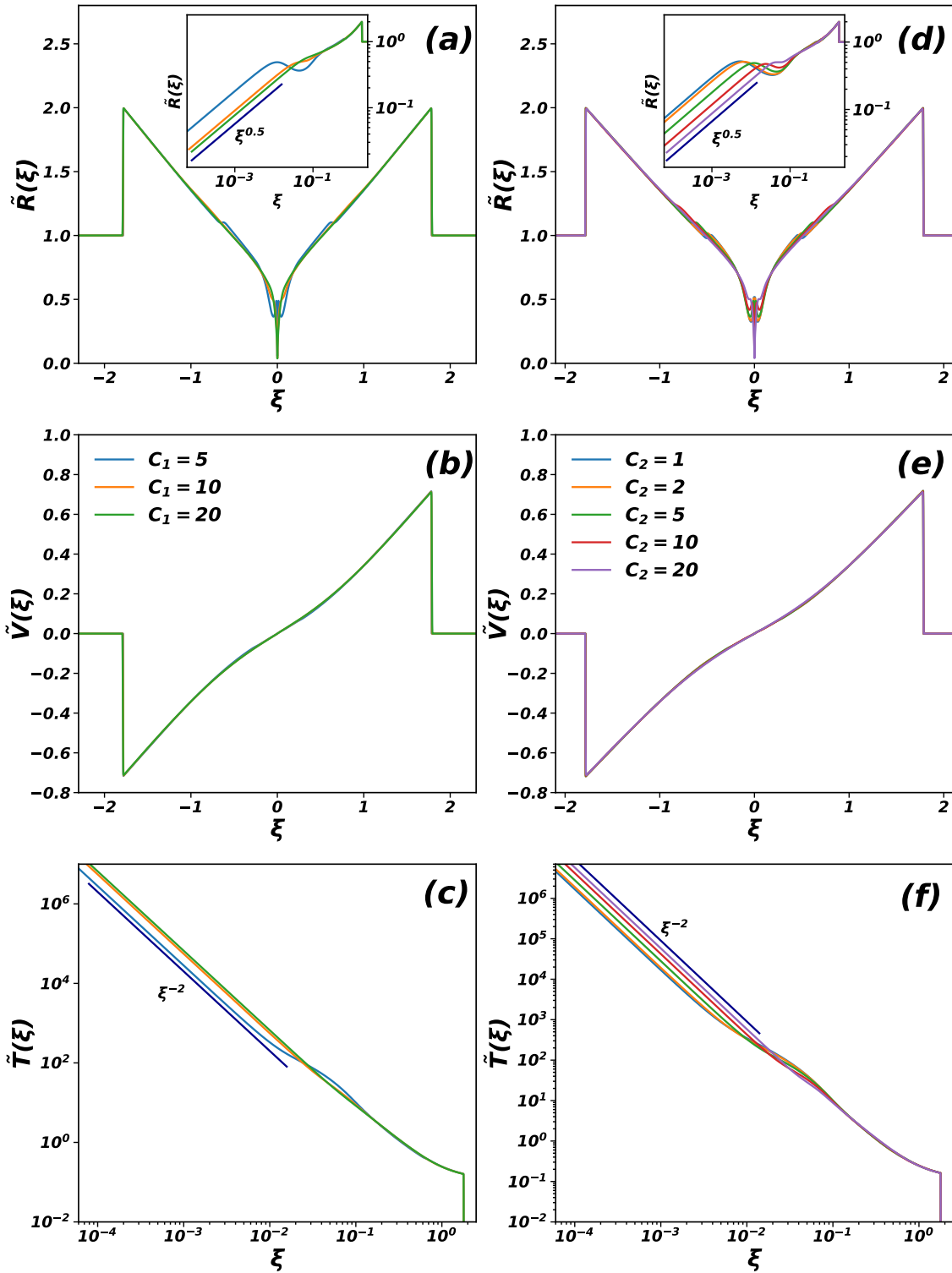


Figure 5.5: The variation of  $\tilde{R}(\xi)$  (a,d),  $\tilde{V}(\xi)$  (b,e), and  $\tilde{T}(\xi)$  (c,f) with  $\xi$ , obtained from the numerical solution of Navier-Stokes equations, for  $\beta = 0.5$ . Figs. (a)–(c) correspond to the data for three different values of coefficient of heat conduction  $C_1 = 5, 10, 20$  with  $C_2 = 5$  fixed, and the Figs. (d)–(f) correspond to the data for five different values of coefficient of bulk viscosity  $C_2 = 1, 2, 5, 10, 20$  with  $C_1 = 5$  fixed. The solid dark blue lines represent the power law fitting of the data of density and temperature profiles. The insets are the densities on the logarithmic scale.

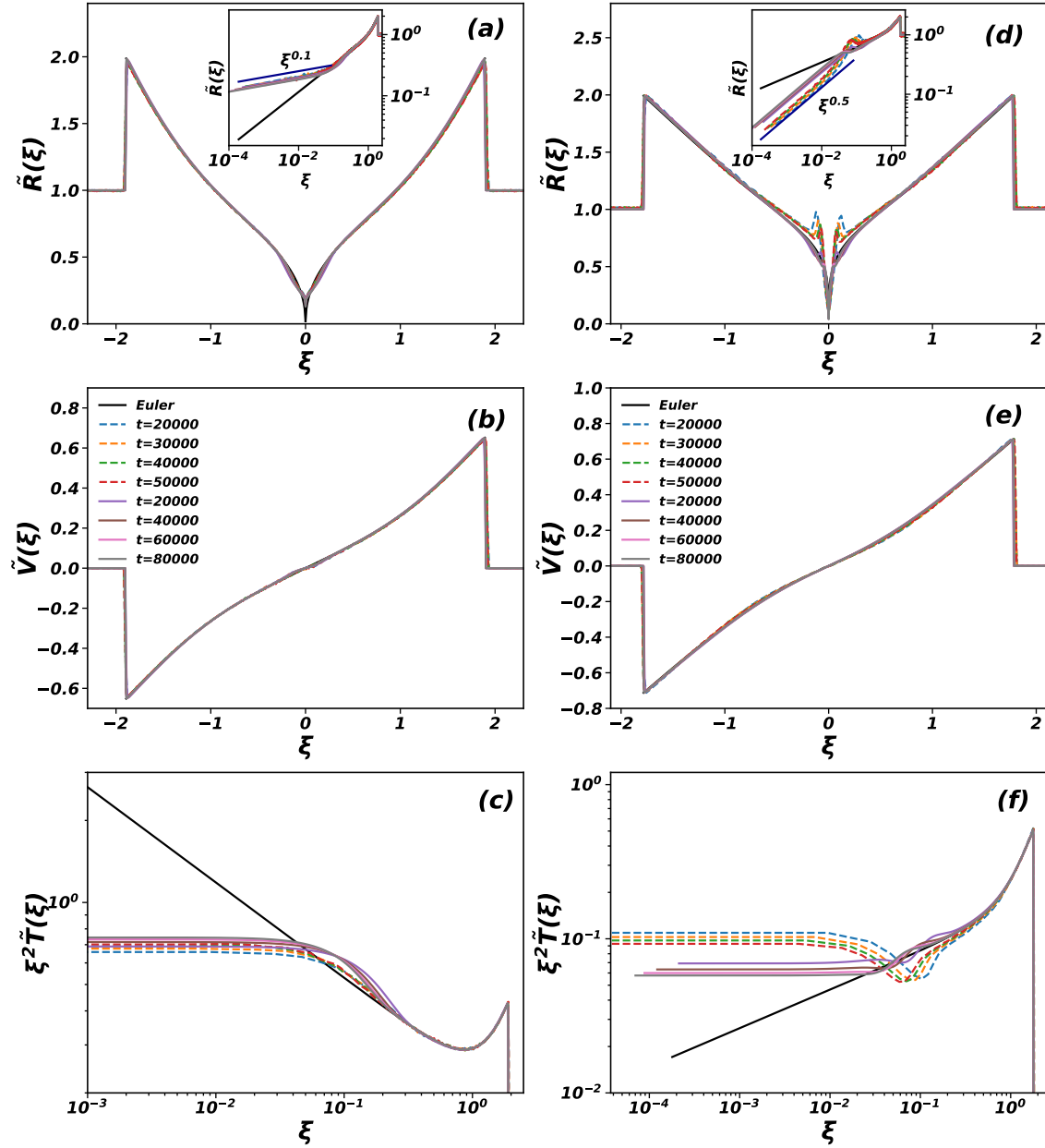


Figure 5.6: The comparison of density  $\tilde{R}(\xi)$ , velocity  $\tilde{V}(\xi)$ , and temperature  $\tilde{T}(\xi)$  obtained from the EDMD results with the solution of Euler equation, and the numerical integration of Navier-Stokes equations. Figs. (a)-(c) represent the plots for  $\beta = 0.1$ , and the Figs. (d)-(f) represent the plots for  $\beta = 0.5$ . The dashed coloured lines represent the EDMD results, solid black lines represent the exact solution of Euler equation, and the solid coloured lines represent the numerical integration of Navier-Stokes equations. The insets are the density plots on logarithmic scale. Solid dark blue lines represent the power law fitting of the data of density and temperature. For the integration of the Navier-Stokes equations,  $\beta = 0.1$  with  $\rho_0 = 15.8$ , and  $\beta = 0.5$  with  $\rho_0 = 260$  and  $C_1 = 5$ ,  $C_2 = 20$ .

## 5.6 Scaling near the shock center in one dimension

Due to inclusion of the heat conduction, an extra core scaling arises in the region  $0 \leq |x| \leq X(t)$ ,  $X(t)$  being the size of the core [18]. We follow the procedure followed in Ref. [18] to find the crossover scaling for the homogeneous case, to find the core size  $X(t)$  and the resultant scaling near the shock center for the inhomogeneous case.

In one dimension, near the shock center, the exact solution of the Euler equation [see Eqs. (5.30)–(5.31)] gives temperature and density for  $x \rightarrow 0$  as

$$T(x, t) \sim |x|^{\frac{3\beta-1}{2}} t^{\frac{1+\beta}{\beta-3}}, \quad (5.47)$$

$$\rho(x, t) \sim |x|^{\frac{1-3\beta}{2}} t^{\frac{1-\beta}{\beta-3}}. \quad (5.48)$$

In the region  $0 \leq |x| \leq X(t)$  the heat conduction dominates the Euler terms, while in the region  $X(t) \leq |x| \leq R(t)$  Euler terms dominate the heat conduction term, where the core size  $r = X(t)$  is the location where both the terms become comparable. From the Eq. (5.43), equating the Euler term with the heat conduction term i.e.  $\frac{\rho T}{t} \sim \frac{\rho^{1/3} T^{3/2}}{|x|^2}$ , valid only for  $\beta \neq \beta_c$  (for  $\beta = \beta_c$ , see below), and using  $T$  and  $\rho$  as in Eqs. (5.47) and (5.48), with  $|x| = X(t)$ , we obtain the size of the core as

$$X(t) \sim t^{\frac{2(19-13\beta)}{(3-\beta)(31-21\beta)}}, \quad \beta \neq \beta_c. \quad (5.49)$$

When  $\beta = \beta_c$ , the leading contribution to the heat conduction term has to be calculated explicitly. Now,

$$\rho \sim \frac{2^{3/2}}{3^{3/4}} \left( \frac{\xi_f}{R(t)} \right)^{1/3} + \dots, \quad \beta = \beta_c, \quad x \rightarrow 0 \quad (5.50)$$

$$T \sim \frac{1}{2\sqrt{3}} \frac{\xi_f^2}{t^2 R(t)^2} + \frac{x^2}{3t^2} + \dots, \quad \beta = \beta_c, \quad x \rightarrow 0. \quad (5.51)$$

The Euler term scales as  $\rho T/t \sim t^{-7/4}$ , while the heat conduction term scales as  $\lambda/t^2 \sim \rho^{1/3} \sqrt{T}/t^2 \sim t^{-7/3}$ . Thus, for  $\beta = \beta_c$ , the heat conduction term is always sub-dominant and can be ignored throughout the shock region. In this case there is no crossover length scale  $X(t)$ .

We now define a new rescaled distance  $\xi' = x/X(t)$  near the shock center. With the help of Eqs. (5.47)–(5.48), and Eq. (5.49), we define the thermodynamic quantities near the shock center in terms of new scaling  $\xi'$  as

$$\rho(x, t) \sim t^{\frac{6(3\beta^2 - 3\beta - 2)}{(3-\beta)(31-21\beta)}} \tilde{R}'(\xi'), \quad (5.52)$$

$$u(x, t) \sim t^{-\frac{21\beta^2 - 68\beta + 55}{21\beta^2 - 94\beta + 93}} \tilde{V}'(\xi') \approx \frac{X(t)}{t} \tilde{V}'(\xi'), \quad (5.53)$$

$$T(x, t) \sim t^{-\frac{2(5-3\beta)^2}{(3-\beta)(31-21\beta)}} \tilde{T}'(\xi'), \quad (5.54)$$

while near the shock front, the system follows the scaling (see Eqs. (5.8-5.11)),

$$\rho(x, t) \sim t^{-\frac{2\beta}{3-\beta}} \tilde{R}''(\xi), \quad (5.55)$$

$$u(x, t) \sim t^{\frac{\beta-1}{3-\beta}} \tilde{V}''(\xi), \quad (5.56)$$

$$T(x, t) \sim t^{\frac{2(\beta-1)}{3-\beta}} \tilde{T}''(\xi), \quad (5.57)$$

where  $\tilde{R}'$ ,  $\tilde{V}'$ ,  $\tilde{T}'$ , and  $\tilde{R}''$ ,  $\tilde{V}''$ ,  $\tilde{T}''$  are the resultant non-dimensionalised thermodynamic quantities near the shock center, and near the shock front respectively.

We numerically confirm the scaling in Fig. 5.7, where the scaling near the shock front [Eqs. (5.55)–(5.57)] is shown in Fig. 5.7(a)–(c), while the the core scaling [Eqs. (5.52)–(5.54)] is shown in Fig. 5.7(d)–(f) for EDMD data for  $\beta = 0.5$ . The data for different times show excellent data collapse in the appropriate regimes.

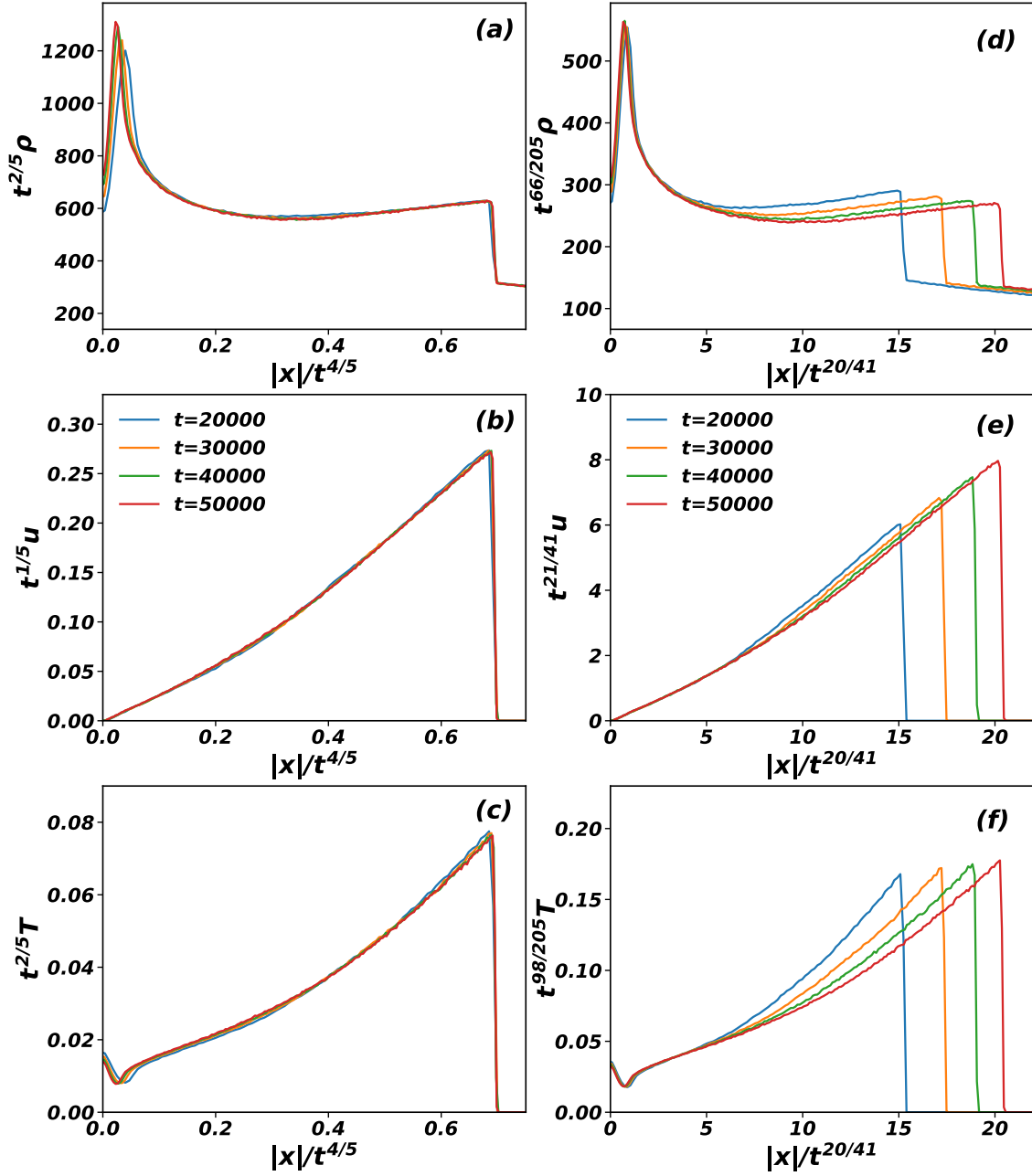


Figure 5.7: The scalings of thermodynamic quantities of density  $\rho$ , velocity  $u$ , and temperature  $T$  obtained from the EDMD results at four different times for  $\beta = 0.5$  with  $\rho_0 = 260$ . Figs. (a)-(c) represent the plots for front scaling Eqs. (5.55)–(5.57), and the Figs. (d)-(f) represent the plots for core scaling Eqs. (5.52)–(5.54). Near the shock center, core scaling shows better collapse than front scaling.

## 5.7 Behaviour for critical $\beta_c$

In Sec. 5.3.4, we derived a critical  $\beta_c = d/\gamma$ . For this critical value of  $\beta$ , the solution of the Euler equation satisfies the boundary condition  $\nabla T = 0$  at the shock center. Hence, we expect that the Euler equation should provide a good description of the EDMD data both at the shock center as well as the shock front.

We check numerically whether this is true for  $\beta_c = 1/3$  in 1-dimension.  $\tilde{R}$ ,  $\tilde{V}$ , and  $\tilde{T}$  obtained in EDMD simulations for four different times and  $\beta = 1/3$  are compared with the exact solution of the Euler equation in Fig. 5.8. Excellent agreement is seen for all the thermodynamic quantities both at the shock front as well as the shock center.

## 5.8 Summary and Discussion

In summary, we studied the spatio-temporal evolution of density, velocity, and temperature following an explosion in an ideal gas with an initial inhomogeneous density distribution  $\rho(r) = \rho_0 r^{-\beta}$ . We generalised the exact solution of the Euler equation, consistent with the Rankine-Hugoniot boundary conditions, to  $d$ -dimensions. From the asymptotic behaviour of the solution near the shock center, we argue that only for  $\beta_c = d/\gamma$ , should the Euler equation provide a full description of the problem. Using EDMD simulations in one dimension, we show that the Euler equation does not describe the data near the shock center. On the other hand the Navier-Stokes equations are able to overcome this issue. The crossover length scale below which the dissipation terms are relevant are derived for arbitrary  $\beta$ . The core scaling for the data near the shock center are also derived for arbitrary  $\beta$  and confirmed in EDMD simulations.

The results in this chapter generalises the known results for explosion in a homo-



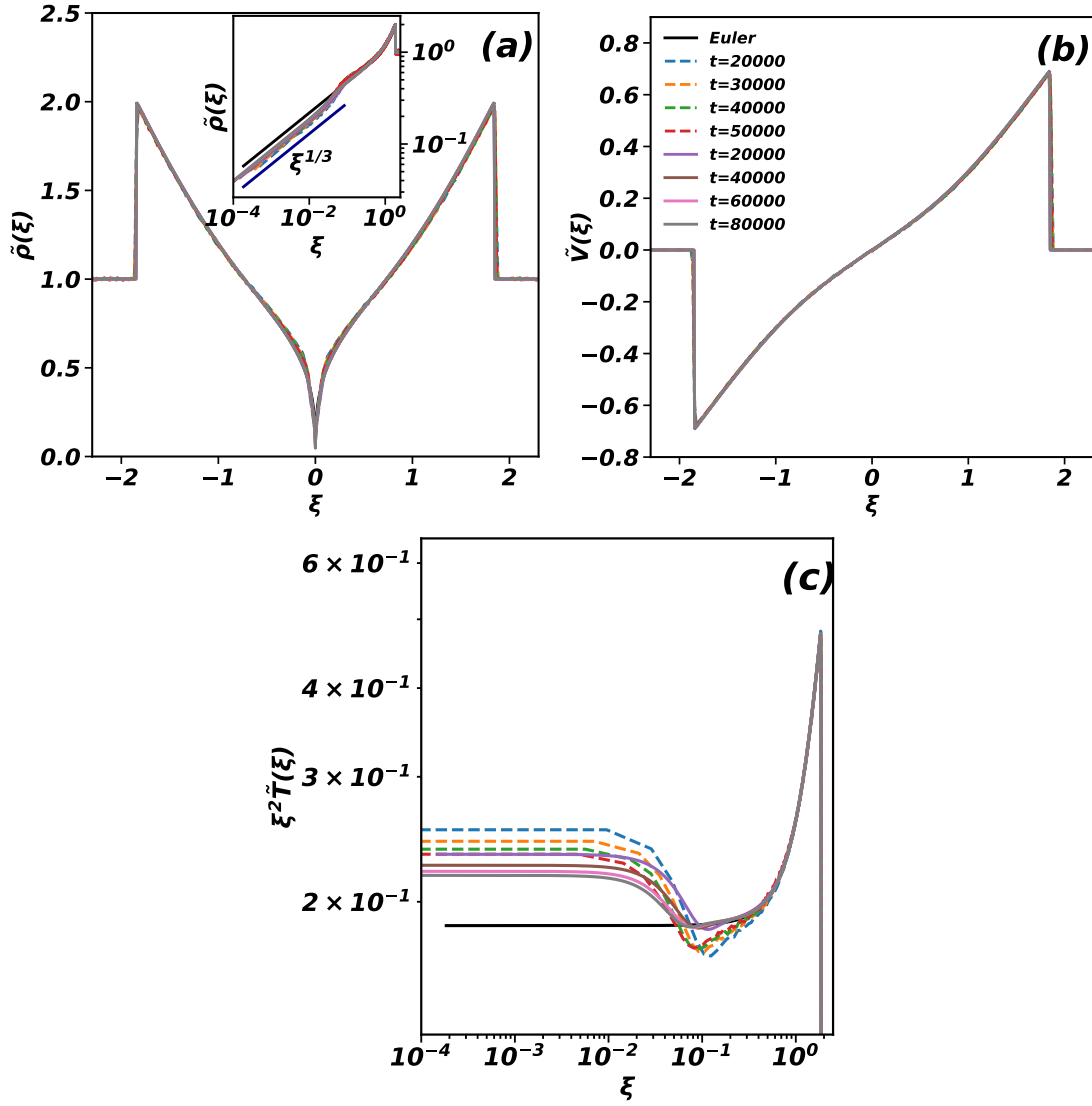


Figure 5.8: For  $\beta_c = 1/3$ , the EDMD data for (a) density  $\tilde{R}(\xi)$ , (b) velocity  $\tilde{V}(\xi)$ , and (c) temperature  $\tilde{T}(\xi)$  are compared with the exact result for the Euler equation, and the DNS results of NSE. The dashed coloured lines represent the EDMD data at four different times, solid coloured lines represent the DNS results at four different times, and solid black lines represent the exact solution of Euler equation. The inset is the same data on logarithmic scale. Solid dark blue line represents the power law fitting of the data of density.

geneous gas, a problem that is much better studied. By doing so, it is possible to pinpoint the exact reason why the Euler equation fails, even though it is the equation that satisfies the scaling limit. For the value of  $\beta$  for which the solution to the Euler equation satisfies  $\nabla T = 0$ , and  $T$  a finite non-zero value, close to the shock center the Euler equation is able to describe the data everywhere and not just near the shock front. The condition  $\nabla T = 0$  is satisfied in two dimensions, also for  $\beta > 3/2$ . It would be interesting to see whether the Euler equation provides a complete description of the problem for  $\beta > 3/2$ , thereby leading to a more complete understanding of the boundary conditions when heat conduction is present.

It is possible to look at shocks in initial density profiles different from the power law profile  $\rho = \rho_0 r^{-\beta}$ . It is not possible in general to find self-similar solutions to the Euler equation. However, the growth of the radius of the shock front can be determined by examining the large  $r$  behaviour of the initial density profile. For instance, if the density profile is a constant at large  $r$ , we expect the shock to behave as for a blast in a medium at constant density. To show this, we simulate blasts in two different density profiles:

$$\rho(r) = \rho_0 + \rho_1 r^{-\beta}, \quad (5.58)$$

$$\rho(r) = \rho_0 + \rho_1 \exp\left(-\frac{r}{\sigma}\right). \quad (5.59)$$

This is confirmed in Fig. 5.9, where the results of the EDMD simulations for the shock radius for these initial density profiles in one dimension is shown to agree with that of a blast in a medium at constant density. Likewise, we would expect that adding a perturbation to the initial power law distribution at small distances will not affect the large time behaviour.

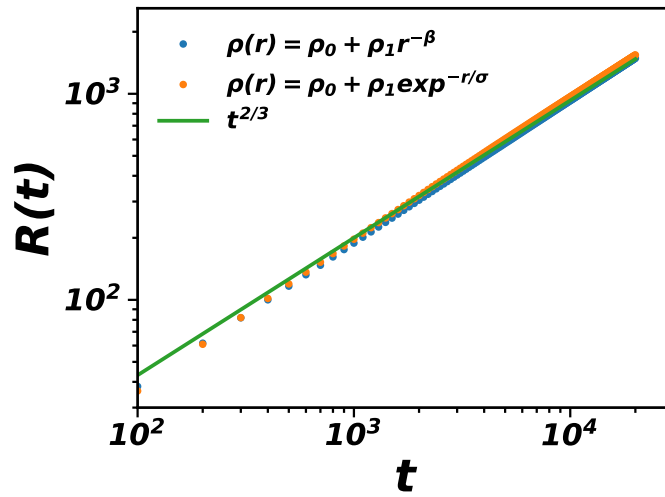


Figure 5.9: The variation of the radius of the shock front with time for two different initial density profiles (see Eqs. (5.58)–(5.59)). For a blast in such systems, at late times, the radius follows the same power-law growth as for a blast in a system with a uniform initial density profile. The plots represent the EDMD data with parameters:  $\rho_0 = 10$ ,  $\rho_1 = 20$ ,  $\sigma = 15$ , and  $\beta = 0.3$  in one dimension.



# 6

## Splash in an inhomogeneous gas in one dimension: Exact analysis and molecular dynamics simulations

### Related Publication :

This chapter is based on the following publication [101]:

Splash in an inhomogeneous gas in one dimension: Exact analysis and molecular dynamics simulations,

**Amit Kumar** and R. Rajesh, *arXiv preprint arXiv:2504.03549*, 2025.



### 6.1 Introduction

In the previous chapters, we have considered only the isotropic cases of the initial density distributions of the ambient gas. The gas could be initially spatially isotropic

or anisotropic. We will refer to the isotropic case as the blast problem, which is very well studied for both the homogeneous and inhomogeneous gas where  $\rho(r, 0) = \rho_0 r^{-\beta}$ . Due to point symmetry, these thermodynamic quantities depend only on radial distance  $r$  and time  $t$ . The scaling exponents are easily obtained using dimensional analysis. It is known that near the shock front, the shock is well described by Euler equation, while near the shock center, there is a crossover to a region where heat conduction become important, and the hydrodynamics is described by the Navier-Stokes equations [4–7, 13–18, 80, 83, 94–96].

The gas could be initially spatially anisotropic. A special case is one when there is vacuum in half the space and a gas in the other half. Energy is input at a point in the interface. We will refer to this problem as the splash problem. This problem is less studied in comparison to the blast problem. In a recent paper, the splash problem was studied in one dimension when the gas is homogeneous [12]. The energy is reflected back into the vacuum, and in the scaling regime the total energy of medium (gas) decays as  $E(t) \sim t^{-\delta_s}$ . The value of  $\delta_s = 0.11614383675\dots$  has been obtained for the homogeneous medium in one dimension by analysing the Euler equation, using self-similarity of the second kind. The value of  $\delta_s$  was obtained by arguing that the singular points in the Euler equation should be canceled by zeros elsewhere. The results were validated using molecular dynamics simulations of hard point particles of different masses with alternate particles having same mass [12].

In this chapter, we generalise the results for the splash problem to an inhomogeneous gas in one dimension. The system is composed of vacuum in the region  $x < 0$  and an inhomogeneous medium in the region  $x \geq 0$ , with an initial density distribution  $\rho(x) = \rho_0 |x|^{-\beta}$ . Using the Euler equation, we determine exactly  $\delta_s$  and the shock front growth exponent  $\alpha$  as functions of  $\beta$ . These results are verified using event-driven molecular dynamics simulations. In addition, we find that the thermodynamic quantities obtained from the Euler equation match well with those from

---

the EDMD simulations for all values of  $\beta$ .

The remainder of this chapter is as follows. In Sec. 6.2, we describe the Euler equation in terms of rescaling functions. In Sec. 6.3, we simplify the Euler equation and find the singular points. Using these point we show the curves of  $\delta_s$  and singular points with  $\beta$ . We describe the particles based simulation models for point particles in Sec. 6.4, and show the power law behavior of energy and radius of shock front. In Sec. 6.5, we compare the similarity exponents and thermodynamic quantities form EDMD and Euler equation. Sec. 6.6 contains the summary and discussion. The content of this chapter is published in Ref. [101].

## 6.2 Model and continuity equations

In this section, we describe the model, scaling analysis, and the continuity equations describing the evolution of the thermodynamic quantities. Consider a gas in one dimension. Initially the particles are such that it is vacuum in the region  $x < 0$  and an inhomogeneous medium in the region  $x \geq 0$ , with an initial density distribution that varies with distance  $x$  as  $\rho(x) = \rho_0|x|^{-\beta}$ , where  $0 \leq \beta < 1$ . At time  $t = 0$ , energy  $E_0$  is introduced at  $x = 0$ . This creates a shock front that propagates into the medium. Let the shock front be at a distance  $R(t)$  at time  $t$ . We assume a power law growth

$$R(t) \sim t^\alpha, \quad t \rightarrow \infty. \quad (6.1)$$

Due to the vacuum in  $x < 0$ , the pressure is zero for  $x < 0$ , leading to a reflection of the energy towards the vacuum. At long times, the energy in  $x > 0$  decreases to zero. We introduce an exponent for this decay:

$$E(t) \sim t^{-\delta_s}, \quad t \rightarrow \infty. \quad (6.2)$$

The aim of the chapter is to determine  $\alpha, \delta_s$  as a function of  $\beta$ , and then the spatio-temporal behaviour of the different thermodynamic quantities.

---

The two exponents  $\alpha$  and  $\delta_s$  are not independent of each other and can be related to each other through scaling arguments. The total number of moving particles in the medium,  $N(t)$ , scales as  $N(t) \sim R(t)^{1-\beta}$ . The typical speed of a particle is  $\dot{R}(t)$ . Then the total energy of the medium scales as  $E(t) \sim N(t)\dot{R}^2 \sim t^{\alpha(3-\beta)-2}$ . From Eq. (6.2), we obtain

$$\alpha = \frac{2 - \delta_s}{3 - \beta}, \quad (6.3)$$

The propagation of the disturbance into the medium due to the splash at the origin is described by the density  $\rho$ , velocity  $u$ , temperature  $T$ , and pressure  $p$  fields. In the hydrodynamic regime, the continuity equations of mass, momentum, and entropy which govern the evolution of these thermodynamic quantities in one dimension are given by [1–3, 11]:

$$\partial_t \rho + \partial_x (\rho u) = 0, \quad (6.4)$$

$$\rho(\partial_t + u\partial_x)u + \partial_x p = 0, \quad (6.5)$$

$$\partial_t \left( \frac{p}{\rho^3} \right) + u\partial_x \left( \frac{p}{\rho^3} \right) = 0. \quad (6.6)$$

The continuity equation (6.5) is known as the Euler equation. By assuming local equilibrium, the local pressure is related to the local temperature and density through the equation of state, which we take to be the ideal gas equation of state:

$$p = k_B \rho T, \quad (6.7)$$

where  $k_B$  is the Boltzmann constant, which we set to 1.

Across the shock front, the thermodynamic quantities become discontinuous. The values of the thermodynamic quantities at the shock front can be determined by equating the fluxes across the shock front, which lead to the Rankine-Hugoniot boundary conditions [3, 11, 94], which adapted to the inhomogeneous gas reduce to

$$\rho_1 = 2\rho_0 R^{-\beta}, \quad (6.8)$$

$$u_1 = \frac{1}{2} \dot{R}, \quad (6.9)$$



$$p_1 = \frac{1}{2} \rho_0 \dot{R}^2 R^{-\beta}, \quad (6.10)$$

where the subscript 1 denotes the quantities just behind the shock front, and  $\dot{R}$  is the speed of the shock front.

We define the following non-dimensionalised functions for the different thermodynamic quantities [2, 11]:

$$\xi = \frac{x}{R(t)}, \quad (6.11)$$

$$\tilde{G} = \frac{R^\beta}{\rho_0} \rho(x, t), \quad (6.12)$$

$$\tilde{V} = \frac{u(x, t)}{\dot{R}}, \quad (6.13)$$

$$\tilde{Z} = \frac{3}{\dot{R}^2} T(x, t). \quad (6.14)$$

Substituting these into the partial differential equations (6.4) to (6.6), we obtain ordinary differential equations for the scaling functions  $\tilde{G}$ ,  $\tilde{V}$ , and  $\tilde{Z}$ :

$$(\tilde{V} - \xi) \frac{d\tilde{G}}{d\xi} + \tilde{G} \frac{d\tilde{V}}{d\xi} - \beta \tilde{G} = 0, \quad (6.15)$$

$$(\tilde{V} - \xi) \frac{d\tilde{V}}{d\xi} + \frac{1}{3} \frac{d\tilde{Z}}{d\xi} + \frac{\tilde{Z}}{3\tilde{G}} \frac{d\tilde{G}}{d\xi} + \left(1 - \frac{1}{\alpha}\right) \tilde{V} = 0, \quad (6.16)$$

$$(\tilde{V} - \xi) \frac{d}{d\xi} \left( \frac{\tilde{Z}}{\tilde{G}^2} \right) + \left(2 + 2\beta - \frac{2}{\alpha}\right) \frac{\tilde{Z}}{\tilde{G}^2} = 0. \quad (6.17)$$

In terms of the scaling functions, the Rankine-Hugoniot boundary conditions (6.8) to (6.10) reduce to

$$\tilde{G}(1) = 2, \quad (6.18)$$

$$\tilde{V}(1) = \frac{1}{2}, \quad (6.19)$$

$$\tilde{Z}(1) = \frac{3}{4}. \quad (6.20)$$

Since the differential forms of Eqs. (6.15)–(6.17) become singular at  $\xi = \xi_s$  (see Section 6.3), scaling solutions for the thermodynamic quantities cannot be extended

into the region  $\xi < \xi_s$ . To obtain a complete solution over the full domain  $\xi \in (-\infty, 1]$ , an additional boundary condition is required in the region  $\xi < \xi_s$ , in addition to the Rankine-Hugoniot conditions, to smoothly connect the left-side solution ( $\xi < \xi_s$ ) with the right-side solution ( $\xi > \xi_s$ ) at  $\xi = \xi_s$ .

Although finding the scaling solution in the vacuum region is beyond the scope of this chapter, the following boundary conditions, as suggested in Ref. [12], can be employed numerically to extend the scaling solution into the vacuum:

$$\tilde{G}(\xi \rightarrow -\infty) = 0, \quad (6.21)$$

$$\tilde{V}(\xi \rightarrow -\infty) = -\infty, \quad (6.22)$$

$$\tilde{Z}(\xi \rightarrow -\infty) = 0. \quad (6.23)$$

## 6.3 Exact solution of the exponent $\alpha$

In the splash problem, the energy in the hydrodynamic region decays continuously over time, and a closed-form solution for the thermodynamic quantities including the exponent  $\delta_s$  cannot be obtained solely from scaling arguments, making this a self-similar problem of the second kind. Solutions to such self-similar problems have been studied in the context of implosions, where the shock approaches the center of symmetry from infinity [3, 43–46]. For self-similar solutions of the second kind, one treats the ordinary differential equations (6.15) to (6.17) as an eigenvalue problem and seeks the unique value of  $\alpha$  for which the solution curves are single-valued over the range of  $\xi$ .

After simplifying Eqs. (6.15) to (6.17) and solving for  $d\tilde{G}/d\xi$ ,  $d\tilde{V}/d\xi$ , and  $d\tilde{Z}/d\xi$ ,

we obtain

$$\frac{d\tilde{G}}{d\xi} = \frac{\tilde{G}[(\alpha\beta + \alpha - 1)(3\tilde{V}^2 - 2\tilde{Z}) - 3\xi\tilde{V}(2\alpha\beta + \alpha - 1) + 3\alpha\beta\xi^2]}{3\alpha(\tilde{V} - \xi)((\tilde{V} - \xi)^2 - \tilde{Z})}, \quad (6.24)$$

$$\frac{d\tilde{V}}{d\xi} = -\frac{\tilde{Z}[\alpha(\beta - 2) + 2] + 3(\alpha - 1)\tilde{V}(\tilde{V} - \xi)}{3\alpha((\tilde{V} - \xi)^2 - \tilde{Z})}, \quad (6.25)$$

$$\frac{d\tilde{Z}}{d\xi} = \frac{2\tilde{Z}[3(\alpha - 1)\xi(\tilde{V} - \xi) + \tilde{Z}(\alpha\beta + \alpha - 1)]}{3\alpha(\tilde{V} - \xi)((\tilde{V} - \xi)^2 - \tilde{Z})}. \quad (6.26)$$

These equations blow up simultaneously when  $\tilde{Z}(\xi) = (\tilde{V}(\xi) - \xi)^2$ . We denote the singular point as  $\xi_s$ . In order for the scaling functions  $\tilde{G}$ ,  $\tilde{Z}$ , and  $\tilde{V}$  to be single-valued functions of  $\xi$ , both the numerator and denominator of Eqs. (6.24) to (6.26) must simultaneously vanish at  $\xi = \xi_s$ . The common roots of Eqs. (6.24) to (6.26) for which both the numerator and denominator vanish are:

$$\tilde{Z}(\xi_s) = \frac{9(\alpha - 1)^2}{(\alpha\beta + \alpha - 1)^2} \xi_s^2, \quad (6.27)$$

$$\tilde{V}(\xi_s) = \frac{\alpha(\beta - 2) + 2}{\alpha\beta + \alpha - 1} \xi_s. \quad (6.28)$$

The above equations allow us to determine, numerically exactly, the exponent  $\delta_s$ . The solution curve of the ordinary differential equations (6.24) to (6.26) must pass through the singular point  $(\tilde{Z}(\xi_s), \tilde{V}(\xi_s))$  in the  $\tilde{Z}$ - $\tilde{V}$  plane for the right choice of  $\delta_s$ . To iteratively determine  $\delta_s$ , we proceed as follows. We first assign a numerical value to  $\delta_s$ . We then solve numerically Eqs. (6.24)-(6.26) using Rankine-Hugoniot boundary conditions. From the solution for  $\tilde{Z}(\xi)$ , we determine  $\xi_s$  using Eq. (6.27). This, in turn allows us to determine  $\tilde{V}(\xi_s)$  from Eq. (6.28). We then check whether the numerical solution of  $\tilde{V}(\xi)$  is consistent with the value of  $\tilde{V}(\xi_s)$ . If  $\tilde{V}(\xi_s)$  from the solution is greater (smaller) than the value obtained from Eq. (6.28), we increase (decrease)  $\delta_s$  and repeat the process, till we obtain  $\delta_s$  to desired accuracy. We tabulate the values of  $\delta_s$  and  $\alpha$ , thus obtained, for different values of  $\beta$  in Table 6.1. In Fig. 6.1, we show the variation of  $\xi_s$  and the values of the thermodynamic quantities

Table 6.1: The different values of exponent of energy decay of the inhomogeneous medium for corresponding  $\beta$ . The different values are obtained by the second-kind self similar solution of the Euler equation (see eqs. (6.24) - (6.26)).

$\beta$	$\alpha$	$\delta_s$
0.0	0.627952	0.1161438368
0.1	0.653500	0.1048477306
0.2	0.681098	0.0929255989
0.3	0.710967	0.0803888757
0.4	0.743350	0.0672880460
0.5	0.778503	0.0537414570
0.6	0.816672	0.0399860573
0.7	0.858056	0.0264699100
0.8	0.902714	0.0140277900

at the singular points as a function of  $\beta$ . Curiously,  $\xi_s$  is not monotonic with  $\beta$ .

We now proceed to compare the values of  $\delta_s$  and other thermodynamic quantities obtained from the exact analysis of the Euler equation with those obtained from molecular dynamics simulations in one dimension.

## 6.4 Event driven molecular dynamics simulations

We first describe the particle-based model in one dimension that is used for the event-driven molecular dynamics simulations. Consider a line of length  $L$ , with a set of  $N$  point particles labeled  $1, 2, \dots, N$ , distributed in the region  $L/2 \leq x \leq L$ . The region  $0 \leq x < L/2$  is initially empty. To obtain the initial density  $\rho(x) = \rho_0|x|^{-\beta}$ , we assign the position  $x_i$  to each particle  $i$  as

$$x_i = \frac{L}{2} \left( 1 + q_i^{\frac{1}{1-\beta}} \right), \quad i = 1, 2, \dots, N \quad (6.29)$$

where  $q_i$  is a random number drawn from the the uniform distribution on  $[0, 1]$ .

Initially, all the particles are at rest. At time  $t = 0$ , a subset of  $N_c$  particles, selected from the region near the center, are given initial Gaussian velocities based on their

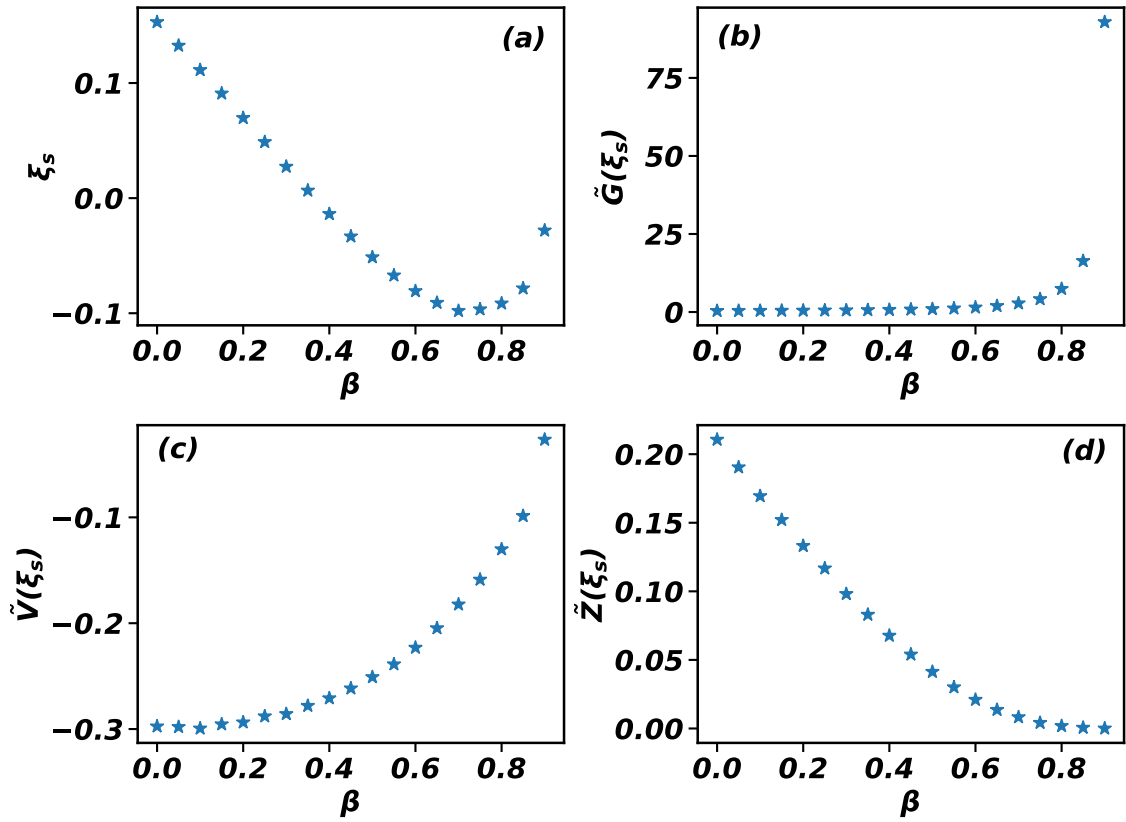


Figure 6.1: The variation of (a) singular point  $\xi_s$ , and the rescaled thermodynamic quantities: (b) density  $\tilde{G}$ , (c) velocity  $\tilde{V}$ , and (d) temperature  $\tilde{Z}$  at the singular point  $\xi_s$ , as a function  $\beta$ . The quantities are obtained from the numerical solution of the Euler equation (see eqs. (6.24) - (6.26)) using Rankine-Hugoniot boundary conditions.

positions:

$$u_i = u_0 \exp\left(-\frac{(x_i - L/2)^2}{2\sigma^2}\right), \quad (6.30)$$

where  $u_0$  and  $\sigma$  are positive constants. These initial velocities are then rescaled such that the total initial energy of the system is  $E_0$ . The system evolves in time through elastic collisions between particles. The particles move ballistically between their successive collisions, and the ordering of the particles is conserved throughout the evolution.

Since head-on collisions of particles with same masses simply exchange their velocities, making the dynamics of the system integrable, in what follows we take these particles as bi-dispersed particles of mass  $m_1$  and  $m_2$  with neighbouring particles having different masses [97–99]. The post collision velocities  $u'_i$  and  $u'_j$  of particles  $i$  and  $j$ , having pre collision velocity  $u_i$  and  $u_j$  respectively, after the collision are

$$u'_i = \frac{m_i u_i + m_j u_j + m_j (u_j - u_i)}{m_i + m_j}, \quad (6.31)$$

$$u'_j = \frac{m_j u_j + m_i u_i + m_i (u_i - u_j)}{m_i + m_j}. \quad (6.32)$$

The splatter results in particles escaping to the vacuum  $x < L/2$ . To avoid finite size effects, we remove the particles with coordinate  $x < x_0$ , where  $0 < x_0 \ll L/2$ . This is reasonable since the splatters move ballistically towards  $x \rightarrow -\infty$  and will not interact with the system again.

For our EDMD simulations, we use the following parameters: energy  $E_0 = 24$ , number of particles  $N = 32000$ , number of particles excited at the center  $N_c = 24$ , system size  $L = 16000$ , and masses  $m_1 = 1$  and  $m_2 = 2$ . We choose the simulation runtime such that the shock front does not reach the boundary at  $x = L$ .

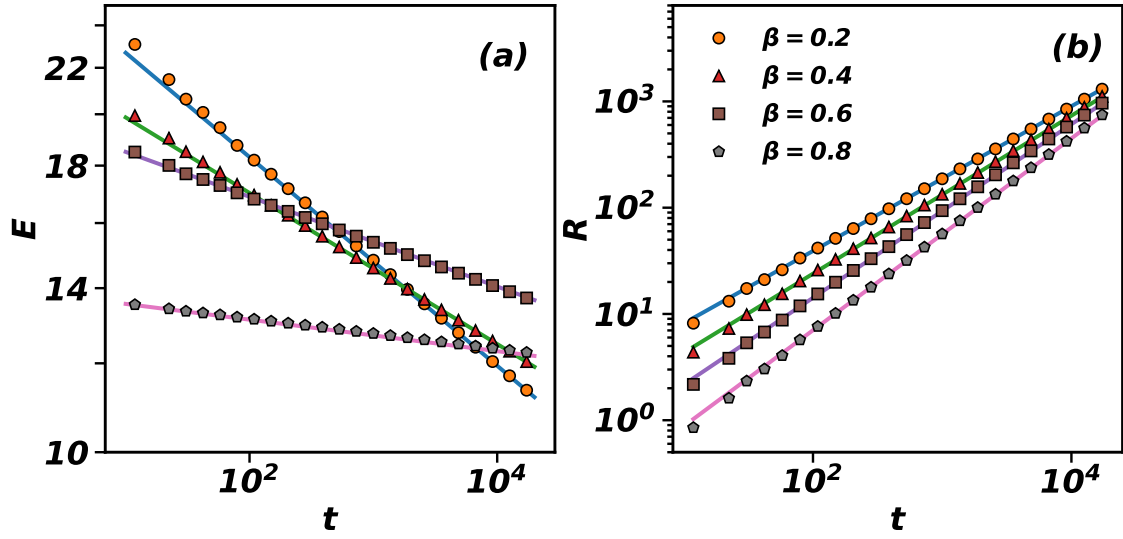


Figure 6.2: The power-law variation of (a) the energy  $E(t)$  in the inhomogeneous medium ( $x > 0$ ), and (b) the radius of the shock front  $R(t)$  with time  $t$ , is shown for four different values of  $\beta = 0.2, 0.4, 0.6$ , and  $0.8$ . The symbols correspond to the event-driven molecular dynamics simulation data, while the solid lines represent the best power-law fits. The exponents extracted from the EDMD data show excellent agreement with those obtained from the numerical solution of the Euler equation for both energy decay and shock front propagation.

## 6.5 Results

### 6.5.1 The exponents $\delta_s$ and $\alpha$

We first show how we extract the exponents  $\delta_s$  and  $\alpha$  from the EDMD data. The data for energy, obtained as the kinetic energy of all particles with  $x > L/2$ , and  $R(t)$ , obtained from the position of the right-most moving particle, shown in Fig. 6.2, are power-law in time spanning over more than a couple of decades. We fit the data to power-laws and it can be seen that we obtain excellent fits as the entire data can be fitted to one exponent.

The values of  $\delta_s$  and  $\alpha$  obtained from the EDMD simulations are compared with the exponents obtained from the exact analysis of the Euler equation (see Eqs. (6.24-6.26)) in Fig. 6.3. It can be seen that the results obtained from the two analysis are

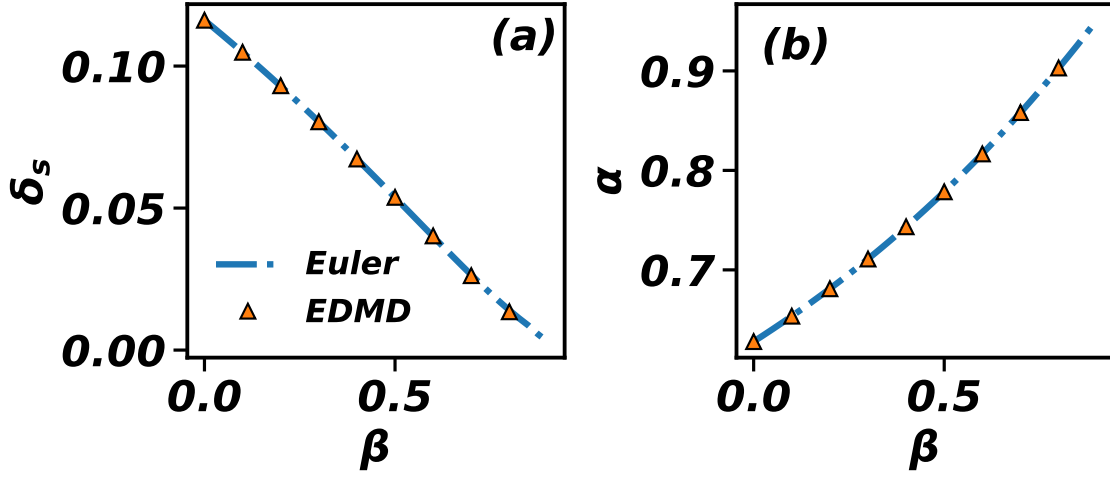


Figure 6.3: The comparison of (a) the power-law exponent of energy decay,  $\delta_s$ , in the region  $x > 0$ , and (b) the power-law exponent of the radius of shock front,  $\alpha$ , is shown. The dashed lines represent the values obtained from the exact analysis of the Euler equation, while the symbols correspond to the exponents extracted from the EDMD simulation data. The results demonstrate excellent agreement between the EDMD simulations and the theoretical predictions from the Euler equation.

in excellent agreement for the entire range of  $\beta$ .

### 6.5.2 Behaviour of Thermodynamic Quantities

To measure the thermodynamic quantities  $\rho(x, t)$ ,  $u(x, t)$ , and  $T(x, t)$ , we divide the system into bins of size  $\Delta$  and compute these quantities at spatial position  $x \in [0, L]$ .

The measured values of these quantities are given by:

$$\rho(x, t) = \left\langle \frac{\sum m_i \delta(x_i, x)}{\Delta} \right\rangle, \quad (6.33)$$

$$u(x, t) = \left\langle \frac{\sum m_i u_i \delta(x_i, x)}{\sum m_i \delta(x_i, x)} \right\rangle, \quad (6.34)$$

$$T(x, t) = \left\langle \frac{\sum m_i u_i^2 \delta(x_i, x)}{\sum m_i \delta(x_i, x)} \right\rangle - \left( \left\langle \frac{\sum m_i u_i \delta(x_i, x)}{\sum m_i \delta(x_i, x)} \right\rangle \right)^2. \quad (6.35)$$



Here,  $\langle \dots \rangle$  denotes the average over different initial configurations, and  $\delta(x_i, x)$  is the step function defined as

$$\delta(x_i, x) = \begin{cases} 1 & \text{if } |x - x_i| \leq \Delta/2, \\ 0 & \text{if } |x - x_i| > \Delta/2. \end{cases} \quad (6.36)$$

In Fig. 6.4, we show the spatial variation of  $\rho(x)$ ,  $u(x)$ , and  $T(x)$  at four different times for fixed  $\beta = 0.5$  [Fig. 6.4(a-c)], and, for fixed time and four values of  $\beta$  [Fig. 6.4(d-f)]. We observe that the shock front, indicated by the sharp jumps in the profiles, shifts over time, and the values of thermodynamic quantities at the shock front decrease with time. The results in Fig. 6.4(d-f) show that both the velocity and temperature increase monotonically from the shock center for all values of  $\beta$ . The density also increases monotonically from the shock center for lower values of  $\beta$ , reaching a maximum at the shock front. However, for larger values of  $\beta$ , the peak in density is no longer at the shock front, and decreases from a peak in the vacuum to the shock front.

Finally, we compare the thermodynamic quantities obtained from the Euler equation (see eqs. (6.15-6.17)) with those from the EDMD simulations. In Fig. 6.5(a-c), we see that the non-dimensionalised thermodynamic quantities at different times collapse onto a single curve, validating the scaling equations (6.11-6.14). The scaling function, obtained from the solution of the Euler equation with the exact solution for  $\delta_s$  (shown by lines), are in excellent agreement with the EDMD data over the range  $\xi \in [0, 1]$ , for all values of  $\beta$  considered.

## 6.6 Summary and Discussion

In this study, we investigated the splash problem where energy is initially input into a system consisting of a vacuum region for  $x < 0$  and an inhomogeneous medium

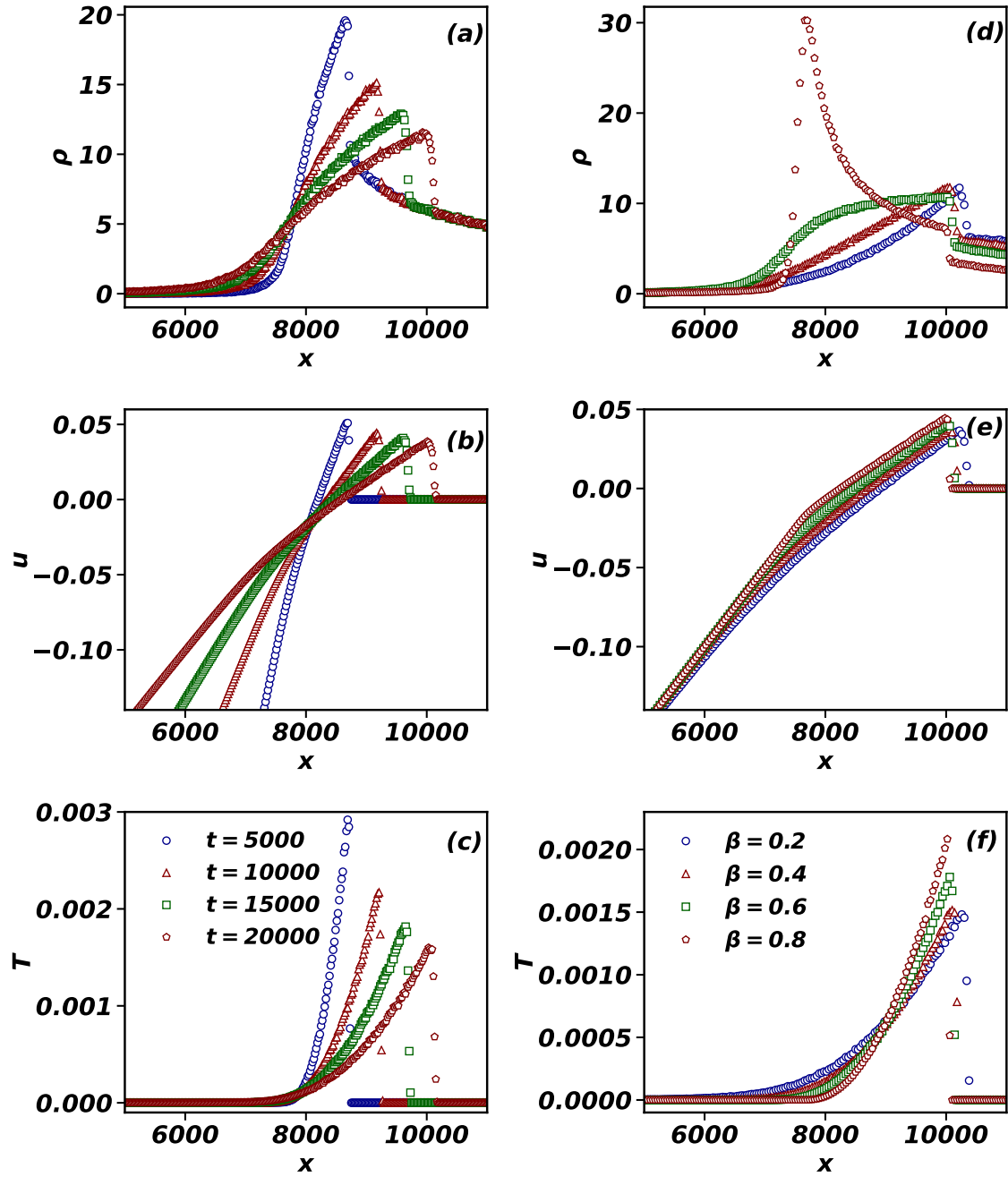


Figure 6.4: The spatial variation of density  $\rho(x,t)$ , velocity  $u(x,t)$ , and temperature  $T(x,t)$  is shown: panels (a)–(c) correspond to fixed  $\beta = 0.5$  at different times, while panels (d)–(f) correspond to a fixed time  $t = 2000$  with varying  $\beta$ . The top row illustrates that for  $\beta = 0.5$ , all thermodynamic quantities increase monotonically with distance, and the shock front moves rightward as time progresses. In the bottom row, at  $t = 20000$ , both velocity and temperature increase monotonically with distance, whereas the density profile develops a secondary peak in the vacuum region, whose prominence grows with increasing  $\beta$ .

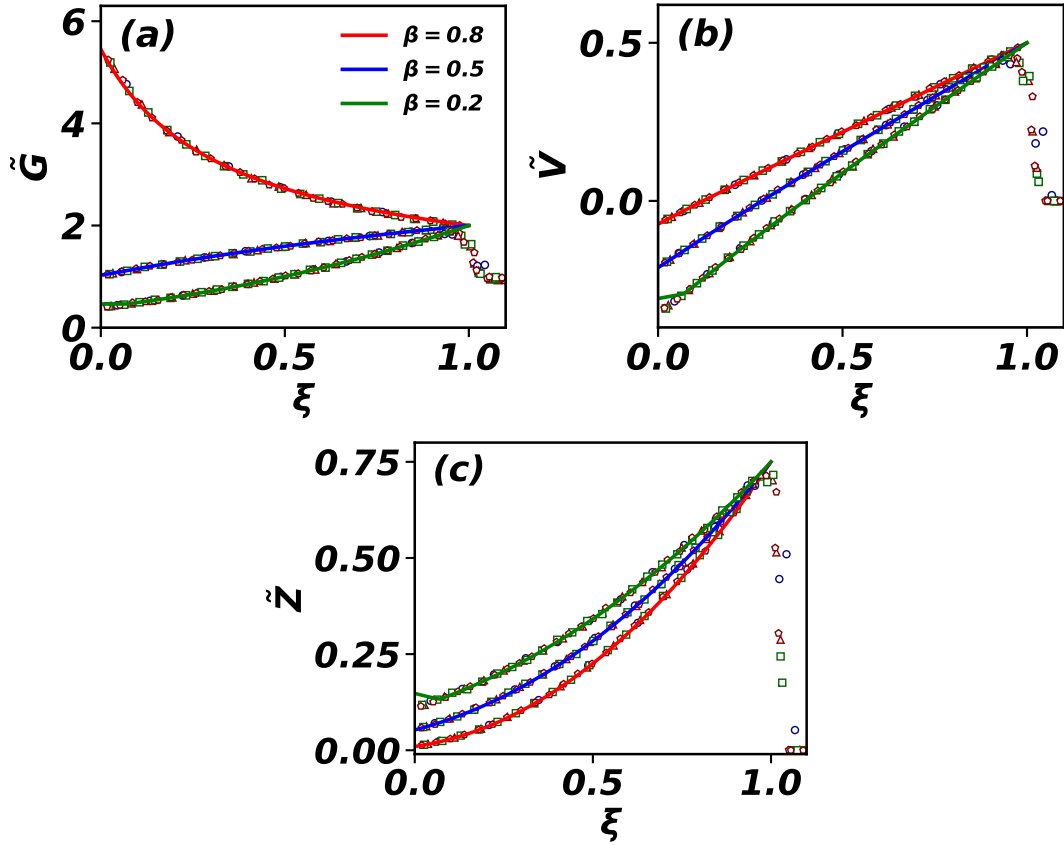


Figure 6.5: The variation of scaling functions: (a) density  $\tilde{G}$ , (b) velocity  $\tilde{V}$ , and (c) temperature  $\tilde{Z}$  with rescaled distance  $\xi$  for  $\beta = 0.2, 0.5$ , and  $0.8$ . The symbols represent the EDMD data at four different times,  $t = 5000, 10000, 15000$ , and  $20000$ , while the solid colored lines represent the self-similar solution of the Euler equation (see Eqs. (6.15-6.17)). The rescaled thermodynamic profiles obtained from the EDMD simulations show excellent agreement with the numerical solution of the Euler equation.

for  $x \geq 0$ , where the initial density distribution of the medium decays as a power law with radial distance,  $\rho(x) = \rho_0|x|^{-\beta}$ , with  $0 < \beta < 1$  in one dimension. At long times, the entire energy is reflected back into the vacuum. This results in the energy of the inhomogeneous medium decaying over time as a power law,  $E(t) \sim t^{-\delta_s}$ .

The splash problem does not allow for determination of all the exponents using scaling analysis. Instead, we derived the values of  $\delta_s$  and other thermodynamic quantities for different  $\beta$  by solving the Euler equation using self-similarity of the second kind. The solutions were obtained by simplifying the Euler equation's differential terms and identifying the common roots of the numerator and denominator. For the scaling functions to be single-valued in terms of the rescaled distance, the solution curves for different values of  $\beta$  must pass through these common roots.

We validated the numerical values of  $\delta_s$  through event-driven molecular simulations in one dimension. In our simulations, we used bi-disperse particles with masses 1 and 2 units, arranged alternately to prevent the system from becoming integrable, as would occur if all particles had the same mass. The simulation results confirm that the energy of the inhomogeneous medium decays as  $E(t) \sim t^{-\delta_s}$ , with  $\delta_s$  matching the value predicted by the Euler equation for the corresponding  $\beta$ . Additionally, the radius of the shock front followed the dimensional analysis result,  $R(t) \sim t^{(2-\delta_s)/(3-\beta)}$ . We observed a growth in the density peak in the vacuum, which leads to particle confinement between two density peaks: one in the vacuum and the other at the shock front. This results in a much slower decay of the energy, eventually becoming nearly constant. We demonstrated that the thermodynamic quantities derived from the Euler equation closely match the simulation data, and found that the scaling functions in the splash problem exhibit a power-law behaviour near the center, akin to the behaviour observed in the blast problem in an inhomogeneous medium [94].

# 7

## Shock propagation in a driven hard sphere gas : molecular dynamics simulations and hydrodynamics

### Related Publication :

This chapter is based on the following publication [96]:

Shock propagation in a driven hard sphere gas: molecular dynamics simulations and hydrodynamics,

**Amit Kumar** and R. Rajesh, *arXiv preprint arXiv:2409.12086*, 2025.



### 7.1 Introduction

The studies discussed in the previous chapters focus solely on the dependence of thermodynamic quantities on the spatial mass distributions of the surrounding gas.

Another key aspect to consider is the mechanism of energy input into the gas. A closely related problem is that of shocks that are generated when there is a continuous input of energy in the system by an external source. Now, unlike the problem of single impact as discussed in earlier chapters, the system is driven away from equilibrium due to the constant energy current. This problem has relevance for the study of the motion of interstellar gas due to the effect continuous energy injection by the stellar wind [29, 30]. Let the source be such that energy increases as  $E(t) = E_0 t^\delta$ , where  $E_0$  and  $\delta$  are positive constants. From dimensional analysis, one obtains that the radius of shock front grows as  $R(t) \sim (E_0/\rho_0)^{1/d+2} t^{(2+\delta)/(d+2)}$ , in  $d$ -dimensions [13]. The TvNS solution for the single impact can now be generalised to  $\delta \neq 0$ .

Self-similar solutions for driven shocks have been studied for two types of driving mechanisms, which we refer to as central driving and uniform driving. In central driving, energy is continuously input in a fixed localised region around the shock center, leading to the rate of change of local entropy being zero away from the shock center [13, 102]. In uniform driving, energy is continuously input uniformly in the region between the shock center and the shock front (which is moving with time) [13, 102]. In the central driving, the self-similar solution of the Euler equation becomes singular at a finite scaled radius, and thus is unable to describe the hydrodynamics of the shock in the complete region from the shock center to the shock front. On the other hand, for the uniform driving, there exists a self-similar solution of the Euler equation for the entire region of the shock [13]. The exact self similar solution of the Euler equation for the uniform driving of an ideal gas in three dimensions was found by Dokuchaev [13].

In this chapter, we focus on the hydrodynamics of the shocks in the presence of an energy source. Given that the correct description of the shock due to a single impact required dissipation terms (Navier-Stokes equations), it is highly likely that

the driven shocks also are not described by the Euler equation specially close to the shock center. In addition, it is not even clear whether the Navier-Stokes equations can describe the different thermodynamic quantities for the driven shock, given that the system is far from equilibrium. Also, for central driving, the Euler equation is manifestly insufficient to describe the hydrodynamics, and we ask whether including the dissipation terms to the Euler equation can regularise the singular behaviour seen in the self-similar solution. To address these issues, we study the problem of driven shocks using different approaches namely Euler equation, Navier-Stokes equations, and EDMD simulations for hard sphere gas in two and three dimensions. In two dimensions, we study both central as well as uniform driving, while in three dimensions, we restrict ourselves to only central driving.

The remainder of this chapter is organised as follows. In Sec. 7.2, we review the exact solution of Euler equation for driven shocks in an ideal gas, and find the asymptotic behaviour of different scaling functions. In Sec. 7.2.4, we modify the equation of state from ideal to virial equation of state to account for steric effects. We then numerically solve the Euler equation and quantify the effect of excluded volume on the solution. In Sec. 7.3 we numerically study the driven shock in a hard sphere gas using EDMD simulations, and verify the correctness of the simulations by benchmarking the known behaviour of physical quantities. In Sec. 7.4, we provide the direct numerical solution of the Navier-Stokes equations for virial equation of state, and do a parametric study to understand the effect of the dissipation terms on the scaling functions. In Sec. 7.5, we compare all the results obtained from the theory, EDMD, and DNS of NSE for hard sphere gas. We show that for central driving, the solution for NSE has self-similar solution that spans the entire shock, overcoming the singular behaviour that the solution to the Euler equation suffers from. For both driving, we show that the data from EDMD is well described by NSE. We conclude with a summary and discussion in Sec. 7.6. The content of this chapter is published in Ref. [96].

---

## 7.2 Review of Euler Equation for Driven Shock

In this section, we summarise the Euler equation describing the macroscopic dynamics of a driven shock. Consider a gas at rest having uniform density  $\rho_0$ , and hence zero pressure and zero temperature everywhere. Energy is isotropically and continuously injected at one point (taken to be the origin) such that the total energy increases with time  $t$  as  $E(t) = E_0 t^\delta$ ,  $\delta \geq 0$ . The driving generates a spherically symmetric shock which expands self similarly in time into the ambient gas. We define the shock front as the surface of discontinuity which separates the moving gas from the ambient stationary gas. A shock is said to be strong if  $p_1/\rho_1 \gg p_0/\rho_0$ , where  $p$  is the pressure,  $\rho$  is the mass density, and subscripts 1 and 0 indicate the quantities just behind and front of the shock respectively. Since  $p_0 = 0$  for an initial stationary gas, the shock is always strong.

The scaling of the radius of shock front,  $R(t)$ , with time  $t$ , is uniquely determined by dimensional analysis [1, 11, 73], and in  $d$ -dimensions is

$$R(t) \sim \left( \frac{E_0}{\rho_0} \right)^{1/(2+d)} t^{(2+\delta)/(2+d)}. \quad (7.1)$$

The macroscopic state of the gas at time  $t$  and position  $\vec{r}$  is described in terms of the following fields: density  $\rho(\vec{r}, t)$ , velocity  $\vec{v}(\vec{r}, t)$ , temperature  $T(\vec{r}, t)$ , and pressure  $p(\vec{r}, t)$ . Due to the spherical symmetry, the thermodynamic quantities depend only on radial distance  $r$ , and the velocity is radial,

$$\vec{v}(\vec{r}, t) = v(r, t) \hat{r}. \quad (7.2)$$

The continuity equations of locally conserved quantities, mass, momentum, and the energy, give the evolution of the fields. In the scaling limit,  $r \rightarrow \infty$ ,  $t \rightarrow \infty$ , such that  $rt^{-(2+\delta)/(2+d)}$  remains constant, the contribution of heat conduction and viscosity become negligible and the hydrodynamics is governed by the Euler equation. The



continuity equations for mass and momentum along radial direction in  $d$ -dimensional spherical polar coordinates is given by [1–3, 11, 13]

$$\partial_t \rho + \partial_r(\rho v) + \frac{(d-1)\rho v}{r} = 0, \quad (7.3)$$

$$\partial_t v + v \partial_r v + \frac{1}{\rho} \partial_r p = 0, \quad (7.4)$$

In general, there can be multiple ways to drive the system, such as central driving or uniform driving. Regardless of the specific driving mechanism, macroscopic quantities like the radius  $R(t)$ , total energy  $E(t)$ , and total radial momentum  $M(t)$  are expected to exhibit the same long-time scaling behavior. However, the rescaled thermodynamic quantities depend sensitively on the nature of the driving, and their evolution must be described by appropriate continuity equations.

For any driven system, the entropy production rate  $\dot{s}$  cannot vanish at the location of energy injection. This is because the driving source continuously supplies energy, pushing the system out of equilibrium and thus generating local entropy.

Both systems — central driving and uniform driving — can be described either via the continuity equation for entropy or for energy. However, in each case, the governing equations must properly account for the distribution and effect of the energy sources. When using the entropy continuity framework, the entropy production rate  $\dot{s}$  should take the form of a Dirac delta function centered at  $r = 0$  for the case of central driving, implying that  $\dot{s} \approx 0$  far from the origin. In contrast, for uniform driving,  $\dot{s} \neq 0$  throughout the entire domain, reflecting spatially distributed energy input. In such cases,  $\dot{s}$  must be correctly evaluated at each point to accurately describe the system.

Alternatively, when the system is described using the energy continuity equation, the driving source in the central driving case appears as a Dirac delta function at  $r = 0$ , and its effect becomes negligible at large distances. For uniform driving, the energy injection corresponds to an infinite number of Dirac delta functions continuously

---

distributed over the entire driven region  $0 \leq r \leq R(t)$ , capturing the uniform nature of the energy input.

In the following sections, we present the complete set of governing equations — in addition to Eqs. (7.3) and (7.4) — that are required to fully describe these driven systems.

### 7.2.1 Continuity equation of energy for uniform driving

For uniform driving, it is more appropriate to describe the system using the continuity equation for energy. We follow the derivation presented in Refs. [1, 13].

Consider a spherical surface at radial distance  $r$ , expanding in a self-similar manner with the shock front. Define the self-similar variable as  $\xi' = r/R(t)$ . The velocity of this surface is given by

$$v_n(r) = \dot{r} = U \frac{r}{R(t)}, \quad (7.5)$$

where  $U = \dot{R}(t)$  is the velocity of the shock front. Suppose that, during a time interval  $\Delta t$ , this surface moves a radial distance  $\Delta r = v_n \Delta t$ . The energy contained inside this shell is

$$E_{\text{in}} = \rho \left( \epsilon + \frac{v^2}{2} \right) S_d r^{d-1} v_n \Delta t, \quad (7.6)$$

where  $S_d$  is the surface area of a unit sphere in  $d$  dimensions. The total energy flux leaving the shell due to particle motion is

$$E_{\text{out}} = \rho \left( \epsilon + \frac{p}{\rho} + \frac{v^2}{2} \right) S_d r^{d-1} v \Delta t. \quad (7.7)$$

The energy injected into the shell by the driving source is

$$E_{\text{source}} = \rho T \dot{s} \Delta t S_d r^{d-1} v_n \Delta t. \quad (7.8)$$

By applying energy conservation within the shell, we write

$$E_{\text{out}} = E_{\text{in}} + E_{\text{source}}. \quad (7.9)$$

Substituting the expressions, we get

$$\rho v \left( \epsilon + \frac{p}{\rho} + \frac{v^2}{2} \right) S_d r^{d-1} \Delta t = \rho v_n \left( \epsilon + \frac{v^2}{2} \right) S_d r^{d-1} \Delta t + \rho T \dot{s} S_d r^{d-1} v_n \Delta t^2. \quad (7.10)$$

In the limit  $\Delta t \rightarrow 0$ , the second term on the right-hand side becomes negligible compared to the other terms [13]. Neglecting this term leads to the final form of the energy continuity equation:

$$v \left( \epsilon + \frac{p}{\rho} + \frac{v^2}{2} \right) = \frac{U r}{R(t)} \left( \epsilon + \frac{v^2}{2} \right), \quad (7.11)$$

where  $\epsilon$  is the internal energy per unit volume. For any gas,  $\epsilon = T/(\gamma - 1)$ , with  $\gamma$  being the adiabatic index.

### 7.2.2 Continuity equation of entropy for central driving

For central driving, it is convenient to analyze the system using the continuity equation for entropy:

$$\dot{s} = \partial_t s + v \partial_r s, \quad (7.12)$$

where the local entropy is defined as  $s = \frac{1}{\gamma-1} \log \left( \frac{p}{\rho^\gamma} \right)$ . For this case, the flow can be assumed to be adiabatic away from the shock center, implying  $\dot{s} = 0$  for  $\vec{r} \neq 0$ .

### 7.2.3 Non-dimensional continuity equations for ideal gas

Equations (7.3-7.4) and Eq. (7.11) together describe the driven shock problem with uniform driving [13], while Eqs. (7.3-7.4) and Eq. (7.12) with  $\dot{s} = 0$  together describe the driven shock problem with the central driving [102].

Assuming local thermal equilibrium, the local pressure  $p$  is related to the local temperature  $T$  and local density  $\rho$  through an equation of state (EOS), reducing the number of variables by one. A general EOS can be written as

$$p = k_B \rho T \mathbb{Z}(\rho), \quad (7.13)$$

where  $\mathbb{Z}(\rho)$  is known as the compressibility factor of the EOS.

Across the shock front these thermodynamic quantities become discontinuous. The values of these quantities ahead and behind the shock front are related by the Rankine-Hugoniot boundary conditions [1, 3]:

$$\rho_1 = \left[ 1 + \frac{2}{(\gamma - 1)\mathbb{Z}(\rho_1)} \right] \rho_0, \quad (7.14)$$

$$v_1 = \frac{2U}{2 + (\gamma - 1)\mathbb{Z}(\rho_1)}, \quad (7.15)$$

$$p_1 = \frac{2\rho_0 U^2}{2 + (\gamma - 1)\mathbb{Z}(\rho_1)}. \quad (7.16)$$

$\gamma = 1 + 2/d$  is the adiabatic constant for mono-atomic gas in  $d$ -dimensions.

It should also be noted that total energy  $E(t)$  of the gas at time  $t$  should be equal to  $E_0 t^\delta$ , i.e.

$$E_0 t^\delta = \int_0^{R(t)} \left( \frac{\rho v^2}{2} + \frac{\rho T}{\gamma - 1} \right) S_d r^{d-1} dr, \quad (7.17)$$

where  $S_d = 2\pi^{d/2}/\Gamma(d/2)$  is the surface area of  $d$ -dimensional sphere of unit radius. The continuity equations (7.3)–(7.12) are first order partial differential equations in both time and distance. These equations can be converted into ordinary differential

---

equations using self similar solutions. We define dimensionless distance  $\xi$  and non-dimensionalised scaling functions  $\tilde{R}, \tilde{u}, \tilde{T}, \tilde{P}$  corresponding to density  $\rho$ , velocity  $u$ , temperature  $T$ , and pressure  $p$  respectively as

$$\xi = r \left( \frac{E_0}{\rho_0} \right)^{-1/(2+d)} t^{-(2+\delta)/(2+d)}, \quad (7.18)$$

$$\rho(r, t) = \rho_0 \tilde{R}(\xi), \quad (7.19)$$

$$v(r, t) = \frac{r}{t} \tilde{u}(\xi), \quad (7.20)$$

$$T(r, t) = \frac{r^2}{t^2} \tilde{T}(\xi), \quad (7.21)$$

$$p(r, t) = \frac{\rho_0 r^2}{t^2} \tilde{P}(\xi). \quad (7.22)$$

We now specialize the solution to the ideal gas for which an exact solution may be found for the case of uniform driving case. For ideal gas  $\mathbb{Z}(\rho) = 1$ , and the equation of state (Eq. (7.13)) implies that,

$$\tilde{P} = \tilde{R} \tilde{T}. \quad (7.23)$$

The continuity equations (7.3-7.11) and Eq. (7.12) with  $\dot{s} = 0$ , in terms of the scaling functions, reduce to

$$(\alpha - \tilde{u}) \frac{d \log \tilde{R}}{d \log \xi} - \frac{d \tilde{u}}{d \log \xi} = d \tilde{u}, \quad (7.24)$$

$$(\tilde{u} - \alpha) \frac{d \tilde{u}}{d \log \xi} + \tilde{T} \frac{d \log \tilde{R}}{d \log \xi} + \frac{d \tilde{T}}{d \log \xi} + \tilde{u}[\tilde{u} - 1] + 2 \tilde{T} = 0, \quad (7.25)$$

$$\tilde{T} = \frac{\tilde{u}^2 (\alpha - \tilde{u}) (\gamma - 1)}{2(\gamma \tilde{u} - \alpha)}, \quad (7.26)$$

$$(\tilde{u} - \alpha) \frac{d}{d \log \xi} \log \left( \frac{\tilde{T}}{\tilde{R}^{\gamma-1}} \right) + 2(\tilde{u} - 1) = 0, \quad (7.27)$$

respectively, where  $\alpha = (2 + \delta)/(2 + d)$ , while the Rankine-Hugoniot boundary conditions reduce to

$$\tilde{R}(\xi = \xi_f) = \frac{\gamma + 1}{\gamma - 1}, \quad (7.28)$$

$$\tilde{u}(\xi = \xi_f) = \frac{2\alpha}{\gamma + 1}, \quad (7.29)$$

$$\tilde{T}(\xi = \xi_f) = \frac{2\alpha^2(\gamma - 1)}{(\gamma + 1)^2}, \quad (7.30)$$

where  $\xi_f$  is the location of the shock front. For uniform driving, given the boundary conditions (7.28)–(7.30) at  $\xi_f$ , the differential equations (7.24)–(7.26) may be integrated to obtain the scaling functions. However,  $\xi_f$  remains indeterminate. The value of  $\xi_f$  is uniquely fixed from the non-dimensionalised form of Eq. (7.17),

$$S_d \int_0^{\xi_f} \left( \frac{\tilde{R}\tilde{u}^2}{2} + \frac{\tilde{R}\tilde{T}}{\gamma - 1} \right) \xi^{d+1} d\xi = 1. \quad (7.31)$$

An analytical solution of Eqs (7.24)–(7.26) with boundary conditions given in Eqs. (7.28)–(7.30) is possible [13]. For the completeness of the results, as obtained in Ref. [13] in three dimensions, we provide the analytical solution of ordinary differential Eqs. (7.24)–(7.26) satisfying the Rankine-Hugoniot boundary conditions (see Eqs. (7.28)–(7.30)) for non-dimensionalised scaling functions  $\tilde{R}$ ,  $\tilde{u}$ ,  $\tilde{T}$ , and  $\tilde{P}$  as defined in Eqs. (7.18)–(7.22). On further simplifying the Eqs. (7.24)–(7.26) for  $d\tilde{u}/d\log\xi$  and  $d\log\tilde{R}/d\log\xi$ , we obtain

$$\frac{d\tilde{u}}{d\log\xi} = \frac{\tilde{u}(\gamma\tilde{u} - \alpha)[10\alpha^2 + 2\tilde{u}[(2+\delta)(\tilde{u} - 2\alpha) + \gamma\alpha(\delta - 3)] + 3\tilde{u}^2(2+\delta)(\gamma - 1)]}{(2+\delta)[2\alpha^3 - 2\alpha\tilde{u}(\gamma + 2) + \alpha\tilde{u}^2(3 + 2\gamma + \gamma^2) - 2\gamma\tilde{u}^3 - \tilde{u}^2(\gamma - 1)(\gamma\tilde{u} - \alpha)]}, \quad (7.32)$$

$$\begin{aligned} \frac{d\log\tilde{R}}{d\log\xi} = & \frac{3\tilde{u}(2+\delta)[2\alpha^3 - 2\alpha^2\tilde{u}(\gamma + 2) + \alpha\tilde{u}^2(3 + 2\gamma + \gamma^2)]}{(2+\delta)(\alpha - \tilde{u})[2\alpha^3 - 2\alpha^2\tilde{u}(\gamma + 2) + \alpha\tilde{u}^2(3 + 2\gamma + \gamma^2) - 2\gamma\tilde{u}^3 - \tilde{u}^2(\gamma - 1)(\gamma\tilde{u} - \alpha)]} + \\ & \frac{2\tilde{u}(\gamma\tilde{u} - \alpha)[5\alpha^2 + \tilde{u}[(2+\delta)(\tilde{u} - 2\alpha) + \gamma\alpha(\delta - 3)]]}{(2+\delta)(\alpha - \tilde{u})[2\alpha^3 - 2\alpha^2\tilde{u}(\gamma + 2) + \alpha\tilde{u}^2(3 + 2\gamma + \gamma^2) - 2\gamma\tilde{u}^3 - \tilde{u}^2(\gamma - 1)(\gamma\tilde{u} - \alpha)]}, \end{aligned} \quad (7.33)$$

$$\tilde{T} = \frac{\tilde{u}^2(\alpha - \tilde{u})(\gamma - 1)}{2(\gamma\tilde{u} - \alpha)}. \quad (7.34)$$

The above ordinary differential equations can be solved analytically. The solution depends on the sign of the parameter  $a_1 = (\gamma - 2)^2(\delta^2 + 9) - (6\gamma^2 + 26\gamma - 26)\delta$ .

When  $a_1 \geq 0$ , we find

$$\begin{aligned} \tilde{R}(\tilde{u}) = & \frac{\alpha b_1}{\alpha - \tilde{u}} (f_2(\tilde{u}))^{a_8} \left( \frac{\gamma\tilde{u} - \alpha}{\alpha(\gamma - 1)} \right)^{a_9} \exp \left( \frac{a_7}{\sqrt{a_1}} \left[ \tanh^{-1} \left( \frac{f_1(\tilde{u})}{\sqrt{a_1}} \right) - \tanh^{-1} \left( \frac{a_5}{\sqrt{a_1}} \right) \right] \right), \end{aligned} \quad (7.35)$$

$$\begin{aligned} \left( \frac{10}{2+\delta} \right) \log \left( \frac{\xi(\tilde{u})}{\xi_f} \right) = & \frac{a_2}{\sqrt{a_1}} \left[ \tanh^{-1} \left( \frac{a_5}{\sqrt{a_1}} \right) - \tanh^{-1} \left( \frac{f_1(\tilde{u})}{\sqrt{a_1}} \right) \right] + a_3 \log \left( \frac{\gamma\tilde{u} - \alpha}{\alpha(\gamma - 1)} \right) \\ & + \log \left( \frac{(\alpha^2 f_2(\tilde{u}))^{a_4}}{\tilde{u}^2} \right) + b_2. \end{aligned} \quad (7.36)$$

On the other hand, when  $a_1 < 0$ , we obtain

$$\begin{aligned} \tilde{R}(\tilde{u}) = & \frac{\alpha b_1}{\alpha - \tilde{u}} (f_2(\tilde{u}))^{a_8} \left( \frac{\gamma\tilde{u} - \alpha}{\alpha(\gamma - 1)} \right)^{a_9} \exp \left( \frac{a_7}{\sqrt{-a_1}} \left[ \tan^{-1} \left( \frac{a_5}{\sqrt{-a_1}} \right) - \tan^{-1} \left( \frac{f_1(\tilde{u})}{\sqrt{-a_1}} \right) \right] \right), \end{aligned} \quad (7.37)$$

$$\begin{aligned} \left( \frac{10}{2+\delta} \right) \log \left( \frac{\xi(\tilde{u})}{\xi_f} \right) = & \frac{a_2}{\sqrt{-a_1}} \left[ \tan^{-1} \left( \frac{f_1(\tilde{u})}{\sqrt{-a_1}} \right) - \tan^{-1} \left( \frac{a_5}{\sqrt{-a_1}} \right) \right] \\ & + a_3 \log \left( \frac{\gamma\tilde{u} - \alpha}{\alpha(\gamma - 1)} \right) + \log \left( \frac{(\alpha^2 f_2(\tilde{u}))^{a_4}}{\tilde{u}^2} \right) + b_2, \end{aligned} \quad (7.38)$$

where,

$$a_2 = \frac{2 \left( (6\gamma^3 - 11\gamma^2 - 3\gamma + 2) \delta^2 + (19\gamma^3 + 16\gamma^2 + 33\gamma - 32) \delta + 39\gamma^3 - 99\gamma^2 + 78\gamma - 72 \right)}{(2\gamma + 1)(3\gamma - 1)(\delta + 2)}, \quad (7.39)$$

$$a_3 = \frac{10(\gamma - 1)}{(2\gamma + 1)(\delta + 2)}, \quad (7.40)$$

$$a_4 = \frac{(6\gamma^2 + \gamma - 1) \delta - 13\gamma^2 + 7\gamma - 12}{(2\gamma + 1)(3\gamma - 1)(\delta + 2)}, \quad (7.41)$$

$$a_5 = \frac{(\gamma^2 + 5\gamma - 4) \delta - 3\gamma^2 + 5\gamma - 8}{\gamma + 1}, \quad (7.42)$$

$$a_6 = \frac{2 \left( (2\gamma^2 + 4\gamma - 6) \delta - \gamma^2 + 8\gamma - 7 \right)}{(\gamma + 1)^2}, \quad (7.43)$$

$$a_7 = \frac{6(\gamma + 3) \left( (\gamma^2 + \gamma - 1) \delta - 3\gamma^2 + 2\gamma - 2 \right)}{(6\gamma^2 + \gamma - 1)}, \quad (7.44)$$

$$a_8 = \frac{3(\gamma^2 + 1)}{6\gamma^2 + \gamma - 1}, \quad (7.45)$$

$$a_9 = \frac{3}{2\gamma + 1}, \quad (7.46)$$

$$b_1 = (\gamma + 1)^{a_9} a_6^{-a_8}, \quad (7.47)$$

$$b_2 = a_3 \log(\gamma + 1) - a_4 \log(a_6) + 2 \log \left( \frac{2}{\gamma + 1} \right), \quad (7.48)$$

$$f_1(\tilde{u}) = (3\gamma - 1)(\delta + 2)\tilde{u}/\alpha + (\gamma - 2)\delta - 3\gamma - 4, \quad (7.49)$$

$$f_2(\tilde{u}) = (3\gamma - 1)(\delta + 2)\tilde{u}^2/\alpha^2 + 2((\gamma - 2)\delta - 3\gamma - 4)\tilde{u}/\alpha + 10. \quad (7.50)$$

We have checked for the correctness of the solution by checking that they match with the numerical solution of the differential equations. The value of  $\xi_f$  can be obtained by using the energy constraint  $E(t) = E_0 t^\delta$  [see Eq. (7.31)].

The exact solution of Euler Eqs. (7.24)–(7.26) can be obtained in general  $d$ -dimensions, and the behaviour of the thermodynamic quantities near the shock center ( $\xi \rightarrow 0$ ) may be derived. These results will be useful for comparison with



results from particle based simulations. We find that when  $\xi \rightarrow 0$ , then  $\tilde{u} \rightarrow \alpha/\gamma$ . The asymptotic behaviour of  $\tilde{R}$ ,  $\tilde{u}$ ,  $\tilde{T}$ , and  $\tilde{P}$  near  $\xi \rightarrow 0$  for uniform driving in  $d$ -dimensions is

$$\tilde{u} - \frac{\alpha}{\gamma} \sim \xi^{\frac{2\gamma+d-2}{\gamma-1}} \quad (7.51)$$

$$\tilde{R} \sim \xi^{\frac{d}{\gamma-1}} \quad (7.52)$$

$$\tilde{T} \sim \xi^{-\frac{2\gamma+d-2}{\gamma-1}}, \quad (7.53)$$

$$\tilde{P} \sim \xi^{-2}. \quad (7.54)$$

The exponents of the different non-dimensionalised thermodynamic quantities only depend on  $d$ , and are independent of  $\delta$ , while the exponent of  $\tilde{P}$  is a constant. Since the exponents are independent of  $\delta$ , the power law behaviour of thermodynamic quantities remain same as for the case for shocks arising from a single impact [16].

We check for the correctness of the asymptotic analysis for  $\xi \rightarrow 0$  by comparing them with the full exact solution in two dimensions (see Fig. 7.1), where the non-dimensionalised functions obtained from exact solution of Euler Eqs. (7.24)–(7.26) are shown for four different values of  $\delta = 0, 0.5, 1, 1.5$ . It is clear that the power laws followed by different thermodynamic quantities are independent of  $\delta$ , and their exponents are consistent with Eqs. (7.51)–(7.54). Also, we note that the exact solution with  $\delta = 0$  reproduces the TvNS solution.

We now consider the case of central driving (see Eqs. (7.24–7.25) and Eq. (7.27)). From the numerical results, it is evident that the self-similar solution does not extend over the entire disturbed region. This limitation may arise due to the vanishing of either the numerator or the denominator — or both — in any of the derivatives  $\frac{d \log \tilde{R}(\xi)}{d \log \xi}$ ,  $\frac{d \log \tilde{u}(\xi)}{d \log \xi}$ , or  $\frac{d \log \tilde{T}(\xi)}{d \log \xi}$  for  $\delta \neq 0$  within the interval  $\xi \in (0, \xi_f)$ .

Unlike the uniform driving case, the absence of a complete self-similar solution over the full interval implies that Eq. (7.31) cannot be integrated from  $\xi = 0$  to  $\xi = \xi_f$ , leaving  $\xi_f$  undetermined. Therefore, for illustrative purposes, we fix  $\xi_f = 1$ . In

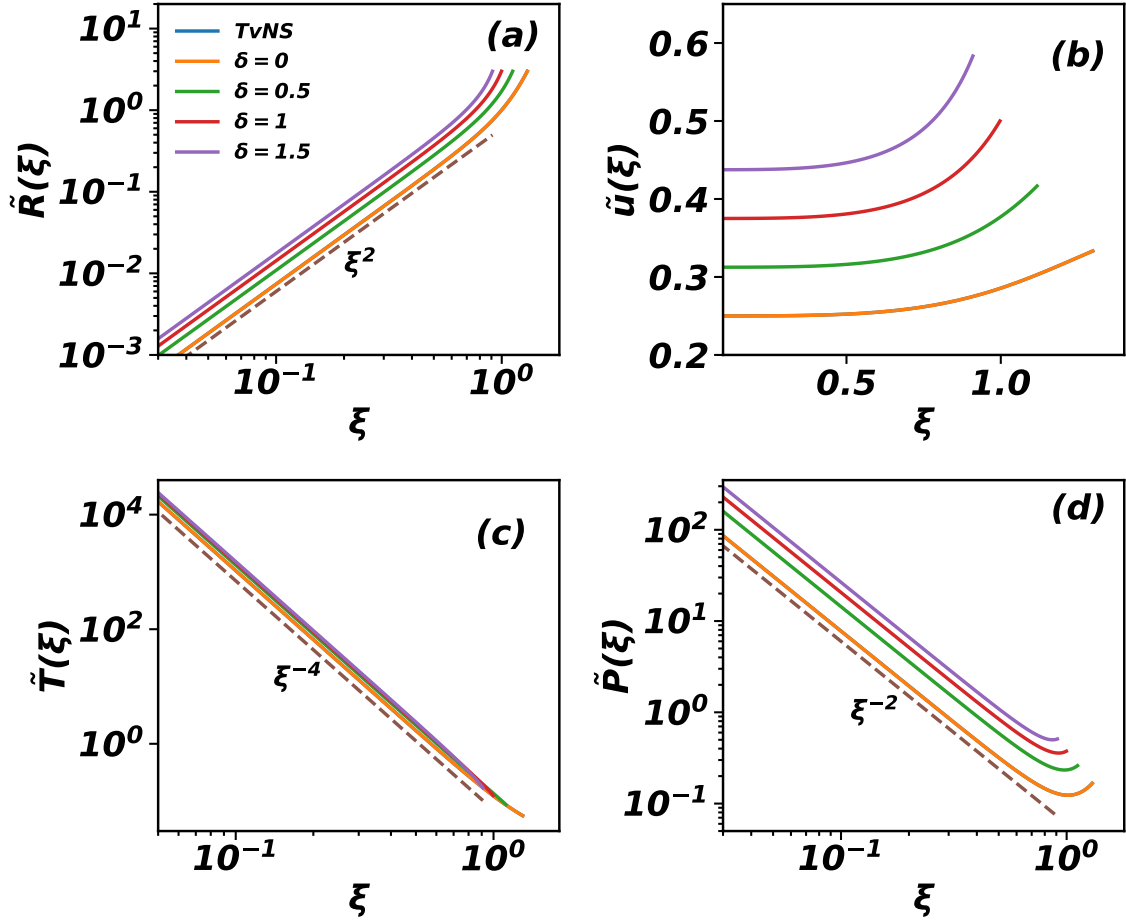


Figure 7.1: The exact solutions of the continuity equations for uniform driving (7.24)–(7.26) for the non-dimensionalised (a) density,  $\tilde{R}$ , (b) velocity,  $\tilde{u}$ , (c) temperature,  $\tilde{T}$ , and (d) pressure,  $\tilde{P}$  are compared with the asymptotic behaviour in two dimensions when  $\xi \rightarrow 0$  (see Eqs. (7.51)–(7.54)). The data are for four different values of  $\delta = 0, 0.5, 1, 1.5$ . The label  $TvNS$  refers to the solution of Euler equation with ideal EOS for a single impact.

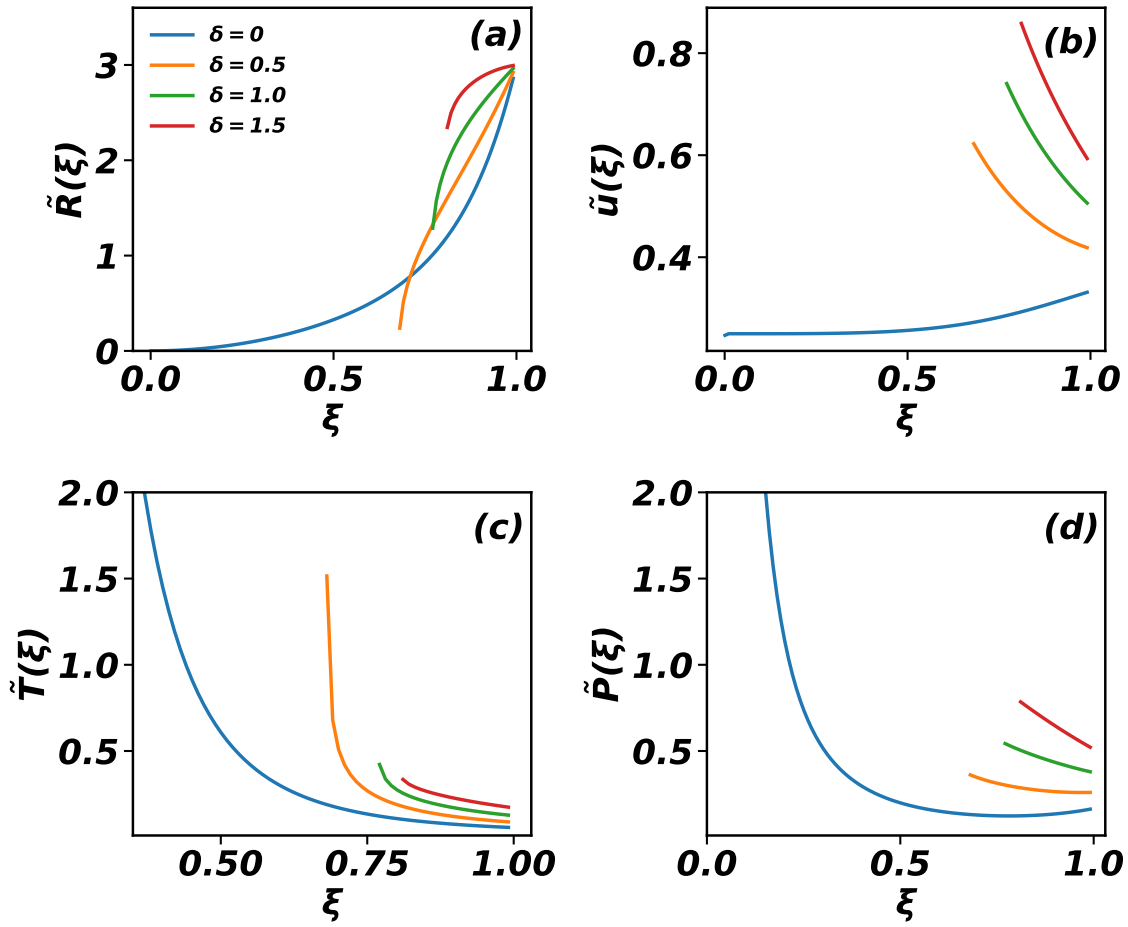


Figure 7.2: The numerical solution of the continuity equations for central driving [Eqs. (7.24–7.25) and Eq. (7.27)] for the non-dimensionalised (a) density,  $\tilde{R}$ , (b) velocity,  $\tilde{u}$ , (c) temperature,  $\tilde{T}$ , and (d) pressure,  $\tilde{P}$  for four different values of  $\delta = 0, 0.5, 1, 1.5$  in two dimensions. The solution curves for different  $\delta \neq 0$ , do not reach the origin and the range decreases with increasing  $\delta$ .

Fig. 7.2, we present the numerical solution of Eqs. (7.24–7.25) and Eq. (7.27) in two dimensions. For  $\delta \neq 0$ , the solution is valid only over a limited range of  $\xi$ , and this range shrinks as  $\delta$  increases.

To compare the results with EDMD simulations, we need to take into account steric effects. We describe below the details of how we incorporate excluded volume effects.

### 7.2.4 Euler equation for hard sphere gas

In a hard sphere gas, steric effects are important unlike in ideal gas. Thus, a more realistic EOS is needed to account for these effects. Virial EOS is the most common EOS for hard spheres, which take the following form,

$$p = \rho k_B T \left( 1 + \sum_{i=2}^{\infty} B_i \rho^{i-1} \right), \quad (7.55)$$

with compressibility factor,

$$\mathbb{Z}(\rho) = 1 + \sum_{i=2}^{\infty} B_i \rho^{i-1}. \quad (7.56)$$

where  $B_i$  denotes the  $i^{th}$  virial coefficient. We tabulate the known values of the virial coefficients [89] in Table 4.1. For hard-core gases,  $B_i$  does not depend on temperature and therefore only depend on the shape of the particles.

The Euler Eqs. (7.3)–(7.11) with the hard sphere gas EOS can be simplified in terms of scaling functions as

$$(\alpha - \tilde{u}) \frac{d \log \tilde{R}}{d \log \xi} - \frac{d \tilde{u}}{d \log \xi} = d \tilde{u}, \quad (7.57)$$

$$(\tilde{u} - \alpha) \xi \frac{dV}{d\xi} + \frac{d(\tilde{T}\mathbb{Z})}{d \log \xi} + \tilde{T}\mathbb{Z} \left( \frac{d \log \tilde{R}}{d \log \xi} + 2 \right) + \tilde{u}^2 - \tilde{u} = 0, \quad (7.58)$$

$$\tilde{T} = \frac{\tilde{u}^2(\alpha - \tilde{u})(\gamma - 1)}{2[(\gamma - 1)\tilde{u}\mathbb{Z} - (\alpha - \tilde{u})]}, \quad (7.59)$$

The Rankine-Hugoniot boundary conditions, Eqs. (7.14)–(7.16), for the hard sphere

Table 7.1: The numerical values of  $\xi_f$  for the hard sphere gas when virial EOS truncated at the  $i$ -th term, in three dimensions. The data for  $\xi_f$  for TvNS solution in two dimensions is taken from Ref. [17]. These data are for hard disk gas with diameter one,  $\gamma = 2$ , density 0.382.

$i$	$\xi_f(TvNS)$	$\xi_f(\delta = 0.5)$	$\xi_f(\delta = 1.0)$
2	1.5564	1.3426	1.1993
4	1.7286	1.4904	1.3308
6	1.7643	1.5202	1.3569
8	1.7719	1.5264	1.3623
10	1.7736	1.5277	1.3634

gas in terms of scaling functions reduce to

$$\tilde{R}(\xi_f) = 1 + \frac{2}{(\gamma - 1)\mathbb{Z}}, \quad (7.60)$$

$$\tilde{u}(\xi_f) = \frac{2\alpha}{2 + (\gamma - 1)\mathbb{Z}}, \quad (7.61)$$

$$\tilde{T}(\xi_f) = \frac{2\alpha^2(\gamma - 1)}{[2 + (\gamma - 1)\mathbb{Z}]^2}. \quad (7.62)$$

The ordinary differential equations (7.57)–(7.59) with the boundary conditions, Eqs. (7.60)–(7.62) can be solved numerically. As for the ideal gas, we find the value of  $\xi_f$  recursively by satisfying the energy constraint Eq. (7.31).

We now present the solution of Euler equation (see Eqs. (7.57)–(7.59)) only for the case of uniform driving in two dimensions. We obtain the numerical solution of Euler equation for hard disk gas with ambient density  $\rho_0 = 0.382$ , for different values of  $\delta$ , with virial EOS truncated at different terms. From the numerical solution, we calculated the values of  $\xi_f$  when virial EOS truncated at various terms. These values are tabulated in Table 7.1. We find that  $\xi_f$  does not change much between the equation of state truncated at the 8-th and 10-th virial terms for all values of  $\delta$ . We now examine the role of the truncation of the equation of state on the thermodynamics quantities. Figure 7.3 shows the variation of the scaling functions  $\tilde{R}$ ,  $\tilde{u}$ ,  $\tilde{T}$ , and  $\tilde{P}$  with  $\xi$  for hard spheres for  $\delta = 1$  in two dimension, when the

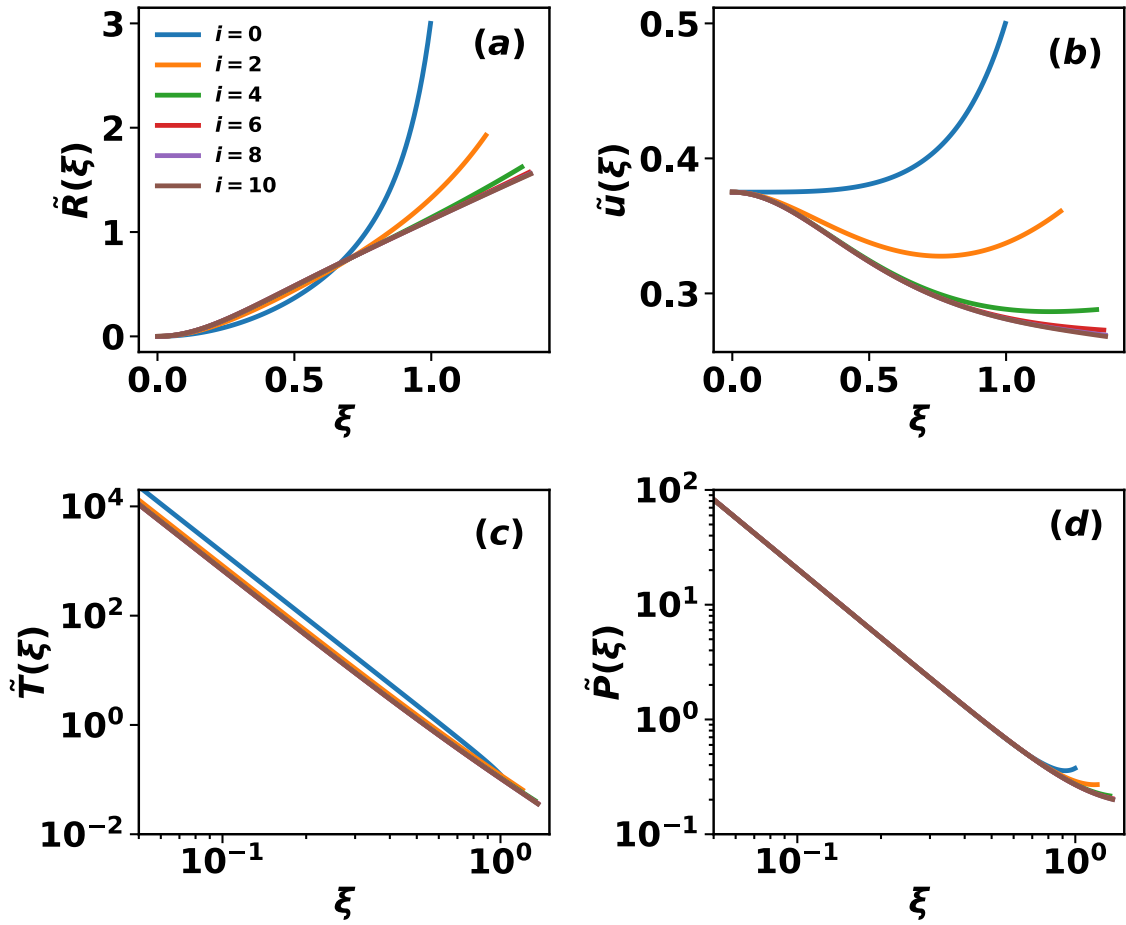


Figure 7.3: Non-dimensionalised thermodynamic quantities obtained by numerically solving Euler equation for uniform driving with virial equation of state (see Eqs. (7.57)–(7.59)) for  $\delta = 1$  when the virial EOS is truncated at  $i = 0, 2, 4, 6, 8$ , and 10-th term. The curves corresponding to  $i = 8, 10$  collapse on each other showing negligible truncation error at  $i = 10$ .  $i = 0$  represents the ideal EOS. The data are for ambient gas density  $\rho_0 = 0.382$  and  $d = 2$ .

virial EOS is truncated at  $i = 0, 2, 4, 6, 8, 10$ -th terms. We find that including the virial terms does affect the thermodynamic quantities, especially density and velocity. However, the data corresponding to  $i = 8, 10$  lie on top of each other showing negligible truncation error at  $i = 10$ . Thus, truncating virial EOS at  $i = 10$  is a good approximation to the actual EOS. We also point out that the exponents characterising the power-law behaviour do not depend on the truncation.

We now examine the role of  $\delta$ , the driving rate, on the thermodynamic quantities, within the Euler equation. For this, we keep the truncation of the virial expansion

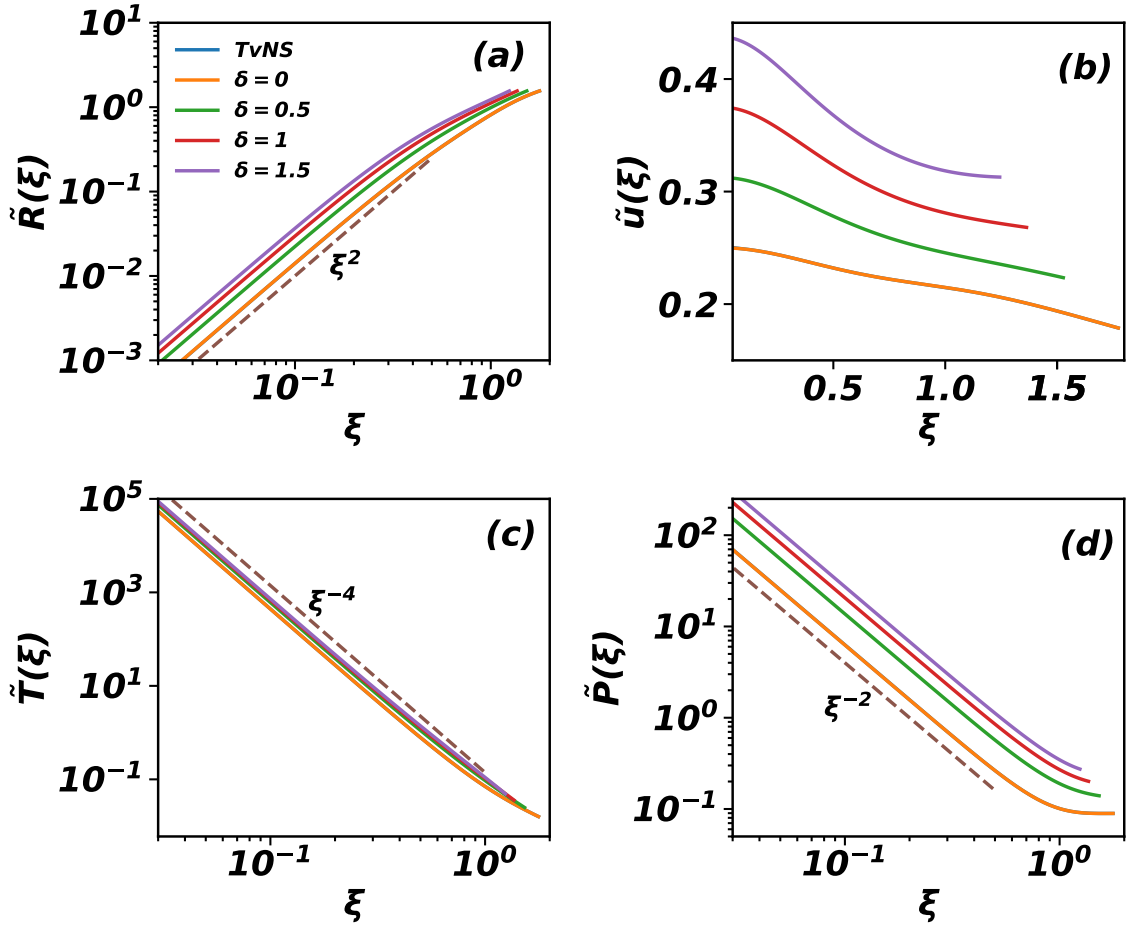


Figure 7.4: Power law behaviour of scaling functions for uniform driving obtained from numerical solution of Euler equation for hard spheres (see Eqs. (7.57)–(7.59)) for four different values of  $\delta = 0, 0.5, 1, 1.5$  in two dimensions. From the plot, power law behaviours of different scaling functions seem to be independent of the value of  $\delta$  and are the same as in the ideal gas case. The data shown here are for ambient gas density  $\rho_0 = 0.382$ , and for the virial EOS truncated at  $i = 10$ .

fixed at  $i = 10$  and vary  $\delta$ . We find that the exponents characterising the power law behaviour of the different thermodynamic quantities are independent of  $\delta$  (see Fig. 7.4), and hence same as that for the single impact with ideal gas EOS.

### 7.3 EDMD Simulations

In this section we briefly describe the details of the EDMD simulations of driven shock in a particle based model. The simulation results are for  $\delta = 1$  when energy is input at a constant rate, i.e.,  $E(t) = E_0 t$ .

We first describe the model. Consider a system of  $N$  identical hard spheres, labeled  $1, 2, \dots, N$ , distributed uniformly in space. The particles are initially at rest. Depending upon the driving scheme, we input the energy at a constant rate either at the origin (central driving) or throughout the disturbed region (uniform driving). The system evolves in time through momentum and energy conserving binary collisions between particles. All masses and distances are measured in terms of the particle mass  $m$  and diameter  $D$ , hence we set the mass and diameter of each particle to 1. Time is measured in terms of the inherent time scale  $(mD^2/E_0)^{1/3}$ .

In a binary collision, the normal component of the relative velocity is reversed while the tangential component remains unchanged. If  $\vec{v}_i, \vec{v}_j$  are the pre-collision velocities of colliding particles  $i, j$ , then their post-collision velocities  $\vec{v}'_i, \vec{v}'_j$  are given by

$$\vec{v}'_i = \vec{v}_i - (\hat{n} \cdot \vec{v}_{ij}) \hat{n}, \quad (7.63)$$

$$\vec{v}'_j = \vec{v}_j - (\hat{n} \cdot \vec{v}_{ji}) \hat{n}, \quad (7.64)$$

where  $\hat{n}$  is the unit vector along the line joining the centers of the two particles at the time of contact, and  $\vec{v}_{ij} = \vec{v}_i - \vec{v}_j$  is their relative velocity.

We model the continuous driving as follows. For central driving, consider a sphere of radius  $R_0$  centered about the origin or equivalently center of the simulation box. In each time interval  $\Delta t$ , a particle within the sphere of radius  $R_0$  is chosen at random and its velocity is modified to

$$\vec{v}'_i = \vec{v}_i + \vec{\eta}, \quad (7.65)$$

where the components of the noise  $\vec{\eta}$  are drawn from a uniform distribution between  $-\sqrt{dE_0\Delta t/6}$  to  $\sqrt{dE_0\Delta t/6}$ . For uniform driving, after each time interval  $\Delta t$ , a moving particle is randomly selected among all the moving particles at that time and its velocity is modified as Eq. (7.65).

With such a driving it is straightforward to show that total energy increases as

$$E(t) = E_0 t. \quad (7.66)$$


---



The simulations are done using the event driven molecular dynamics scheme where the system evolves from event to event, the events being collisions, driving and cell crossing [81]. Boundary effects are avoided by choosing the number of particles and box size such that the shock does not reach the boundary within the simulation time. The EDMD simulations were performed for  $N = 4 \times 10^7$  particles with mass density  $\rho_0 = 0.4013$ ,  $E_0 = 2.5 \times 10^{-6}$ , and  $R_0 = 15.0$  in three dimensions, and with  $N = 8 \times 10^6$  particles with mass density  $\rho_0 = 0.382$ ,  $E_0 = 3.3 \times 10^{-4}$ , and  $R_0 = 30.0$  in two dimensions.

We measure the radial density, velocity, temperature, and pressure in our simulation. We define density  $\rho(\vec{r}, t)$  and velocity  $v(\vec{r}, t)$  as local average of density and radial velocity at position  $\vec{r}$  and time  $t$ . Local temperature  $T(\vec{r}, t)$  is defined as the variance of local velocity. We measure local pressure for  $d$ -dimensional hard spheres [103] as

$$p = \rho T - \frac{\rho}{dN'\Delta t'} \sum_{\text{collisions}} \vec{r}_{ij} \cdot \vec{v}_{ij}, \quad (7.67)$$

where  $\vec{r}_{ij} = \vec{r}_i - \vec{r}_j$  is the distance between the colliding sphere,  $\Delta t'$  and  $N'$  are time interval and average number of particles belonging to a particular radial bin in which pressure is being measured.

The isotropic driving generates a spherically symmetric shock which grows radially outwards. To visualise the growing shock, in Fig. 7.5, we plot the  $x$ - and  $y$ - coordinates of all the particles lying between the planes  $z = -1$  and  $z = 1$  for the central driving case in three dimensions. It can be observed that there is a sharp boundary between the moving particles (red) and the stationary particles (green), and the shock front expands in time. Also, the density near the shock center is close to zero. Similar features are seen for the case of uniform driving also.

To benchmark our EDMD simulation, we first confirm that the total energy increases as  $E_0 t$ , as can be seen from Fig. 7.6(a). To further benchmark our simulations, we compare the power law growth of the radius of the shock and the radial momentum

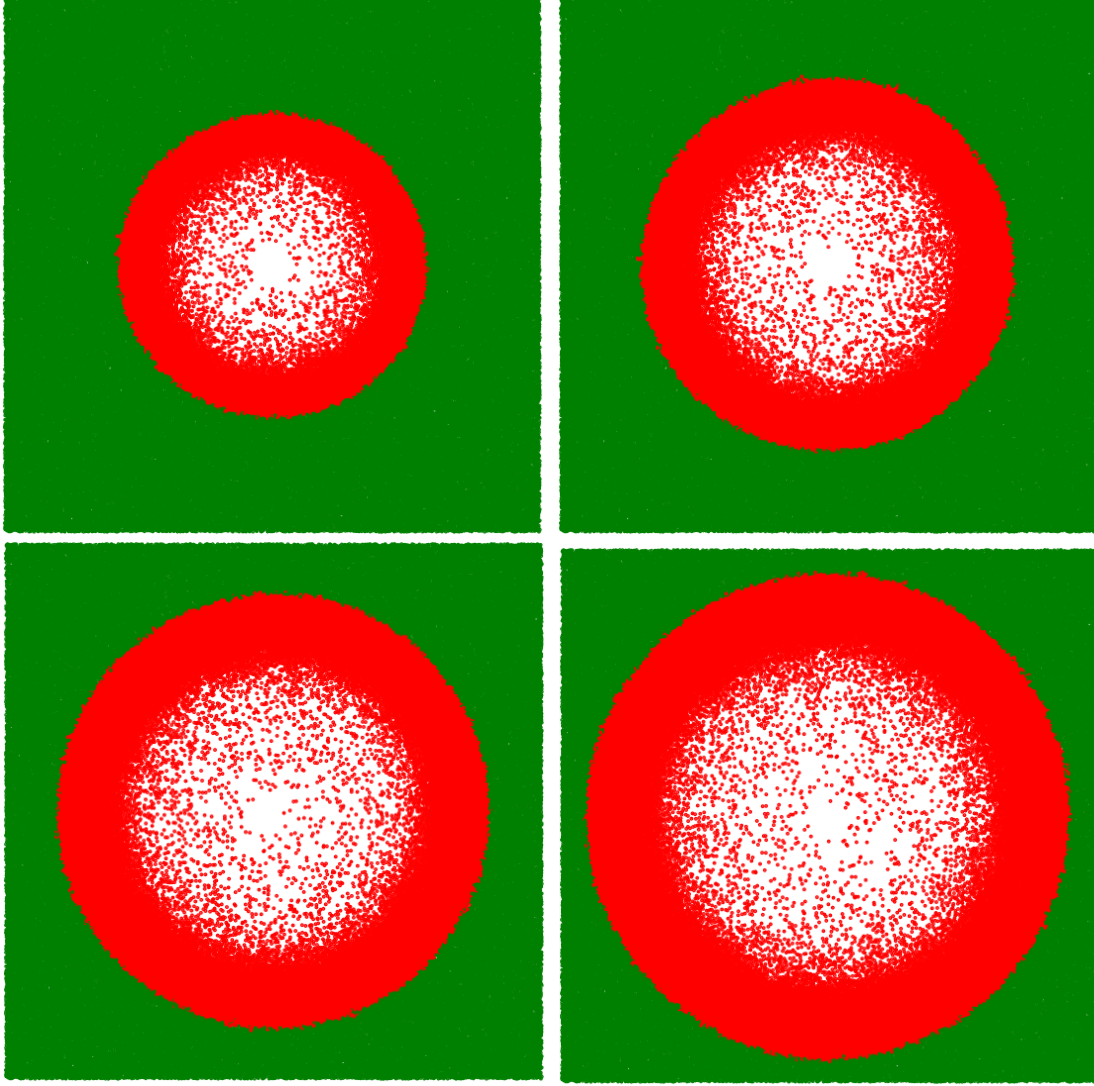


Figure 7.5: Snapshots of a cross-section of shock in the  $x$ - $y$  plane obtained by plotting the coordinates of only the particles with  $z$ -coordinates between  $-1$  to  $1$ . The data are for the times (a)  $t = 1357$ , (b)  $t = 1900$ , (c)  $t = 2443$ , (d)  $t = 2986$ . Stationary particles are coloured green while moving particles are coloured red. The data shown here are for ambient gas density  $\rho_0 = 0.4013$  and  $2 \times 10^7$  number of particles, and for central driving.

with time with known scaling laws. For the driven shock, in the scaling regime, the total radial momentum  $M(t)$ , and the radius of shock front  $R(t)$  should increase with time as

$$M(t) \sim t^{\alpha(d+1)-1}, \quad (7.68)$$

$$R(t) \sim t^\alpha. \quad (7.69)$$

The simulation results reproduce these power laws for large time, as can be seen in Fig. 7.6(b) and (c).  $R(t)$  is measured as the mean value of the radial distance of the moving particles, while  $M(t)$  is obtained as the cumulative radial velocity. For short times, there is a deviation from these power laws for the case of central driving. This is due to the radius of the shock being comparable to the driving scale  $R_0$ . The crossover time also gives us a measure of the time beyond which the scaling regime is reached. However, for uniform driving, the driving radius is  $R_0 = R(t)$ , so there is no such crossover and the power law behaviours are achieved from the start of the simulation itself.

Before a detailed analysis of the behaviour of the different thermodynamic quantities obtained from EDMD, we first describe the driven shock using Navier-Stokes equations i.e. inclusion of heat conduction and viscosity effects in Euler equation.

## 7.4 Navier-Stokes equations

In Euler equation, it was assumed that at long time, the contribution of the dissipation terms (heat conduction and viscosity) become negligible in the scaling limit. Since we anticipate the need for dissipation terms to describe the EDMD results, we now include the dissipation terms and describe how we numerically solve the resulting Navier-Stokes equations.

The continuity equations of mass, momentum, and energy, after including the dissipation terms, in the radial coordinates are given by [1, 3, 84, 85]

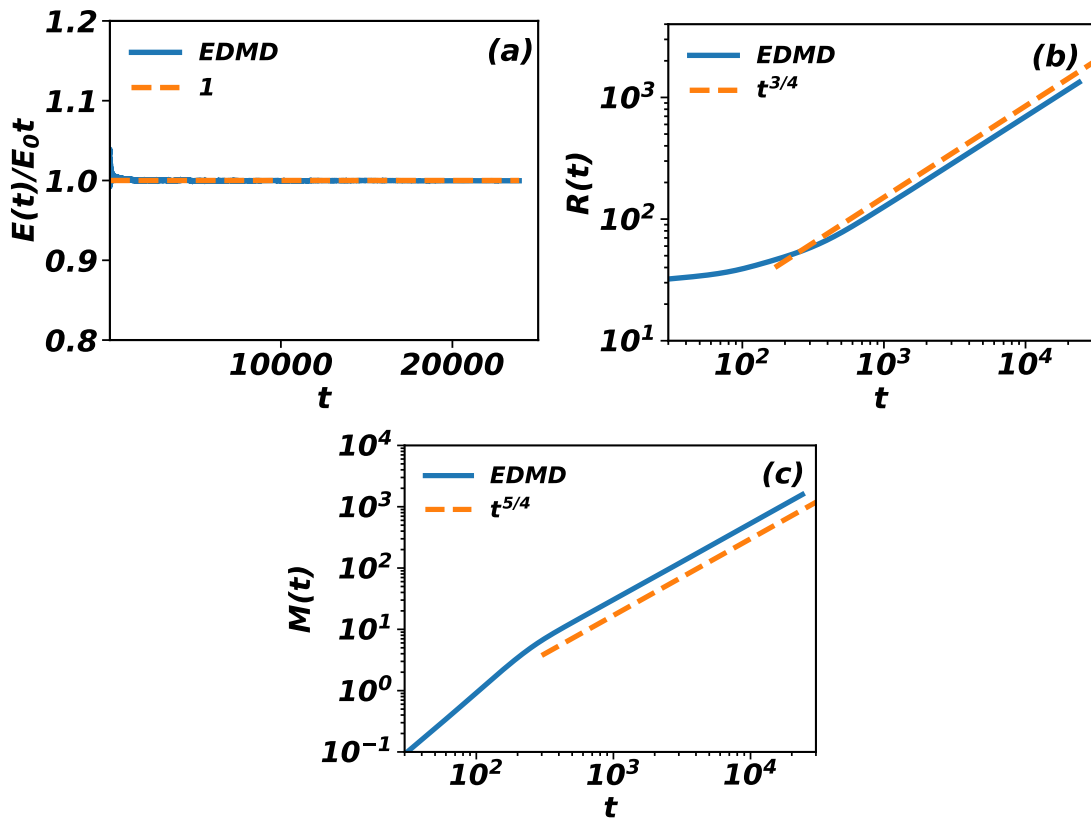


Figure 7.6: Power law growth of (a) total energy  $E(t) = E_0t$ , (b) radius of the shock front  $R(t) \sim t^{3/4}$ , and (c) total radial momentum  $M(t) \sim t^{5/4}$  of the system. Solid lines represent the results from EDMD, and dashed lines represent the respective power laws. The results are for the central driving in two dimensions with  $\delta = 1$ .

$$\partial_t \rho + \frac{1}{r^{d-1}} \partial_r (r^{d-1} \rho u) = 0, \quad (7.70)$$

$$\begin{aligned} \partial_t (\rho u) + \frac{1}{r^{d-1}} \partial_r [r^{d-1} \rho u^2] + \partial_r p &= \frac{1}{r^{d-1}} \partial_r (2\mu r^{d-1} \partial_r u) - \frac{2\mu(d-1)u}{r^2} \\ &+ \partial_r \left[ \left( \zeta - \frac{2}{d}\mu \right) \frac{1}{r^{d-1}} \partial_r (r^{d-1} u) \right], \end{aligned} \quad (7.71)$$

$$\begin{aligned} \partial_t \left( \frac{1}{2} \rho u^2 + \frac{\rho T}{\gamma - 1} \right) + \frac{1}{r^{d-1}} \partial_r \left( r^{d-1} \left[ \frac{1}{2} \rho u^2 + \frac{\rho T}{\gamma - 1} + p \right] u \right) &= \frac{1}{r^{d-1}} \partial_r (2r^{d-1} \mu u \partial_r u) \\ &+ \frac{1}{r^{d-1}} \partial_r \left( r^{d-1} u \left[ \zeta - \frac{2}{d}\mu \right] \frac{1}{r^{d-1}} \partial_r (r^{d-1} u) \right) + \frac{1}{r^{d-1}} \partial_r (r^{d-1} \lambda \partial_r T) \\ &+ \text{driving term}, \end{aligned} \quad (7.72)$$

where  $\mu$  is the viscosity,  $\lambda$  is the heat conductivity, and  $\zeta$  is the bulk viscosity.

The viscosity  $\mu$  and heat conduction  $\lambda$  of a fluid of hard-spheres increase with temperature  $T(r, t)$ . The exact expression of  $\mu$  and  $\lambda$  for hard-sphere gas is given by [85, 86],

$$\mu = C_1 \sqrt{T}, \quad (7.73)$$

$$\lambda = C_2 \sqrt{T}, \quad (7.74)$$

where  $C_1$  and  $C_2$  are the coefficients of viscosity and heat conduction respectively. The exact value of  $C_1$  and  $C_2$  are known only for Maxwell molecules. However, as explained in books on kinetic theory [85, 86], the values of  $C_1$  and  $C_2$  are known only approximately that too for dilute gases. So we treat these coefficients as free parameters to see the effects of these parameters on the thermodynamic quantities close to their kinetic theory values. From kinetic theory of gases, the approximate values of  $C_1$  and  $C_2$  for hard sphere particles of diameter  $D$ , which we denote by  $C_1^*$

and  $C_2^*$ , are given by [86]

$$C_1^* = \frac{1}{dD^{d-1}} \sqrt{\frac{mk_B}{\pi^{d-1}}} \frac{\left[\Gamma\left(\frac{d+1}{2}\right)\right]^2}{\Gamma\left(\frac{d}{2}\right)}, \quad (7.75)$$

$$C_2^* = \frac{1}{2D^{d-1}} \sqrt{\frac{k_B^3}{m\pi^{d-1}}} \frac{\left[\Gamma\left(\frac{d+1}{2}\right)\right]^2}{\Gamma\left(\frac{d}{2}\right)}, \quad (7.76)$$

where  $m$  is the mass of a particle, and  $k_B$  is Boltzmann constant.  $\Gamma$  is the Gamma function. The bulk viscosity for mono-atomic gas is zero [87].

We use MacCormack method [82] to numerically solve the Navier-Stokes Eqs. (7.70)–(7.72), for  $\delta = 1$ . This method has accuracy up to second order both in time discretisation  $\Delta t$  and radial discretisation  $\Delta r$ . We call the numerical solution of NSE as direct numerical solution. The initial conditions on thermodynamic quantities at  $t = 0$  are given by: constant density everywhere, zero velocity everywhere, and zero temperature everywhere.

For the energy source at the origin for central driving, instead of taking a delta function energy source, we take it as a Gaussian to avoid numerical difficulties. We replace the driving term in Eq. (7.72) by

$$\text{driving term} = \frac{A_0 \delta t^{\delta-1}}{S_d r^{d-1}} \exp\left[\frac{-r^2 A_0^2 \pi}{4E_0^2}\right]. \quad (7.77)$$

For uniform driving, we model the driving term as

$$\text{driving term} = \frac{A_0 \delta t^{\delta-1}}{V_d R(t)^d} S_\delta(r, R(t)), \quad (7.78)$$

where  $R(t)$  is the radius of shock front, and  $V_d = \pi^{d/2}/\Gamma(1+d/2)$  is the volume of

Table 7.2: The numerical values of different parameters used in solving the Navier-Stokes Eqs. (7.70)–(7.72).

Parameters	Values ( $d = 2$ )	Values ( $d = 3$ )
$\delta$	1.0	1.0
$\Delta r$	0.05	0.08
$\Delta t$	$10^{-4}$	$10^{-4}$
$A_0$	$10^{-4}$	$10^{-4}$
$\gamma$	2	5/3
$\rho_0$	0.382	0.4013
$L$	1000	300
$\zeta$	0	0
$C_1^*$	$\sqrt{\pi}/8$	$2/(3\sqrt{\pi^3})$
$C_2^*$	$\sqrt{\pi}/8$	$1/\sqrt{\pi^3}$

$d$ -dimensional sphere of unit radius.  $S_\delta(x, y)$  is the step function defined as,

$$S_\delta(x, y) = \begin{cases} 1 & x \leq y, \\ 0 & x > y. \end{cases} \quad (7.79)$$

Such energy sources lead the total energy of the system to increase as  $E_0 t^\delta$ .

To avoid edge effects, we choose the system size  $L$  in such a manner that shock does not reach to the boundary upto the maximum time we integrate. We use boundary conditions where at the shock center,  $r = 0$ , the radial derivative of density and temperature are zero, and radial velocity is set to zero, and at the boundary of the region, the initial ambient values are maintained for each of the thermodynamic quantities [83]. The numerical values of the parameters that we use in our DNS are tabulated in the Table 7.2. We now present the parametric study of the DNS of NSE. We first benchmark the DNS using the same criteria that we used for EDMD, i.e. by validating the growth of total energy, radial momentum, and radius of shock front:  $E(t) \sim t$ ,  $M(t) \sim t^{5/4}$  [Eq. (7.68)], and  $R(t) \sim t^{3/4}$  [Eq. (7.69)], in two dimensions for  $\delta = 1$ . We first confirm that in the DNS, the total energy increases as  $E_0 t$  as can be seen from Fig. 7.7(a). The DNS reproduce the power law growth for both shock

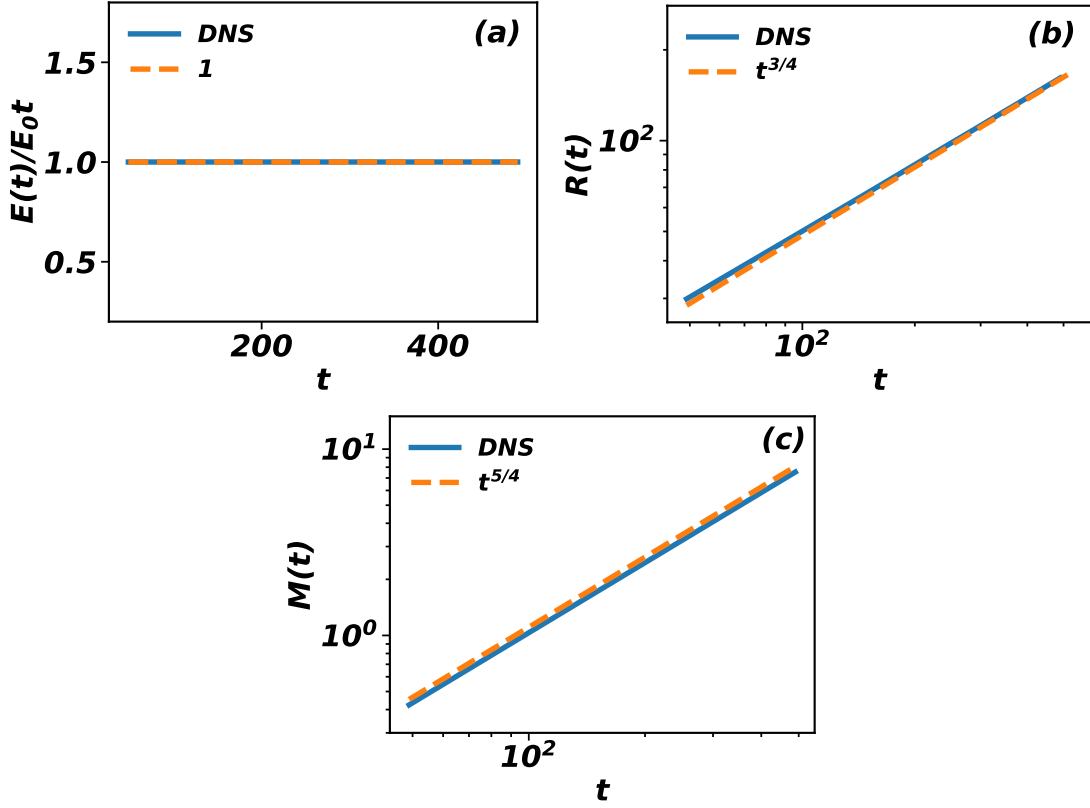


Figure 7.7: Power law growth of (a) total energy  $E(t) = E_0t$ , (b) radius of the shock front  $R(t) \sim t^{3/4}$ , and (c) total radial momentum  $M(t) \sim t^{5/4}$  of the system. Solid lines represent the results from DNS, and dashed lines represent the respective power laws. The DNS data shown here are for ambient gas density  $\rho_0 = 0.382$ ,  $A_0 = 10^{-4}$ ,  $C_1 = C_1^*$ ,  $C_2 = C_2^*$ , and  $\zeta = 0$ . The results are for the central driving in two dimensions with  $\delta = 1$ .

radius as well as radial momentum for large times, as can be seen in Fig. 7.7(b) and (c).

Before comparing the DNS results with results from EDMD simulations, we first examine the role of the various parameters like EOS, dissipation coefficients on the data. We point out that we obtain data collapse of the data for different times when appropriately scaled [see Sec. 7.5]. For the dependence on parameters, we examine the data for one time.

In Fig. 7.8, we show the variation of non-dimensionalised thermodynamic functions, obtained from the DNS of NSE [Eqs. (7.70)–(7.72)], with  $\xi$  for the virial EOS with the series truncated at the  $i = 0, 4, 8, 10$  term. The first thing that we notice is that,



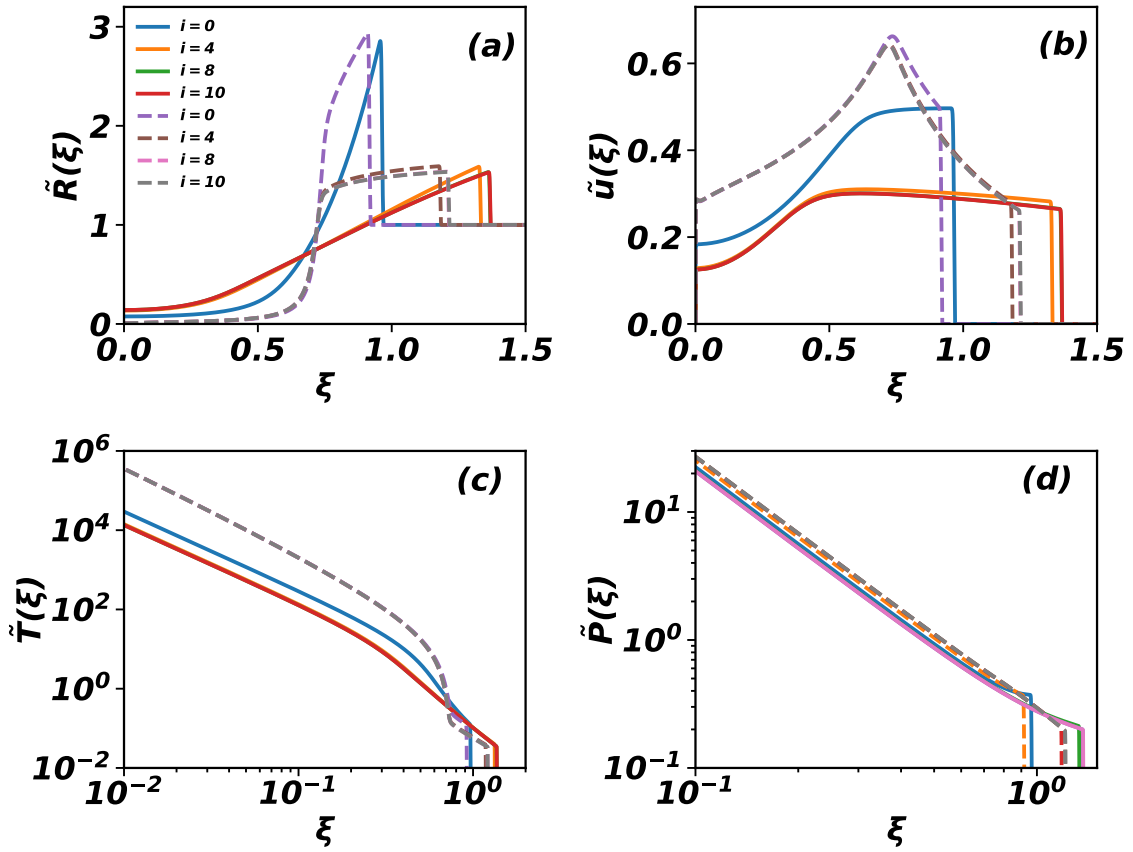


Figure 7.8: The role of the EOS on the DNS data for (a) density  $\tilde{R}(\xi)$ , (b) velocity  $\tilde{u}(\xi)$ , (c) temperature  $\tilde{T}(\xi)$ , and (d) pressure  $\tilde{P}(\xi)$ . The virial EOS [see Eq. (7.55)] is truncated at  $i = 0, 4, 8, 10$ . The DNS data shown here are for initial density  $\rho_0 = 0.382$ ,  $A_0 = 10^{-4}$ ,  $C_1 = C_1^*$ ,  $C_2 = C_2^*$ ,  $\zeta = 0$ , and time  $t = 2t'_0$ , where  $t'_0 = 489.1$ . The dashed lines are for central driving and solid lines are for uniform driving in two dimensions.

for the central driving, the scaled solution of the Navier-Stokes equations covers the entire region of disturbance unlike the Euler equation. The results corresponding to  $i = 0$  represent the DNS for ideal EOS. The data corresponding to  $i = 8, 10$ , lie on top of each other, thus showing negligible truncation error beyond the 10-th term. We will therefore work with virial EOS of 10 terms.

To study the role of viscosity, we study the DNS with four different values of coefficient of viscosity  $C_1^*/2$ ,  $C_1^*$ ,  $2C_1^*$ ,  $4C_1^*$  keeping the heat conduction fixed at  $C_2 = C_2^*$ . We find that the value of  $C_1$  does not affect the results much as can be seen from Fig. 7.9, where the different thermodynamics quantities are shown. We conclude

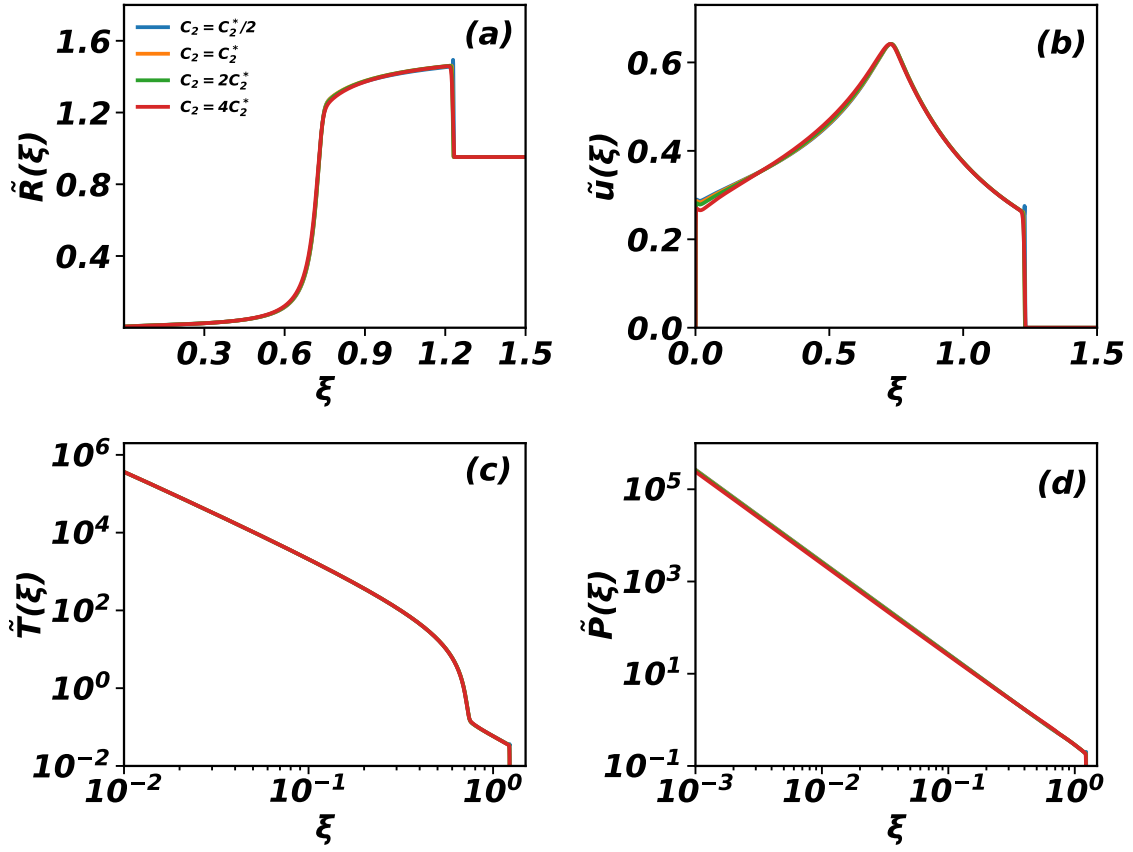


Figure 7.9: The non-dimensionalised (a) density  $\tilde{R}(\xi)$ , (b) velocity  $\tilde{u}(\xi)$ , (c) temperature  $\tilde{T}(\xi)$ , and (d) pressure  $\tilde{P}(\xi)$  obtained from the DNS of Eqs. (7.70)–(7.72) for four different values of coefficient of viscosity  $C_1^*/2$ ,  $C_1^*$ ,  $2C_1^*$ ,  $4C_1^*$ , keeping coefficient of heat conduction fixed at  $C_2 = C_2^*$ . The DNS data shown here are for initial density  $\rho_0 = 0.382$ ,  $A_0 = 10^{-4}$ , virial EOS up to  $10^{th}$  terms,  $\zeta = 0$ , and time  $t = 2t'_0$ , where  $t'_0 = 489.1$ . The results are for the central driving in two dimensions.

that the DNS data are not sensitive to the value of the viscosity of the gas.

To study the role of heat dissipation, we study the DNS with four different values of coefficient of heat conductivity  $C_2^*/2$ ,  $C_2^*$ ,  $2C_2^*$ ,  $4C_2^*$  keeping viscosity  $C_1 = C_1^*$  fixed. Unlike the case of viscosity, we find that the different thermodynamic quantities, except pressure, depend on the value of  $C_2$ , as can be seen from Fig. 7.10.

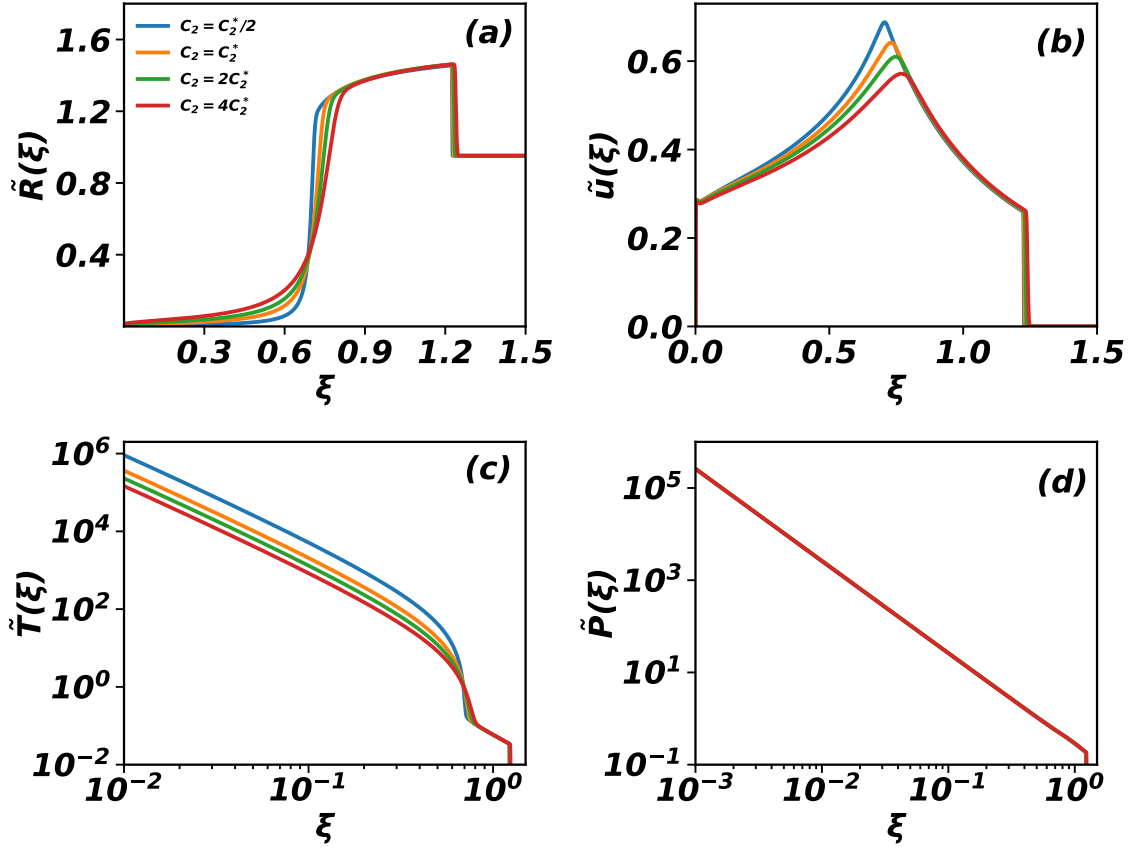


Figure 7.10: The non-dimensionalised (a) density  $\tilde{R}(\xi)$ , (b) velocity  $\tilde{u}(\xi)$ , (c) temperature  $\tilde{T}(\xi)$ , and (d) pressure  $\tilde{P}(\xi)$  obtained from the DNS of Eqs. (7.70)–(7.72) for four different values of coefficient of heat conduction  $C_2^*/2$ ,  $C_2^*$ ,  $2C_2^*$ ,  $4C_2^*$ , keeping coefficient of viscosity fixed at  $C_1 = C_1^*$ . The DNS data shown here are for initial density  $\rho_0 = 0.382$ ,  $A_0 = 10^{-4}$ , virial EOS up to  $10^{th}$  terms,  $\zeta = 0$ , and time  $t = 2t'_0$ , where  $t'_0 = 489.1$ . The results are for the central driving in two dimensions.

## 7.5 Results : comparison between the Euler equation, EDMD, and DNS

We now compare the results from the different schemes that we have used to study continuous shock: simulations of discrete hard spheres using EDMD, solution of Euler equation, and DNS of the Navier-Stokes equations for central as well as uniform driving in two dimensions, and for central driving in three dimensions.

We first show the results in two dimensions. The different non-dimensionalised quantities for four different times are shown in Fig. 7.11 for both uniform and central driving. We first note the results of DNS for different times collapse onto a single curve verifying the scaling Eqs. (7.18)–(7.22). The DNS data are able to capture the EDMD data for  $\tilde{R}(\xi)$ ,  $\tilde{T}(\xi)$ , and  $\tilde{P}(\xi)$ . Interestingly, we find that the power law behavior of thermodynamic quantities from the DNS as well as the EDMD in both the drivings are the same. For the velocity field  $\tilde{u}(\xi)$  for the uniform driving, the results from DNS, while matching with the EDMD results near the shock front, has a quantitative mismatch away from the shock center, as can be seen from Fig. 7.11(b). A possible reason for this mismatch could be that, in the EDMD simulations with uniform driving, there is a non-negligible non-radial velocity at all distances.

For uniform driving, the qualitative behaviour of scaling functions for hard sphere gas, obtained from the numerical solution of Euler equation, are exactly same as the exact solution for ideal gas. In fact, the variation  $\tilde{T} \rightarrow \xi^{-2}$ , in EDMD, indicates that  $T(r, t) \rightarrow r^0 t^{-1/2}$  close to the shock center, which means that the temperature  $T(r, t)$  decreases in time and the slope with respect radial distance  $r$  is zero, while the behaviour  $\tilde{T} \rightarrow \xi^{-4}$  in numerical solution shows that the temperature  $T(r, t)$  varies as  $r^{-2} t^1$  which gives divergent spatial slope of temperature at the shock center. The divergent temperature leads to infinite energy in the system, which is unphysical for a finitely driven system. Since the heat conduction term put a boundary condition:

---

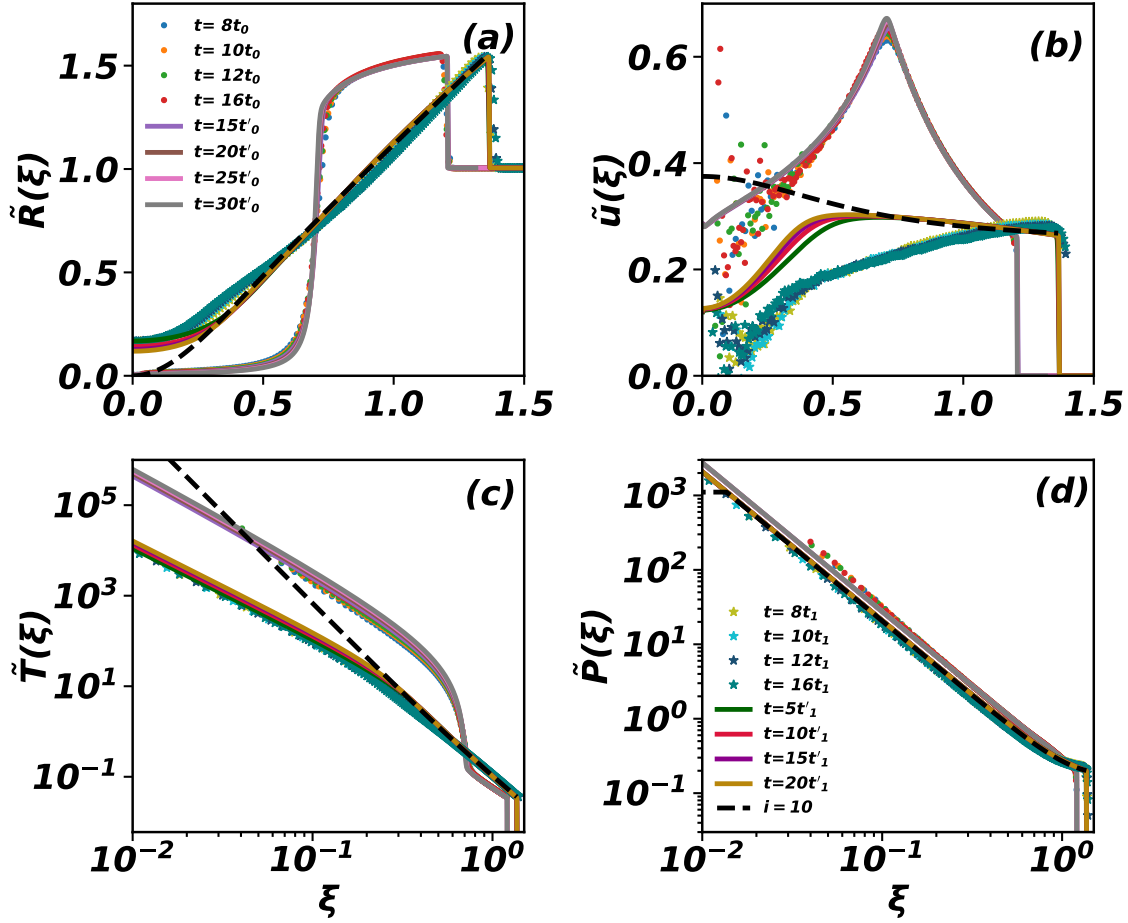


Figure 7.11: The comparison between the profiles of non-dimensionalised (a) density  $\tilde{R}(\xi)$ , (b) velocity  $\tilde{u}(\xi)$ , (c) temperature  $\tilde{T}(\xi)$ , and (d) pressure  $\tilde{P}(\xi)$  obtained from Euler Eqs. (7.57)–(7.59), EDMD, and the DNS of Navier-Stokes Eqs. (7.70)–(7.72) in two dimensions. The EDMD data are for different times  $t = 8t_0, 10t_0, 12t_0, 16t_0$  for central driving (Dots), and at  $t = 8t_1, 10t_1, 12t_1, 16t_1$  for uniform driving (Stars), where  $t_0, t_1 = 1000$ . The solid lines represent the DNS of Navier-Stokes equations at four different times  $t = 15t'_0, 20t'_0, 25t'_0, 30t'_0$  for central driving, and at  $t = 5t'_1, 10t'_1, 15t'_1, 20t'_1$  for uniform driving, where  $t'_0, t'_1 = 489.1$ . The dashed lines represent the results of Euler equation for uniform driving. The data shown here for DNS are for initial density  $\rho_0 = 0.382$ ,  $A_0 = 10^{-4}$ , virial EOS up to  $10^{th}$  terms,  $\zeta = 0$ ,  $C_1 = C_1^*$ ,  $C_2 = C_2^*$ , and the data for EDMD are for ambient gas density  $\rho_0 = 0.382$ ,  $E_0 = 3.3 \times 10^{-4}$ ,  $R_0 = 30.0$ ,  $\Delta t = 1.1$ , and  $8 \times 10^6$  number of hard sphere particles.

$\vec{\nabla}T = 0$ , the solution of full Navier-Stokes equations resolve the discrepancy between EDMD and hydrodynamics.

We now discuss the results in three dimensions for central driving. The different non-dimensionalised quantities for four different times are shown in Fig. 7.12. To match with the EDMD data, we have run the DNS for different values of  $C_1$  and  $C_2$ , and chosen values with the best match. To do so, we started with the initial values of  $C_1$ , and  $C_2$  as  $C_1^*$ , and  $C_2^*$  respectively and then we increased these values systematically till we obtained a best fit (visually) to the data for all the scaling. These results of central driving in three dimensions are very similar to the results in two dimensions, and we conclude that the NSE are able to provide the correct hydrodynamics for the driven shock problem.

## 7.6 Summary and discussion

In summary, we studied the hydrodynamics of shocks in a gas in which energy is continuously input ( $E(t) \sim t^\delta$ ) either at one localised region in space (central driving) or throughout the growing affected region in time (uniform driving). Different schemes were used to study this problem: EDMD simulations, DNS of Navier-Stokes equations, and numerical solution of the Euler equation.

For uniform driving, we showed that the power law exponents of thermodynamic quantities, obtained from the solution of Euler equation, are independent of  $\delta$ . We showed that, for uniform driving, the solution of Euler equation does not match with the EDMD data close to the shock center in terms of different power law exponents, while it matched near the shock front. Inclusion of dissipation terms in terms of the Navier-Stokes equations is able to describe the simulation results near the shock center also.

For central driving, we showed that the self-similar solution of the Euler equation

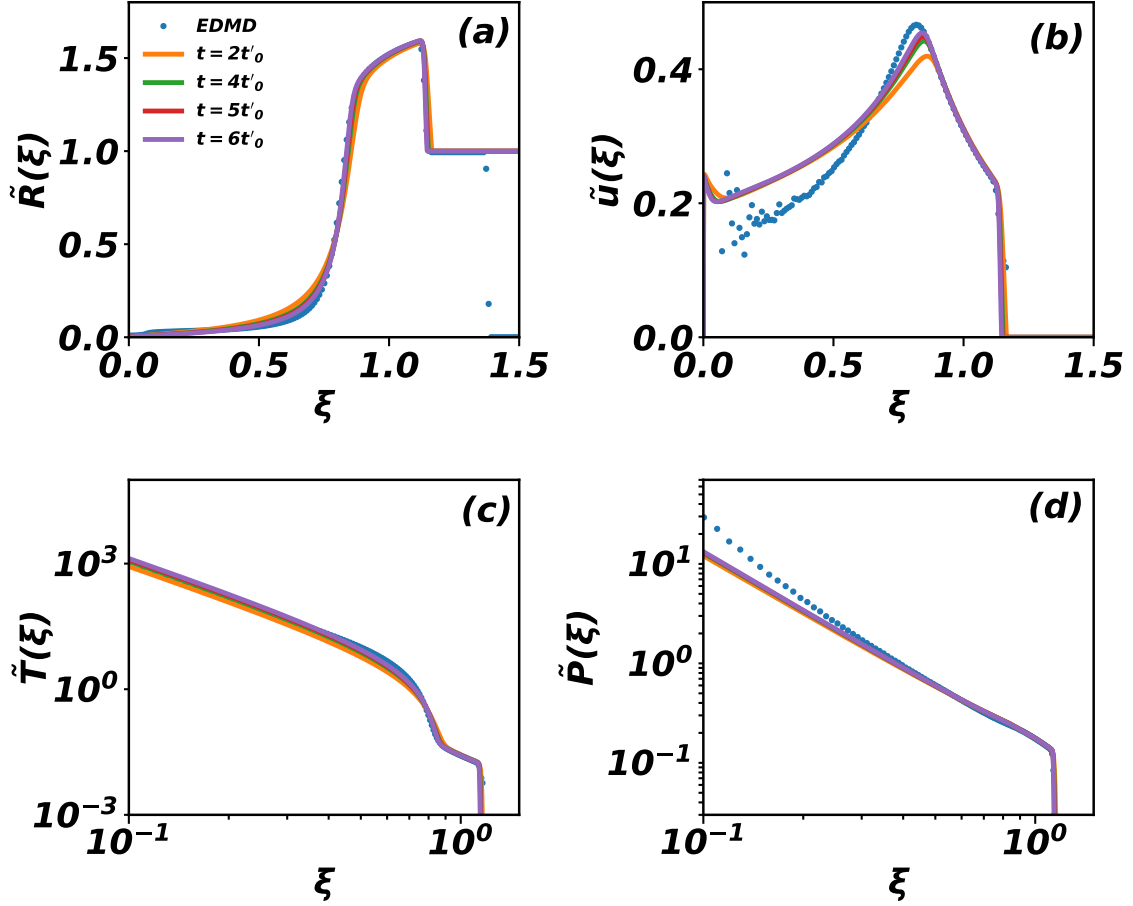


Figure 7.12: The comparison between the profiles of non-dimensionalised (a) density  $\tilde{R}(\xi)$ , (b) velocity  $\tilde{u}(\xi)$ , (c) temperature  $\tilde{T}(\xi)$ , and (d) pressure  $\tilde{P}(\xi)$  obtained from EDMD, and the DNS of Navier-Stokes Eqs. (7.70)–(7.72) in three dimensions. The symbols represent single time EDMD data at time  $t = 3t_0$ , where  $t_0 = 1357.2$ , and the solid lines denote the results of DNS at four different times  $t = 2t'_0, 4t'_0, 5t'_0, 6t'_0$  where  $t'_0 = 69.2$ . The data shown here for DNS are for initial density  $\rho_0 = 0.4013$ ,  $A_0 = 10^{-4}$ , virial EOS up to  $10^{th}$  terms,  $\zeta = 0$ ,  $C_1 = 10C_1^*$ ,  $C_2 = 8.35C_2^*$ , and the data for EDMD are for ambient gas density  $\rho_0 = 0.4013$ ,  $E_0 = 2.5 \times 10^{-6}$ ,  $R_0 = 15.0$ ,  $\Delta t = 0.15$ , and  $4 \times 10^7$  number of hard sphere particles.

is singular and does not extend over the full spatial region of the shock. However, the numerical solutions of Navier-Stokes equations are able to produce self-similar solution that extend all the way to the shock center, thus showing the necessity of dissipation terms to even have a sensible solution. The Navier-Stokes equations are also able to describe the simulation results for the different thermodynamic quantities, provided the heat conduction and viscosity are chosen parametrically.

We conclude that even though the continuous drive takes the system far from equilibrium, Navier-Stokes equations continue to give a good description of the system. For uniform driving, the reason why Euler equation does not provide a good hydrodynamic description remains the same as that for the single impact. Temperature diverges at the shock center, within the Euler equation. Adding a heat conduction term regularises this behaviour with the radial derivative going to zero. This is what is observed in EDMD simulations also. Thus, the solution of the Euler equation does not respect the boundary conditions seen in simulations, leading to an incorrect description. For central driving, the Euler equation fails poorly at describing the system.

Incorporating heat conduction in the continuity equations altered the scaling near the shock center for the case of single impact. This crossover has been quantified in earlier work [18, 80, 95]. Generalising these results to the case of driven shock is an interesting problem for future research. However, obtaining clean data near the shock center is a more challenging problem for driven shocks. Central driving introduces a new length scale, defined by the region of driving, and hence taking the  $r \rightarrow 0$  limit requires simulations of much larger systems. However, it will be easier to study the crossover in the case of uniform driving.



# 8

## Summary and outlook

We have analysed the problem of shock propagation in both homogeneous and inhomogeneous media, initiated by an intense explosion or a continuous energy input either from a localised region of space around the center or throughout the affected region. The shock propagation is described by the exact solution of the Euler equation based on the TvNS theory. Earlier studies have focused on applying TvNS theory and its modifications to model phenomena such as young supernova remnants, gamma-ray bursts, galaxy formation, and experimental verification of shock front radius. However, recent particle-based molecular dynamics simulations, while showing excellent agreement with the power law of shock radius, revealed significant discrepancies between the TvNS theory predictions for intense explosions and the simulation results.

## 8.1 Conclusions and Outlook

In this thesis, we investigate the potential reasons for these discrepancies and propose a resolution.

In Chapter 4, we explore shock propagation in two and three dimensions using the Navier-Stokes equations. We hypothesise that ignoring the heat conduction term could contribute to the observed mismatch, as it imposes a boundary condition that requires a zero temperature gradient at the shock center. Direct numerical solutions of the Navier-Stokes equations for a hard-sphere gas align well with EDMD simulation data in both dimensions, whereas solution of the Euler equation does not. We suggest that the discrepancy arises due to the order of taking limits—solving the continuity equations after rescaling the thermodynamic variables (as done in TvNS theory) is not equivalent to solving the equations first and then rescaling the solution. The Navier-Stokes solution in Cartesian coordinates indeed shows that the heat conduction is zero at the center. We demonstrate that truncating the virial equation of state at the 10th term introduces negligible error, and the numerical solutions for hard-sphere gases remain consistent as long as the equation of state represents the hard sphere gas. Moreover, altering the viscosity coefficient while keeping heat conduction fixed does not affect the solution, whereas changes in heat conduction do affect it. However, these changes do not impact the power-law behaviour near the shock center.

In Chapters 5 and 6, we study shock propagation in a one-dimensional inhomogeneous medium, both for a blast at the center as well as a splash at the interface of a vacuum and inhomogeneous medium. For the blast problem, the thermodynamic quantities can be determined via dimensional analysis, but the exact solution of the Euler equation does not match molecular dynamics simulations except for a critical inhomogeneity parameter,  $\beta$ . In contrast, the Navier-Stokes equations provide ac-

curate results across all values of  $\beta$ . For the critical value of  $\beta$ , the thermodynamic quantities from Euler, Navier-Stokes, and simulations converge, and also we find a new length scale and scaling law for thermodynamic quantities where heat conduction dominates the Euler terms. In the splash problem, thermodynamic quantities cannot be derived purely from dimensional analysis but can be obtained by numerically solving the Euler equation using Rankine-Hugoniot boundary conditions and ensuring single-valued profiles over the rescaled distance. We determine the power-law exponent of energy decay from the numerical solution of the Euler equation, and validate these exponents with molecular dynamics simulations, showing that Euler equation sufficiently describes the splash problem in one dimension.

In Chapter 7, we extend our study to shock propagation both in two as well as in three dimensional hard-sphere gas driven by continuous energy injection from a localised region or throughout the affected region. The external driving takes the system far from equilibrium, and it is unclear whether the Navier-Stokes equations are applicable and solvable. Despite this, the Navier-Stokes equations describe the driven shock well, matching molecular dynamics results when heat conduction and viscosity are chosen parametrically in both dimensions. Also, for the case of energy injection from a localised region, we note that the solution of Euler equation is not achievable for full range of the rescaled distance while the solution of Navier-Stokes equations extends all the way from the shock front to the shock center. Our parametric study shows similar behaviour to the blast problem: changing the viscosity while fixing heat conduction does not affect the solution, but altering heat conduction does. Nonetheless, the power-law behaviour remains unaffected from these changes, and truncating the virial equation of state at the 10th term introduces negligible error.

Shock propagation has also been studied in granular systems, driven either by single impacts or continuous sources. Examples include crater formation from high-energy

impacts on granular heaps, vertical impacts of steel balls into containers of glass beads, and shock propagation from sudden energy release or continuous particle insertion. Hydrodynamic theory has been generalised to describe shock in granular gases, where energy is no longer conserved. Extending these results to inhomogeneous media and driven shock problems, as well as studying splash problems in higher dimensions, would be an interesting direction for future work.

## Bibliography

- [1] L. D. Landau and E. M. Lifshitz. *Fluid Mechanics*. Course of theoretical physics, Vol. 6. Butterworth-Heinemann, Oxford UK, 1987.
  - [2] Grigory Isaakovich Barenblatt. *Scaling, self-similarity, and intermediate asymptotics: dimensional analysis and intermediate asymptotics*. Cambridge University Press, 1996.
  - [3] Gerald Beresford Whitham. *Linear and nonlinear waves*. John Wiley & Sons, 2011.
  - [4] Geoffrey Ingram Taylor. The formation of a blast wave by a very intense explosion i. theoretical discussion. *Proc. Roy. Soc. A*, 201(1065):159–174, 1950.
  - [5] Geoffrey Ingram Taylor. The formation of a blast wave by a very intense explosion.-ii. the atomic explosion of 1945. *Proc. Roy. Soc. A*, 201(1065):175–186, 1950.
  - [6] J. von Neumann. In *Collected Works*, page 219. Pergamon Press, Oxford, 1963.
  - [7] L.I. Sedov. Propagation of strong shock waves. *J. Appl. Math. Mech.*, 10:241, 1946.
  - [8] MJ Edwards, AJ MacKinnon, J Zweiback, K Shigemori, D Ryutov, AM Rubenchik, KA Keilty, E Liang, BA Remington, and Todd Ditmire. In-
-

- vestigation of ultrafast laser-driven radiative blast waves. *Phys. Rev. Lett.*, 87(8):085004, 2001.
- [9] AD Edens, T Ditmire, JF Hansen, MJ Edwards, RG Adams, P Rambo, L Rugles, IC Smith, and JL Porter. Study of high mach number laser driven blast waves. *Phys. Plasma*, 11(11):4968–4972, 2004.
- [10] Alastair S Moore, Daniel R Symes, and Roland A Smith. Tailored blast wave formation: Developing experiments pertinent to laboratory astrophysics. *Phys. Plasma*, 12(5):052707, 2005.
- [11] L.I. Sedov. *Similarity and Dimensional Methods in Mechanics*. CRC Press, Florida, 10 edition, 1993.
- [12] Subhadip Chakraborti, Abhishek Dhar, and Paul Krapivsky. A splash in a one-dimensional cold gas. *SciPost Physics*, 13(3):074, 2022.
- [13] VI Dokuchaev. Self-similar spherical shock solution with sustained energy injection. *Astronomy & Astrophysics*, 395(3):1023–1029, 2002.
- [14] Zahera Jabeen, R Rajesh, and Purusattam Ray. Universal scaling dynamics in a perturbed granular gas. *EPL (Europhysics Letters)*, 89(3):34001, 2010.
- [15] T Antal, PL Krapivsky, and S Redner. Exciting hard spheres. *Phys. Rev. E*, 78(3):030301, 2008.
- [16] Jilmy P Joy, Sudhir N Pathak, and R Rajesh. Shock propagation following an intense explosion: comparison between hydrodynamics and simulations. *J. Stat. Phys.*, 182(2):1–22, 2021.
- [17] Jilmy P Joy and R Rajesh. Shock propagation in the hard sphere gas in two dimensions: comparison between simulations and hydrodynamics. *J. Stat. Phys.*, 184(1):1–16, 2021.
-

- [18] Subhadip Chakraborti, Santhosh Ganapa, PL Krapivsky, and Abhishek Dhar. Blast in a one-dimensional cold gas: From newtonian dynamics to hydrodynamics. *Phys. Rev. Lett.*, 126(24):244503, 2021.
  - [19] SF Gull and MS Longair. A numerical model of the structure and evolution of young supernova remnants. *Monthly Notices of the Royal Astronomical Society*, 161(1):47–69, 1973.
  - [20] LL Cowie. The early evolution of supernova remnants in a homogeneous medium-the effects of electron thermal conduction. *Astro. J.*, 215:226–231, 1977.
  - [21] E Bertschinger. Cosmological self-similar shock waves and galaxy formation. *Astro. J.*, 268:17–29, 1983.
  - [22] E. Bertschinger. Cosmological detonation waves. *Astro. J.*, 295:1–13, 1985.
  - [23] Denis F Cioffi, Christopher F McKee, and Edmund Bertschinger. Dynamics of radiative supernova remnants. *Astro. J.*, 334:252–265, 1988.
  - [24] Jeremiah P Ostriker and Christopher F McKee. Astrophysical blastwaves. *Rev. Mod. Phys.*, 60(1):1, 1988.
  - [25] Re'em Sari. Hydrodynamics of gamma-ray burst afterglow. *The Astrophysical Journal*, 489(1):L37–L40, 1997.
  - [26] VS Berezhinsky and VI Dokuchaev. Hidden source of high-energy neutrinos in collapsing galactic nucleus. *Astroparticle Physics*, 15(1):87–96, 2001.
  - [27] Matthieu Barbier, Dario Villamaina, and Emmanuel Trizac. Blast dynamics in a dissipative gas. *Phys. Rev. Lett.*, 115(21):214301, 2015.
  - [28] Matthieu Barbier, Dario Villamaina, and Emmanuel Trizac. Microscopic origin of self-similarity in granular blast waves. *Phys. Fluids*, 28(8):083302, 2016.
-

- [29] VS Avedisova. Formation of nebulae by wolf-rayet stars. *Soviet Astronomy*, 15:708, 1972.
  - [30] SAEG Falle. A numerical calculation of the effect of stellar winds on the interstellar medium. *Astronomy and Astrophysics*, 43:323–336, 1975.
  - [31] John Castor, Richard McCray, and Robert Weaver. Interstellar bubbles. *Astrophysical Journal*, vol. 200, Sept. 1, 1975, pt. 2, p. L107-L110., 200:L107–L110, 1975.
  - [32] Robert Weaver, Richard McCray, John Castor, Paul Shapiro, and Robert Moore. Interstellar bubbles. ii-structure and evolution. *Astrophysical Journal*, Part 1, vol. 218, Dec. 1, 1977, p. 377-395., 218:377–395, 1977.
  - [33] AF Ghoniem, MM Kamel, SA Berger, and AK Oppenheim. Effects of internal heat transfer on the structure of self-similar blast waves. *Journal of Fluid Mechanics*, 117:473–491, 1982.
  - [34] AM Abdel-Raouf and W Gretler. Quasi-similar solutions for blast waves with internal heat transfer effects. *Fluid dynamics research*, 8(5-6):273, 1991.
  - [35] H Steiner and W Gretler. The propagation of spherical and cylindrical shock waves in real gases. *Phys. Fluids*, 6(6):2154–2164, 1994.
  - [36] Viktor Pavlovich Korobeinikov. On propagation of strong spherical blast wave in gas with heat conduction. In *Doklady Akademii Nauk*, volume 113, pages 1006–1009. Russian Academy of Sciences, 1957.
  - [37] John VonNeumann and Robert D Richtmyer. A method for the numerical calculation of hydrodynamic shocks. *Journal of applied physics*, 21(3):232–237, 1950.
  - [38] Myron N Plooster. Shock waves from line sources. numerical solutions and experimental measurements. *The Phys. Fluids*, 13(11):2665–2675, 1970.
-



- [39] Harold L Brode. Numerical solutions of spherical blast waves. *Journal of Applied physics*, 26(6):766–775, 1955.
  - [40] Richard Latter. Similarity solution for a spherical shock wave. *Journal of Applied Physics*, 26(8):954–960, 1955.
  - [41] JRAJ NiCastro. Similarity analysis of the radiative gas dynamic equations with spherical symmetry. *The Physics of Fluids*, 13(8):2000–2006, 1970.
  - [42] Kuo Chang Wang. The ‘piston problem’ with thermal radiation. *Journal of Fluid Mechanics*, 20(3):447–455, 1964.
  - [43] G Guderley. Powerful spherical and cylindrical compression shocks in the neighbourhood of the centre and of the cylinder axis. *Luftfahrtforschung*, 19:302–312, 1942.
  - [44] Roger B Lazarus. Self-similar solutions for converging shocks and collapsing cavities. *SIAM Journal on Numerical Analysis*, 18(2):316–371, 1981.
  - [45] Thomas Hirschler and Helfried Steiner. A self-similar solution for the implosion problem in a dusty gas. *Fluid dynamics research*, 32(3):61–67, 2003.
  - [46] NF Ponchaut, HG Hornung, DI Pullin, and CA Mouton. On imploding cylindrical and spherical shock waves in a perfect gas. *Journal of Fluid Mechanics*, 560:103–122, 2006.
  - [47] Heinrich M Jaeger, Sidney R Nagel, and Robert P Behringer. Granular solids, liquids, and gases. *Reviews of modern physics*, 68(4):1259, 1996.
  - [48] Y Grasselli and HJ Herrmann. Crater formation on a three dimensional granular heap. *Granular Matter*, 3(4):201–204, 2001.
  - [49] Amanda M Walsh, Kristi E Holloway, Piotr Habdas, and John R de Bruyn. Morphology and scaling of impact craters in granular media. *Phys. Rev. Lett.*, 91(10):104301, 2003.
-

- [50] Philip T Metzger, Robert C Latta III, Jason M Schuler, and Christopher D Immer. Craters formed in granular beds by impinging jets of gas. In *AIP Conference Proceedings*, volume 1145, pages 767–770. American Institute of Physics, 2009.
  - [51] Jean-François Boudet, J Cassagne, and Hamid Kellay. Blast shocks in quasi-two-dimensional supersonic granular flows. *Phys. Rev. Lett.*, 103(22):224501, 2009.
  - [52] Sudhir N Pathak, Zahera Jabeen, Purusattam Ray, and R Rajesh. Shock propagation in granular flow subjected to an external impact. *Phys. Rev. E*, 85(6):061301, 2012.
  - [53] Kai Huang, Guoqing Miao, Peng Zhang, Yi Yun, and Rongjue Wei. Shock wave propagation in vibrofluidized granular materials. *Physical Review E—Statistical, Nonlinear, and Soft Matter Physics*, 73(4):041302, 2006.
  - [54] J Bougie, Sung Joon Moon, JB Swift, and Harry L Swinney. Shocks in vertically oscillated granular layers. *Physical Review E*, 66(5):051301, 2002.
  - [55] A Goldshtein, M Shapiro, and C Gutfinger. Mechanics of collisional motion of granular materials. part 3. self-similar shock wave propagation. *Journal of Fluid Mechanics*, 316:29–51, 1996.
  - [56] Patrick Heil, Erin C Rericha, Daniel I Goldman, and Harry L Swinney. Mach cone in a shallow granular fluid. *Physical Review E—Statistical, Nonlinear, and Soft Matter Physics*, 70(6):060301, 2004.
  - [57] Alain Molinari and Chiara Daraio. Stationary shocks in periodic highly nonlinear granular chains. *Physical Review E—Statistical, Nonlinear, and Soft Matter Physics*, 80(5):056602, 2009.
-

- [58] Vitalii Fedorovich Nesterenko. Propagation of nonlinear compression pulses in granular media. *J. Appl. Mech. Tech. Phys.(Engl. Transl.);(United States)*, 24(5), 1984.
  - [59] Mason A Porter, Chiara Daraio, Eric B Herbold, Ivan Szelengowicz, and PG Kevrekidis. Highly nonlinear solitary waves in periodic dimer granular chains. *Physical Review E*, 77(1):015601, 2008.
  - [60] Mason A Porter, Chiara Daraio, Ivan Szelengowicz, Eric B Herbold, and PG Kevrekidis. Highly nonlinear solitary waves in heterogeneous periodic granular media. *Physica D: Nonlinear Phenomena*, 238(6):666–676, 2009.
  - [61] Viktor Pavlovich Korobeinikov. *Problems of point blast theory*. Springer Science & Business Media, 1991.
  - [62] LV Shurshalov. Calculation of powerful underwater explosions. *Fluid Dynamics*, 6(5):750–754, 1971.
  - [63] Viktor Pavovich Korobeinikov, NS Melnikova, and Ye V Rysanov. *The theory of point explosion*. US Department of Commerce, Office of Technical Services, 1962.
  - [64] GS Bisnovatyi-Kogan and SA Silich. Shock-wave propagation in the nonuniform interstellar medium. *Reviews of Modern Physics*, 67(3):661, 1995.
  - [65] Robbie C Dohm-Palmer and Thomas W Jones. Young supernova remnants in nonuniform media. *The Astrophysical Journal*, 471(1):279, 1996.
  - [66] SES Ferreira and OC De Jager. Supernova remnant evolution in uniform and non-uniform media. *Astronomy & Astrophysics*, 478(1):17–29, 2008.
  - [67] Dallas D Laumbach and Ronald F Probstein. A point explosion in a cold exponential atmosphere. *Journal of Fluid Mechanics*, 35(1):53–75, 1969.
-

- [68] Ya B Zel'Dovich and Yu P Raizer. *Physics of shock waves and high-temperature hydrodynamic phenomena*. Courier Corporation, 2002.
- [69] Richard Courant and Kurt Otto Friedrichs. *Supersonic flow and shock waves*, volume 21. Springer Science & Business Media, 1999.
- [70] Roger A Chevalier. Self-similar solutions for the interaction of stellar ejecta with an external medium. *Astrophysical Journal, Part 1, vol. 258, July 15, 1982, p. 790-797. Research supported by the University of Virginia*, 258:790–797, 1982.
- [71] J Kelly Truelove and Christopher F McKee. Evolution of nonradiative supernova remnants. *The Astrophysical Journal Supplement Series*, 120(2):299, 1999.
- [72] Christopher D Matzner and Christopher F McKee. The expulsion of stellar envelopes in core-collapse supernovae. *The Astrophysical Journal*, 510(1):379, 1999.
- [73] Kirill Petrovich Stanyukovich. *Unsteady motion of continuous media*. Elsevier, 2016.
- [74] Jilmy P Joy, Sudhir N Pathak, Dibyendu Das, and R Rajesh. Shock propagation in locally driven granular systems. *Phys. Rev. E*, 96(3):032908, 2017.
- [75] Xiang Cheng, Lei Xu, Aaron Patterson, Heinrich M Jaeger, and Sidney R Nagel. Towards the zero-surface-tension limit in granular fingering instability. *Nature Physics*, 4(3):234–237, 2008.
- [76] Bjornar Sandnes, HA Knudsen, KJ Måløy, and EG Flekkøy. Labyrinth patterns in confined granular-fluid systems. *Phys. Rev. Lett.*, 99(3):038001, 2007.
- [77] SF Pinto, MS Couto, APF Atman, SG Alves, Américo Tristão Bernardes, HFV de Resende, and EC Souza. Granular fingers on jammed systems: New

- fluidlike patterns arising in grain-grain invasion experiments. *Phys. Rev. Lett.*, 99(6):068001, 2007.
- [78] Øistein Johnsen, Renaud Toussaint, Knut Jørgen Måløy, and Eirik Grude Flekkøy. Pattern formation during air injection into granular materials confined in a circular hele-shaw cell. *Phys. Rev. E*, 74(1):011301, 2006.
- [79] Haiying Huang, Fengshou Zhang, Patrick Callahan, and Joseph Ayoub. Granular fingering in fluid injection into dense granular media in a hele-shaw cell. *Phys. Rev. Lett.*, 108(25):258001, 2012.
- [80] Santhosh Ganapa, Subhadip Chakraborti, PL Krapivsky, and Abhishek Dhar. Blast in the one-dimensional cold gas: Comparison of microscopic simulations with hydrodynamic predictions. *Phys. Fluids*, 33(8):087113, 2021.
- [81] Dennis C Rapaport and Dennis C Rapaport Rapaport. *The art of molecular dynamics simulation*. Cambridge university press, 2004.
- [82] Robert William MacCormack. A numerical method for solving the equations of compressible viscous flow. *AIAA journal*, 20(9):1275–1281, 1982.
- [83] Amit Kumar and R Rajesh. Blast waves in two and three dimensions: Euler versus navier–stokes equations. *Journal of Statistical Physics*, 188(2):1–14, 2022.
- [84] Zahir UA Warsi. *Fluid dynamics: theoretical and computational approaches*. CRC press, 2005.
- [85] Kerson Huang. Statistical mechanics, john wily & sons. *New York*, page 10, 1963.
- [86] Frederick Reif. *Fundamentals of statistical and thermal physics*. Waveland Press, 2009.
-

- [87] Radouan Boukharfane, Pedro José Martínez Ferrer, Arnaud Mura, and Vincent Giovangigli. On the role of bulk viscosity in compressible reactive shear layer developments. *European Journal of Mechanics-B/Fluids*, 77:32–47, 2019.
- [88] Otto J Eder and Thomas Lackner. Pressure and bulk viscosity in a hard sphere gas. *The Journal of Chemical Physics*, 75(2):853–858, 1981.
- [89] Barry M McCoy. *Advanced statistical mechanics*, volume 146. Oxford University Press, 2010.
- [90] Douglas Henderson. A simple equation of state for hard discs. *Molecular Physics*, 30(3):971–972, 1975.
- [91] A Santos, M López de Haro, and S Bravo Yuste. An accurate and simple equation of state for hard disks. *J. Chem. Phys.*, 103(11):4622–4625, 1995.
- [92] Alain Barrat and Emmanuel Trizac. Molecular dynamics simulations of vibrated granular gases. *Phys. Rev. E*, 66(5):051303, 2002.
- [93] A Mulero, I Cachadina, and JR Solana. The equation of state of the hard-disc fluid revisited. *Molecular Physics*, 107(14):1457–1465, 2009.
- [94] Amit Kumar and R Rajesh. Shock propagation following an intense explosion in an inhomogeneous gas: core scaling and hydrodynamics. *Journal of Statistical Physics*, 192(2):17, 2025.
- [95] Sahil Kumar Singh, Subhadip Chakraborti, Abhishek Dhar, and PL Krapivsky. Blast waves in the zero temperature hard sphere gas: double scaling structure. *Journal of Statistical Physics*, 190(7):118, 2023.
- [96] Amit Kumar and R Rajesh. Shock propagation in a driven hard sphere gas: molecular dynamics simulations and hydrodynamics. *arXiv preprint arXiv:2409.12086*, 2025.

- [97] Yunson Du, Hao Li, and Leo P Kadanoff. Breakdown of hydrodynamics in a one-dimensional system of inelastic particles. *Physical review letters*, 74(8):1268, 1995.
- [98] Pablo I Hurtado. Breakdown of hydrodynamics in a simple one-dimensional fluid. *Physical review letters*, 96(1):010601, 2006.
- [99] Christian B Mendl and Herbert Spohn. Shocks, rarefaction waves, and current fluctuations for anharmonic chains. *Journal of Statistical Physics*, 166:841–875, 2017.
- [100] Pablo I Hurtado and Pedro L Garrido. A violation of universality in anomalous fourier’s law. *Scientific reports*, 6(1):38823, 2016.
- [101] Amit Kumar and R. Rajesh. Splash in an inhomogeneous gas in one dimension: Exact analysis and molecular dynamics simulations. *arXiv preprint arXiv:2504.03549*, 2025.
- [102] Miyu Masuyama, Toshikazu Shigeyama, and Yoichiro Tsuboki. Spherical explosion with a central energy source. *Publications of the Astronomical Society of Japan*, 68(2):22, 2016.
- [103] Masaharu Isobe. Hard sphere simulation in statistical physics—methodologies and applications. *Molecular Simulation*, 42(16):1317–1329, 2016.